Effects of surfzone wave transformation on swash dynamics

A thesis submitted in fulfilment
of the requirements for the degree of

Doctor of Philosophy
in
Earth Sciences
at
The University of Waikato

by

Rafael Marcondes Carvalho Guedes

THE UNIVERSITY OF
WAIKATO
Te Whare Wānanga o Waikato

2012

Abstract

Swash oscillations on two natural beaches were measured to show that the shape and magnitude of energy spectra can be largely dependent on processes occurring inside the surfzone. The observations took place on a steep, intermediate beach on the east coast (Tairua Beach), and a low-sloping, dissipative beach located on the west coast of New Zealand (Ngarunui Beach, Raglan), and aimed at improving the understanding of the effects of wave breaking, beach slope, and nonlinear wave interactions on the swash oscillations. These problems were addressed by analysing datasets obtained from field experiments undertaken at these two sites.

A field experiment at Tairua Beach showed that swash oscillations were critically dependent on the stage of the tide which controlled the degree of wave energy dissipation over the sandbar crest. Under mild, near-constant offshore wave conditions, the presence of a sandbar and the tidally-controlled water depth over its crest determined whether most of the incoming waves broke before reaching the shoreline. This forced a change in the pattern of wave energy dissipation across the surfzone between low and high tide, which was reflected by changes to swash elevation (runup) on time-scales of a few hours. Significant runup height *Rs*, defined as 4 times the standard deviation of the waterline time series, varied by a factor of 2 between low tide, when most of the waves were breaking over the sandbar and high tide, when the waves were barely breaking. The increase in wave energy dissipation during low tide was associated with changes in swash maxima distribution, decrease in mean swash period and increasing energy at infragravity frequencies (0.004–0.05 Hz). Bispectral analysis suggested this infragravity modulation might be connected with the presence of secondary waves at the shoreline.

Swash oscillations at Tairua were not homogeneous along the beach. Alongshore variability in *Rs* of up to 78% was observed and was mainly driven by changes in the sea-swell (0.05–0.4 Hz) band of the swash. This variability was predominantly controlled by alongshore changes in beach face slope, although alongshore patterning in wave breaking over the sandbar caused alongshore changes in wave dissipation and also resulted in alongshore swash variation in the sea-swell bandwidth. At infragravity frequencies, alongshore swash variability was not well associated either with changes in beach slope or wave breaking and was possibly linked to the presence of low-mode edge waves, observed from frequency-wavenumber spectra of the swash time series.

A final experiment was conducted to understand the surfzone control on incident and infragravity runup on a gently-sloping beach. The observations showed that runup saturation at infragravity frequencies can occur under mild offshore energy conditions if the beach slope is sufficiently gentle. Infragravity saturation was observed for higher-frequency (> 0.025–0.035 Hz) infragravity waves, where typically less than 5% of the (linear) energy flux was reflected from the beach and where, similar to the sea-swell band, the swash energy was independent of offshore wave energy. The infragravity frequency range of saturation was determined by the tide, with saturation extending to lower frequencies at low tide when the local beach face slope over the concave-shaped profile was gentler. Runup was strongly dominated by infragravity frequencies, which accounted on average for 96% of the runup variance, and its energy levels were entirely consistent with strong infragravity wave dissipation observed in the surfzone, particularly when including the nonlinear contributions to the wave energy fluxes. Our observations show evidence of nonlinear interactions involving infragravity and high-frequency, harmonic waves, and suggest that these harmonics could play a role in the wave energy balance near the shoreline on low-sloping, dissipative beaches.

Acknowledgements

I would like to truly thank Drs Karin Bryan and Giovanni Coco for giving me the opportunity to do my PhD under their supervision during the past three years. It has been an amazing experience to be guided by such a motivated, dedicated, smart, helpful and inspiring team of supervisors. I have learned so much from both of you and I already miss our regular meetings down at NIWA or at Karin's office! I am a very lucky person for having had the chance to work with you both and I hope we can keep working together for a long time.

I am grateful for the New Zealand Foundation for Research, Science and Technology and NIWA for funding this work and providing the scholarship that allowed me to undertake my research.

I acknowledge the immense support I had during the field experiment undertaken in Raglan, which would not have been possible without Giovanni Coco, Cliff Hart, Rod Budd, Iain MacDonald, George Payne, Dirk Immenga, Ron Ovenden, Nicole Hancock, and Scott Edhouse. Thanks to the Raglan Surf Life Saving Club, in special to Anne Snowdens and Debbie Phillips-Morgan, for kindly allowing us to use their facility during the experiment. Also thanks to Angeline Greensill and Noel Barber for generously helping with the logistics of the field experiment.

Thanks to all the staff in the Department of Earth and Ocean Sciences for being so helpful throughout these 3 years, in special to Sydney Wright.

I am grateful for having had the chance to collaborate with and learn from Dr Rob Holman.

Thanks to Drs Ian Turner and Nadia Sénéchal for providing a careful review, valuable suggestions and insightful discussion on this thesis.

I would like to thank Wing Yan Man, for extensively helping with the runup digitisation, Nathaniel Plant, for allowing me to use his code to estimate neashore bathymetry from video, and Sarah Kruse and Joseph Vangaalen, for providing the Lidar survey undertaken at Tairua Beach.

The wavelet analysis was performed using code developed by Christopher Torrence and Gilbert P. Compo. Thanks for making those freely available at http://paos.colorado.edu/research/wavelets/.

Finally, I thank my wife, Lisa, for being with me in New Zealand during these 3 years. Your support and your encouragement have been essential throughout this whole journey. Thanks also to my family back home for always encouraging and supporting me in all my decisions.

Table of Contents

List of Figures

List of Tables

Table of symbols

A_f: Complex Fourier coefficient

ADCP: Acoustic Doppler Current Profiler

ADV: Acoustic Doppler Velocimeter

$b(f_1, f_2)$: Bicoherence

$B(f_1, f_2)$: Bispectrum

C_f: Co-spectrum

DoF: Degrees of freedom

Dp: Peak wave direction

$E(k, f)$: Wavenumber-frequency spectra

$E[\ ]$: Expected value

Ed, E_d: Energy density

E_{rms}: Root mean square error

F: Net wave energy flux

f: Wave frequency

F_L: Linear component of the net wave energy flux

F_L^-: Shoreward-propagating component of the linear wave energy flux

F_L^+: Seaward-propagating component of the linear wave energy flux

F_{NL}: Nonlinear component of the net wave energy flux

f_p: Peak wave frequency

g: Acceleration due to gravity

GF: Groupiness factor

h: water depth

H: Wave height

H_0: Deep water significant wave height

Hs: Significant wave height

h_x: Characteristic bed slope

Ig: Infragravity

IMLE: Iterative Maximum Likelihood Estimator

***Inc*:** Incident

k: Wavenumber

L_0: Deep water wavelength

M: Sea-swell mass flux

Max(P_{br}): Maximum probability of breaking at any cross-shore location

N_{br}: Number of breaking waves

P_{br}: Probability of breaking

P_t: Proportion of the total variance explained by its temporal component

P_y: Proportion of the total variance explained by its alongshore component

r: Pearson product-moment correlation coefficient

R: Runup

r^2: Squared correlation coefficient

R^2: Squared reflection coefficient

r^2_{adj}: Adjusted squared correlation coefficient

R_{mean}: Mean runup elevation

Rs: Significant runup height

Rv: Vertical runup elevation

***SS*:** Sea-swell

S_{xx}: Sea-swell radiation stress

T: Wave period

Tp: Peak wave period

u: Cross-shore component of velocity

V: Velocity

W: Wave energy transfer

X, x: Cross-shore coordinates

X_{br}: Cross-shore location of maximum probability of breaking

Y, y: Alongshore coordinates

Z, z: Vertical coordinates

β: Beach slope

$\beta_{2\sigma}$: Beach face slope between mean ± 2σ of the shoreline positions

B_H: Battjes' normalized bed slope parameter

β_{mean}: Beach face slope between the mean shoreline position ± 10cm in elevation

γ: Skewness of swash maxima distribution

ΔX_S: Cross-shore distance from the shoreline

ζ: Swash maxima

η^-: Shoreward-propagating free surface elevation

η: Tide level and free surface elevation

η^+: Seaward-propagating free surface elevation

η_0: Offshore free surface elevation

$\theta(f_1, f_2)$: Biphase

ξ_0: Iribarren number

π: Pi

σ: Standard deviation

σ^2: Variance

ω: Radian wave frequency

$\int P_{br}\mathrm{d}x$: Integral probability of breaking between locations of minimum and maximum P_{br}

Chapter 1

General introduction

1.1 Thesis topic

Swash motions, loosely defined as runup, are short-term (seconds to a few minutes) oscillations of the interface between the dry beach and the ocean. These oscillations are driven by the incoming wave energy that reaches the shoreline and can induce large rates of sediment transport between the subaerial and subaqueous parts of the beach (*Masselink and Hughes*, 1998), changes in beach morphology (*Holland and Puleo*, 2001), dune erosion (*Palmsten and Holman*, 2011) and coastal flooding (*Ruggiero et al.*, 2001). Understanding how runup changes in both time and space and what causes these changes is a key to defining effective coastal structures (*Kobayashi*, 1999) and practicable shoreline setback criteria (*Ruggiero et al.*, 2001) in order to mitigate risks associated with inundation and erosion on the coast.

The magnitude and spectral features of runup have traditionally been described in terms of offshore wave conditions (e.g., *Guza and Thornton*, 1982; *Ruessink et al.*, 1998; *Sénéchal et al.*, 2011), local beach face slope (e.g., *Ruggiero et al.*, 2004), or combinations of these two parameters, expressed in the form of simple parameterizations (e.g., *Mase*, 1988; 1989; *Holman and Sallenger*, 1985; *Holman*, 1986; *Raubenheimer and Guza*, 1996; *Stockdon et al.*, 2006). Though these approaches provide convenient means of assessing some characteristics of the swash oscillations on different beaches, inter-site comparisons (e.g. *Raubenheimer and Guza*, 1996; *Stockdon et al.*, 2006) have suggested that such simple formulas, normally developed for specific locations, might not be appropriated for different sites, since considerable variability in the relationships were typically observed. Such variability potentially arises because of other processes not accounted for by these parameterizations, affecting the swash in different ways on the different sites. For instance, it could be mentioned local effects including swash infiltration and exfiltration across the beach face (*Turner and Masselink*, 1998), and non-local effects, such as those of continental shelf width on the wave climate (*Herbers et al.*, 1995). However, little attention has been given to how processes taking place in between intermediate–deep water regions and the shoreline, such as bar-induced wave breaking dissipation and nonlinear wave energy transfers between frequencies, can affect swash oscillations.

The distribution of energy with frequency can change dramatically within the surfzone, either because the dissipation is frequency-dependant, or because energy is transferred between frequencies, causing energy at one frequency to grow at the expense of another. Just seaward of the breakpoint, group modulations in the incident waves can transfer energy to lower (infragravity) frequencies (e.g., *Symonds et al.*, 1982). At the same time, the saw-tooth shape that occurs when waves shoal in shallow water can induce transfers of energy to higher (harmonic) frequencies (e.g., *Elgar et al.*, 1985). As breaking occurs, the main incident energy peak becomes smaller relative to in infragravity and harmonic frequency regions (e.g. *Sénéchal et al.*, 2002), until eventually they two are acted on by dissipation processes (either bottom friction or breaking).

The dissipation of incident waves inside the surfzone due to breaking is a strong function of depth and seabed slope (*Peregrine*, 1983). Wave breaking takes place when the wave crest overturns and collapses on or in front of the wave face, generating spray and white water and promoting turbulent dissipation. Wave breaking is the dominant dissipative mechanism, controls wave transformation in shallow water (*Thornton and Guza*, 1983) and can be modulated by the tide (e.g., *Howd et al.*, 1991) as most beaches typically have exponential profiles. The presence of one or more sandbars in the surfzone also determines if and how the wave breaks (e.g. *Lippmann and Holman*, 1989), since they cause abrupt changes to seabed slope and water depth. As a result, sandbars can strongly control patterns in surfzone wave dissipation, and potentially the total wave energy reaching the swash zone. However, the emphasis on offshore characteristics and beach face slope has meant the effects of the tide and nearshore sandbar morphology in controlling the characteristics of runup have not been fully explored.

Alongshore variations in swash have largely been attributed to alongshore beach face slope variations (*Holman and Sallenger*, 1985; *Ruggiero et al.*, 2004; *Stockdon et al.*, 2006) or, at a smaller spatial scale, to the influence of cusps (*Ciriano et al.*, 2005; *Stockdon et al.*, 2006; *Holland and Holman*, 1996; *Bryan and Coco*, 2010). Potential tidal effects associated with alongshore changes to the sandbar morphology have been neglected. Tidal changes can cause large differences to alongshore breaking patterns, particularly in cases when the alongshore bar is irregular (e.g. *van Enckevort and Ruessink*, 2003; *Ruessink et al.*, 2007). These breaking patterns not only cause irregular dissipation of incident energy which may cause alongshore patterning of incident swash, but also patterning in the incident group structure. As a consequence, alongshore variations in the swash at infragravity ranges might be expected, quite separate from any effect beach cusps might have. Interest in alongshore variability in swash characteristics is both scientific, since it might be associated with infragravity wave signatures at the shoreline (e.g., *Ciriano et al.*, 2005) and practical, since alongshore variability in runup could be used in coastal zone management of localised hazards (e.g., hot-spots or localized berm breaching and subsequent inundation).

Incident waves are normally steeper (have a higher ratio between wave height and wavelength) than infragravity waves and are preferentially dissipated by breaking throughout the surfzone. As a consequence, swash oscillations can be dominated by infragravity frequencies (e.g., *Guza and Thornton*, 1982), despite these frequencies typically contribute to a small percentage of the offshore wave spectrum. However, recent observations have shown that dissipation might also limit infragravity wave energy within the surfzone (*Henderson and Bowen*, 2002; *Sheremet et al.*, 2002; *Henderson et al.*, 2006; *Thomson et al.*, 2006; *van Dongeren et al.*, 2007). The mechanisms proposed to explain infragravity losses are still not well understood, and infragravity wave energy exchanges in very shallow water have not been linked to low-frequency runup patterns, despite infragravity runup contributing for much of sediment transport and coastal inundation on low-sloping, dissipative beaches (*Butt and Russell*, 2000).

1.2 Thesis objectives

This thesis explores the causes for temporal and spatial swash variations that are not driven by offshore wave changes but are associated with wave transformations in the surfzone. Within the thesis, I analyse field observations of ocean waves, video observations of swash motions and wave breaking patterns, and beach morphology surveys, collected during two field experiments undertaken on a steep, intermediate beach on the east coast (Tairua Beach) and a low-sloping, dissipative beach located on the west coast of New Zealand's North Island (Ngarunui Beach, Raglan) to investigate the following overall research questions:

1. How does the presence of a sandbar affect the magnitude and spectral features of the swash motions on an intermediate, barred beach?

2. Can alongshore variability in the sandbar morphology cause alongshore runup variability?

3. How do nonlinear wave interactions in shallow water, rather than morphological variations in the sandbar, control the magnitude and frequency distribution of runup on a dissipative beach?

1.3 Thesis structure

These objectives are addressed using datasets from the two field experiments and a combination of image processing and time series data analysis techniques, including a technique developed in this thesis to evaluate the probability of wave breaking dissipation from video images of the surfzone. The three general research questions are broken into three scientific articles, presented respectively in Chapter 2, 3 and 4. These chapters are composed by the three complete articles, each with their own abstract, introduction, methods, results, discussion and conclusions (because the articles were intended to be published in American journals, they were written in American English). Although the articles can stand alone, they systematically address aspects of the same theme of characterising surfzone processes that control runup variability. In Chapter 5, the general conclusions of the thesis are presented, and topics for future research are briefly discussed. Finally, the Appendix presents a conference paper published in the *Proceedings of the Coasts and Ports 2011*, where wavelet analysis is used to investigate non-stationary patterns in swash motions at Tairua. This appendix addresses the central theme of the thesis, by exploring the degree to which wave groupiness, which controls infragravity development, may also contribute to controlling infragravity runup oscillations.

The first research article of this thesis (Chapter 2) is entitled *The effects of tides on swash statistics on an intermediate beach* (*Guedes et al.*, 2011), and has been published in the *Journal of Geophysical Research* in April 2011.

The second article, presented in Chapter 3, is entitled *Observations of alongshore variability of swash motions on an intermediate beach* (*Guedes et al.*, 2012) and has been published in the *Continental Shelf Research* in October 2012.

The third and last article (Chapter 4), entitled *Observations of wave energy fluxes and swash motions on a low-sloping, dissipative beach*, has been submitted to the *Journal of Geophysical Research* in December 2012. This research has been carried out using the dataset from a field experiment that was entirely designed and executed as part of my PhD. During the experiment, field measurements of intertidal beach morphology and ocean waves were obtained. Surface ocean waves were measured offshore and in the surfzone, over different cross-shore positions from the shoreline that were controlled by changes in the tide. A video imagery technique was also employed to measure swash oscillations and estimate cross-shore wave breaking dissipation patterns. Description of the field experiment is provided in Section 4.3.1.

Chapter 2

The effects of tides on swash statistics on an intermediate beach

R. M. C. Guedes, K. R. Bryan, G. Coco, R. A. Holman (2011), The effects of tides on swash statistics on an intermediate beach, *Journal of Geophysical Research*, 116, C04008, doi:10.1029/2010JC006660.

Contribution of authors

Chapter 2 presents the article entitled “The effects of tides on swash statistics on an intermediate beach”, published in April 2011 in the *Journal of Geophysical Research*. This study provides a significant contribution to the scientific field by showing that runup can be strongly controlled by changes to the degree of wave breaking dissipation, caused by the presence of a sandbar and variations in the water depth over its crest.

The dataset analysed in this article was collected by my co-authors prior to the start of my PhD. I processed and analysed all the video, wave and lidar data, including extracting runup signals from the video. I wrote the numerical code to perform the processing and statistical analyses, prepared all the figures and wrote the initial and subsequent drafts of the article. My co-authors edited drafts, provided advice on direction, and editorial help with the response to the reviewer’s comments.

Abstract

Swash hydrodynamics were investigated on an intermediate beach using runup data obtained from video images. Under mild, near-constant, offshore wave conditions, the presence of a sandbar and the tidally-controlled water depth over its crest determined whether most of the incoming waves broke before reaching the shoreline. This forced a change in the pattern of wave energy dissipation across the surf zone between low and high tide, which was reflected by changes to swash on time-scales of a few hours. Significant runup height (*Rs*, defined as 4 times the standard deviation of the waterline time series), was found to vary by a factor of 2 between low tide, when most of the waves were breaking over the sandbar (Rs/Hs~1.5, where *Hs* is the offshore significant wave height) and high tide, when the waves were barely breaking (Rs/Hs~2.7). The increase in wave energy dissipation during low tide was also associated with changes in swash maxima distribution, a decrease in mean swash period and increasing energy at infragravity frequencies. Bi-spectral analysis suggested that this infragravity modulation might have been connected with the presence of secondary waves.

Keywords: swash, tide, nearshore, wave breaking, sandbar, video imagery.

2.1 Introduction

The swash zone is the interface between land and ocean where the waves intermittently cover the beach. The time-varying location of the shoreline water level within this region, usually termed runup (*Guza and Thornton*, 1982; *Holman and Sallenger*, 1985; *Ruggiero et al.*, 2004) defines the cross-shore extent and the elevation that can be flooded for a specific tidal level. Runup is of great importance for coastal planners, who want to define appropriate and practicable shoreline setback criteria, for coastal engineers, who are interested in designing coastal structures, and for researchers studying the physical processes contributing to beach erosion/accretion (*Butt and Russell*, 2000*; Elfrink and Baldock*, 2002).

Runup is commonly decomposed into a quasi-steady super elevation above the still water level, (setup) and the fluctuations about such super elevation (swash) (*Guza and Thornton*, 1982; *Holman and Sallenger*, 1985; *Stockdon et al.*, 2006). The swash is composed of two distinct phases, an upslope, landward-directed, flow (usually called uprush) and a downslope, seaward-directed flow (normally known as backwash). Although there is a continuum of energy in swash spectra, they are commonly divided into incident (0.33 to 0.05 Hz) and infragravity frequencies (0.05 to 0.003 Hz). The incident band is normally more energetic in bore-dominated, steeper intermediate and reflective beaches (*Holland and Holman*, 1993; *Raubenheimer and Guza*, 1996), while low-sloped dissipative beaches have been observed to have most of the swash variance within infragravity frequencies (*Ruessink et al.*, 1998; *Ruggiero et al.*, 2004).

Swash characteristics depend on whether the incident waves reflect at the shoreline, or are dissipated offshore by breaking. Traditionally, infragravity waves are considered more likely to reflect (*Miche*, 1951) than waves whose spectra are dominated by the incident band. Nevertheless, recent measurements and modelling results have shown that the surf (*Henderson and Bowen*, 2002; *Sheremet et al.*, 2002; *Thomson et al.*, 2006; *van Dongeren et al.*, 2007) and swash (*Battjes et al.*, 2004) can be zones of infragravity dissipation. *Miche* (1951) hypothesized that under dissipative conditions runup will be saturated, and thus a maximum runup amplitude will be reached when the incident waves are just high enough to break. Further increase in offshore wave height increases the wave steepness and makes the waves break, dissipating their energy rather than reflecting it. Many field investigations on broadbanded swash have been interpreted based on Miche's saturation hypothesis. *Huntley et al.* (1977) calculated the spectra from vertical runup time series obtained in three different natural beaches and found the incident band to be saturated. This implies that the energy at the incident bands is proportional to β^4 and f^{-4} (where β is beach slope and f is wave frequency) and independent of wave height. Some works (e.g. *Mase,* 1988; *Ruggiero et al.*, 2004) have found a similar spectral shape for the saturated band of runup, whereas an f^{-3} dependence has been observed by others (e.g. *Guza and Thornton,* 1982; *Ruessink et al.*, 1998; *Ciriano et al.*, 2005). The implications of different rates of incident energy decay are still not clear and it has been suggested that they might simply be related to different measurement methods (*Raubenheimer and Guza*, 1996). *Guza and Thornton* (1982) measured swash oscillations on a mildly sloped beach and calculated the variance levels for incident and infragravity spectral ranges. Although incident swash energy was found to be independent of offshore wave height H (i.e. the wave field was saturated), positive linear correlation was observed between H and low frequency energy at the shoreline, showing that the low-frequency component of the swash increases with increasing wave height in non-monochromatic conditions, a behaviour subsequently confirmed in other field studies (e.g. *Holman and Sallenger,* 1985; *Raubenheimer and Guza,* 1996; *Ruessink et al.*, 1998; *Ruggiero et al.*, 2004).

The amplitude of incident swash oscillations has been shown to scale well with the non-dimensional Iribarren number:

$$\xi_0 = \frac{\beta}{\left(H_0 / L_0\right)^{1/2}} \tag{2.1}$$

where H_0 and L_0 are deep water wave height and wavelength. *Miche* (1951) suggested that when ξ_0 is high, waves reflect at the shoreline and the swash has larger amplitudes, while for low ξ_0 the waves break and saturation conditions are expected. Field data have confirmed a linear relationship between the Iribarren number and incident runup height, especially for steeper intermediate and reflective beaches (e.g. *Holman and Sallenger,* 1985; *Holman,* 1986; *Raubenheimer and Guza*, 1996; *Stockdon et al.*, 2006). However, substantial variability is often observed around such relationship, possibly owing to other parameters affecting runup which are not accounted for by ξ_0, and also because the definition of a single value for beach slope might not be appropriate on some natural beach, where complex morphological features such as sandbars are often present (*Holman and Sallenger*, 1985).

A potential source of variability in runup characteristics could be related to the presence of tides whose variations modulate a number of wave-related processes in the nearshore. For example, the breaking of waves inside the surf zone is a strong function of depth (*Peregrine*, 1983), and hence is likely to be modulated by the tide. Moreover, the presence of one or more sandbars in the surf zone will determine the characteristics of this breaking (e.g. *Lippmann and Holman*, 1989; *van Enckevort and Ruessink*, 2001; *Aarninkhof et al.*, 2005; *Haller and Catallán*, 2009) and is therefore likely to affect swash hydrodynamics. However, the emphasis on offshore characteristics and beach slope introduced with *Miche* (1951) has meant the effects of sandbars in controlling the characteristics of runup have not been fully explored. The tidal influence in breaking will also control radiation stress gradients which are a function of the wave height gradients, and so long-shore current forcing will also be modulated at the tidal frequency inside the surf zone (*Thornton and Kim*, 1993). Similarly, rip currents have been observed to be stronger at low tide (*MacMahan et al.*, 2006). Offshore of the breaking area, *Okihiro and Guza* (1995) observed infragravity energy within frequency bands of 0.01 and 0.04 Hz to decrease at low tide, which was hypothesized to be a result of changes in infragravity energy generation and propagation on the concave beaches onshore of the observations. In the surf zone, *Thomson et al.* (2006) observed similar modulations and attributed them to nonlinear energy transfers from low-frequency to higher-frequency motions, which were enhanced over the relatively flatter inner surf zone bottom profile at low tide.

The aim of this work is to investigate the degree to which changes in swash hydrodynamics can also be related to tidal variations and the presence of a submerged sandbar on an intermediate beach. We use a dataset of swash oscillations obtained on a natural beach during a period of mild nearly-constant offshore wave conditions when the amount of wave breaking was clearly modulated by the tide and we show that some characteristics of swash such as amplitude, incident/infragravity variance levels and swash maxima distribution were also tidally-modulated.

2.2 Methods

2.2.1 Field site

The field experiment was undertaken between 15 and 17 of July in 2008 at Tairua Beach, a 1.2 km-long pocket beach located on the Pacific coast of New Zealand (Figure 2.1). This medium–coarse grained beach has a fairly steep beach face slope of about 0.1 and is exposed to medium wave energy with average offshore significant wave height and mean spectral period of 0.9 m and 5.8 s (*Gorman et al.*, 2003). The tides are semi-diurnal, with tidal ranges between 1.2 (neap) and 2 m (spring tides) and the system is normally classified as intermediate, with a rhythmic sandbar and strong rip currents often present (*Bogle et al.*, 2000). During the 3-day period of the experiment, the sandbar remained remarkably alongshore uniform, at a cross-shore distance of about 80 m from the shoreline (see the white alongshore bands in Figure 2.2 which are associated with the locations of preferred wave breaking over the sandbar and shoreline) and with water depths over the crest, estimated using the method developed by *Plant et al.* (2008), changing from about 1.1 to 2.2 m from low to high tide.

2.2.2 Field measurements

The dataset presented here is composed of measurements of offshore hydrodynamic conditions, beach face topography and video images. The hydrodynamic variables were measured using an ADCP deployed at a water depth of about 12 m. Time series of subsurface pressure were recorded every hour for 20 min, at 2 Hz and converted to free surface elevation using linear theory. Offshore significant wave height Hs was calculated as 4σ where σ is the standard deviation of the free surface time series. Peak period Tp was determined as the inverse of the peak frequency from the spectrum. Hourly mean water level η was calculated as the mean of each time series and adjusted to the local vertical datum. Peak direction was determined from the directional velocity spectrum obtained by the 4 independent acoustic sensors of the ADCP.

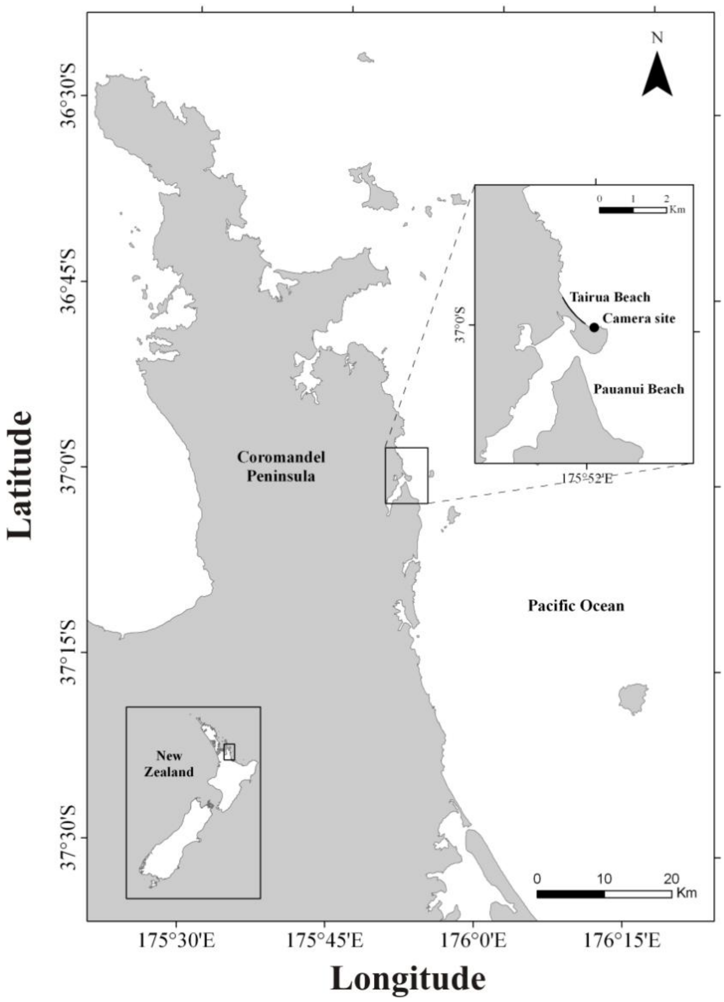

Figure 2.1. Field site location.

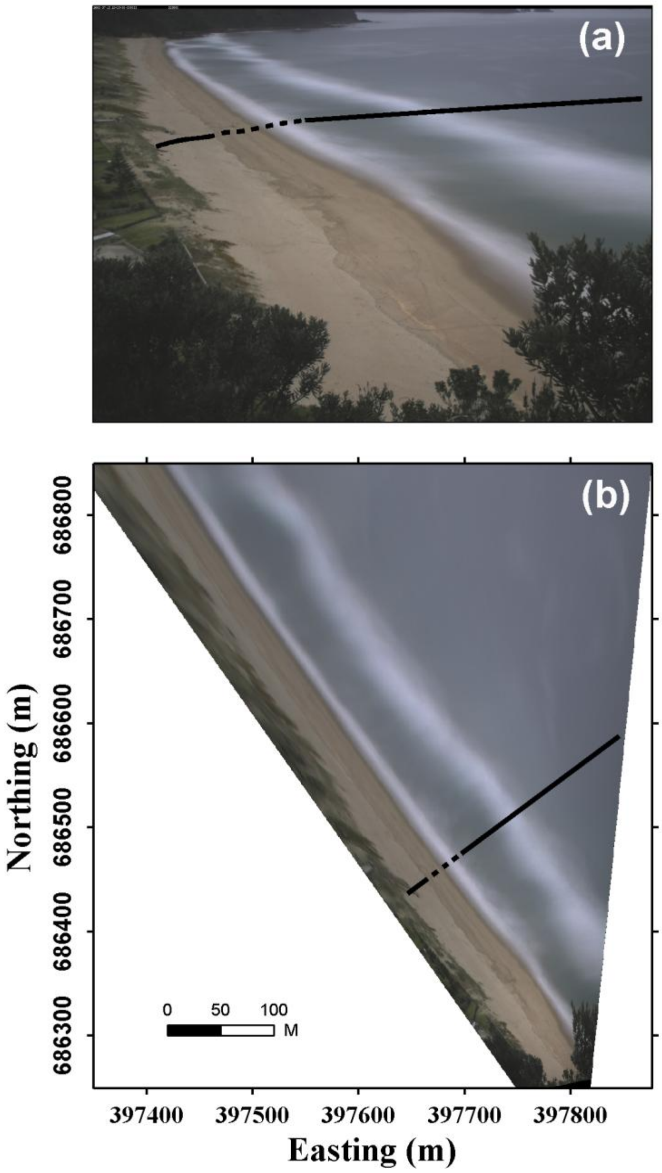

Figure 2.2. (a) Oblique image obtained at Tairua Beach on 16 July 2008 at 11.00 by averaging 600 individual frames recorded at 2 Hz. (b) The same image rectified to a planview using known geometric transformations. Black lines represent cross-shore transect where time stacks were created and location where the beach profile was surveyed (cross-shore range of the swash over the 3 days of field experiment is highlighted by the dashed lines).

A cross-shore beach profile was surveyed using a total station on July 17th, covering a cross-shore distance of 55 m between the backshore and the swash zone (Figure 2.3). The profile was extended offshore of the most seaward surveyed location by extending the linear fit through the lowermost measured points to create a profile that extended just beyond the likely lowermost location

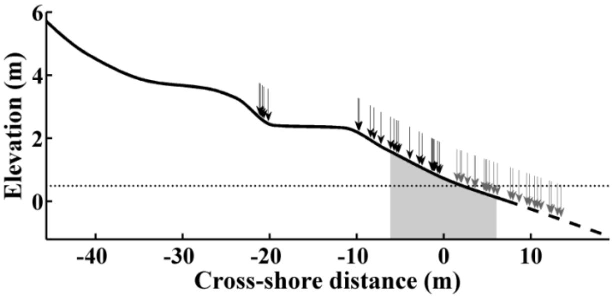

Figure 2.3. Beach profile surveyed at Tairua Beach on 17 July 2008 (solid line) with extension calculated as the line fit through the lowermost measured points (dashed line). Mean swash positions for the 25 data runs are delimited by the gray patch. Location of mean + (-) 2σ of swash positions for the 25 data runs are highlighted by the black (gray) arrows. Dotted line at elevation of 0.5 m indicates still water level (i.e. setup not included) above which the 'step' between cross-shore positions of -20 and -10 m starts to become important for the swash (see text). Elevations are relative to New Zealand Geodesic Datum (NZGD). Cross-shore distances have origin at mean swash location for the 25 data runs and increase offshore.

of low-tide swash elevation. The along-shore position of the profile is shown by the location of the black lines in Figure 2.2. Foreshore slope β was calculated as the best linear fit of the measured profile between the locations of mean ± 2 standard deviations of the shoreline positions for each data run (95% of the data points assuming a Gaussian distribution).

High-resolution images (1528 x 2016 pixels) were acquired continuously at 2 Hz during the daylight hours (e.g. Figure 2.2a), using a digital camera mounted at the southern end of the beach (Figure 2.1) at approximately 42 m above the sea level. Runup oscillations were extracted using a technique known as 'time stack' (*Aagaard and Holm*, 1989), which consists of time series of pixel intensity, sampled along a cross-shore line defined on the images. The time stacks were created by determining the image coordinates of the measured cross-shore beach profile (e.g. Figure 2.2a) and collecting the values of light intensity at these coordinates into a row in the time stack matrices. Conversions between image coordinates and ground coordinates were made using the colinearity equations described by *Holland et al.* (1997) with corrections for lens distortions (e.g.

Figure 2.2b). The vertical resolution of this technique, estimated by mapping the horizontal resolution to an elevation along the profile within the swash zone, varied mainly as a function of beach slope and was less than 3 cm (on average 1 cm). The dataset was broken into hour-long time series, resulting in 25 time stacks created during the 3 days, with typically 7200 individual frames sampled in each.

2.2.3 Data analysis

The swash location was defined as the most shoreward edge of water identifiable on each line of the time stacks. It has been shown that this definition is consistent with swash measurements obtained using resistance wires deployed near-bed (*Holman and Guza*, 1984; *Holland et al.*, 1995). The edge was detected using an image processing algorithm, developed to distinguish the sharp contrast observed between the swash front, typically characterized by the presence of white foam, and the darker sandy beach. Manual refinements were required in some images where the algorithm failed, which mostly happened due to poor contrasts arising from the absence of foam at the swash location, especially during the run-down phases of the swash cycles. Examples of digitized swash locations are shown in the time stacks obtained on 16 July 2008, at 16.30 during high tide (Figure 2.4a) and at 12.30 during low tide (Figure 2.4b). Time series of vertical runup elevation Rv were derived from the digitized swash locations since the cross-shore beach topography at the time stack location was accurately known from the surveyed profile.

Swash statistics were calculated from the 25 hourly time series of runup elevation. Significant runup height Rs was estimated as 4σ of the linearly detrended time series. Swash maxima ζ (e.g. Figure 2.4) were identified following *Holland and Holman* (1993) as the difference in elevation between any local crest and the setup level (mean level $\bar{z}$ of each time series). The local maxima were extracted using a modified version of the zero-crossing method. The time series showed clear evidence of patterns of smaller and larger waves, consistent with the broadband behavior that typically characterizes the swash, in which case standard zero-crossing analysis would not detect the smaller waves. We devised an objective method of detecting these smaller waves. The zero-crossing analysis was repeated 18 times, each time varying the zero-level by 0.2σ increments to a maximum/minimum of $\pm 1.8\sigma$, each addition adding new waves to the result. The number of times the analysis was repeated was determined by the point at which changing the zero-level no longer influenced the number of waves detected.

Power spectra were calculated from each linearly detrended runup elevation time series, segmented into sections of 512 s (resulting in a bandwidth of 0.00195 Hz) and tapered with a Hanning window (50% overlap), giving typically 18 degrees of freedom. The energy density was partitioned into high ($f > 0.05$ Hz) and low frequency bands ($f \leq 0.05$ Hz) to account for the variance at incident and infragravity regions, respectively.

The amount of breaking waves was estimated as the probability of breaking for each cross-shore location on the time stacks, based on the difference in pixel intensity between regions with (i.e. brighter pixels) and without the presence of foam (i.e. darker pixels). Thresholds were defined to separate breaking from non-breaking pixels and create binary time stacks (e.g. Figure 2.4c), from which the probability of breaking of each cross-shore location was calculated. The thresholds were defined by randomly sampling pixel intensity values over regions visually identified as breaking and non-breaking in each time stack, and calculating the average between the lowest ‘breaking’ and the highest ‘non-breaking’ pixel intensities. This method does not distinguish the foam associated with the breaking wave roller from the residual foam left on the surface of the water after the waves break. However, the latter is also expected to be more frequent as wave breaking increases and this parameter is only used as a relative measure of breaking between high and low tide.

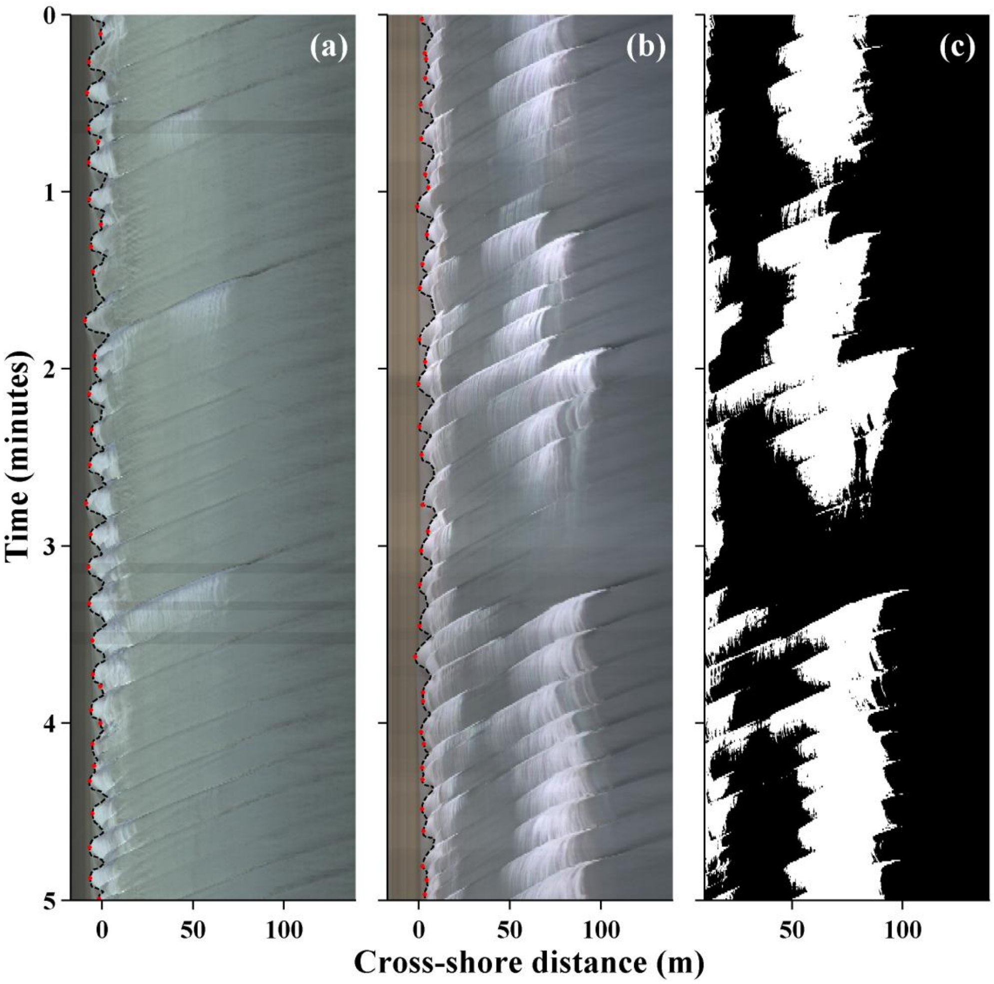

Figure 2.4. 5-min fragments of the time stacks obtained at Tairua Beach on 15 July 2008, at 15.30 near high tide (a) and on 16 July 2008, at 11.30 near low tide (b). (c) Binary time stack obtained from (b) to quantify breaking using the method described in Section 2.2.3 Time increases from top to bottom of the images. Cross-shore distances have origin at mean swash location for the 25 data runs and increase offshore (see Figure 2.3). Dashed lines and red dots on first two panels are digitized swash locations and located swash maxima, respectively. Sloping lines in the time stacks represent individual waves propagating towards the shoreline. Notice the stronger breaking (presence of white foam at cross-shore distances 50–100 m) for the time stack collected at low tide.

2.3 Results

2.3.1 Hydrodynamic conditions

An overview of the hydrodynamic conditions experienced during the field experiment is given in Figure 2.5. The offshore wave parameters barely changed, with gently-sloping waves ($0.003 < H_0/L_0 < 0.005$) coming from east/northeast with $Hs < 1$m and Tp between 10 and 12 s (Figure 2.5a–c). The video recordings spanned 3 partial tidal cycles that ranged in elevation between -0.51 and 0.65 m, with time stacks obtained over 2 high tides and 3 low tides (Figure 2.5d). Beach slope obtained from the profile shown in Figure 2.3 changed from 0.09 to 0.13 due to tidal-induced changes in water level moving the swash zone to different parts of the beach face (Figure 2.5e, circles). In general, beach slope follows the same trend as the tide for the time series in which $\eta < 0.5$ m (i.e. the swash zone was placed over the concave section of the profile, where cross-shore position was greater than -10 m in Figure 2.3). Higher tidal levels, however, resulted in the swash being located in the flat section of the profile (the step between cross-shore positions -20 and -10 m, where β decreases). Iribarren number was mostly conditioned by changes in foreshore slope and ranged from 1.39 to 2.16 (Figure 2.5e, pluses), which characterizes reflective conditions and which is within the range of values reported by other authors (e.g. *Raubenheimer and Guza*, 1996). Significant runup height changed by almost a factor of 2, from 1.2 (1.5Hs) to 2.2 m (2.7Hs) and displayed a consistent relationship with tidal levels (Figure 2.5h).

2.3.2 Swash statistics

The effects of environmental variables on swash oscillations were investigated by regressing Rs against Hs, ξ_0 and η. Scatter plots of the regressions and correlation results are shown in Figure 2.6 and Table 2.1, respectively. No significant linear

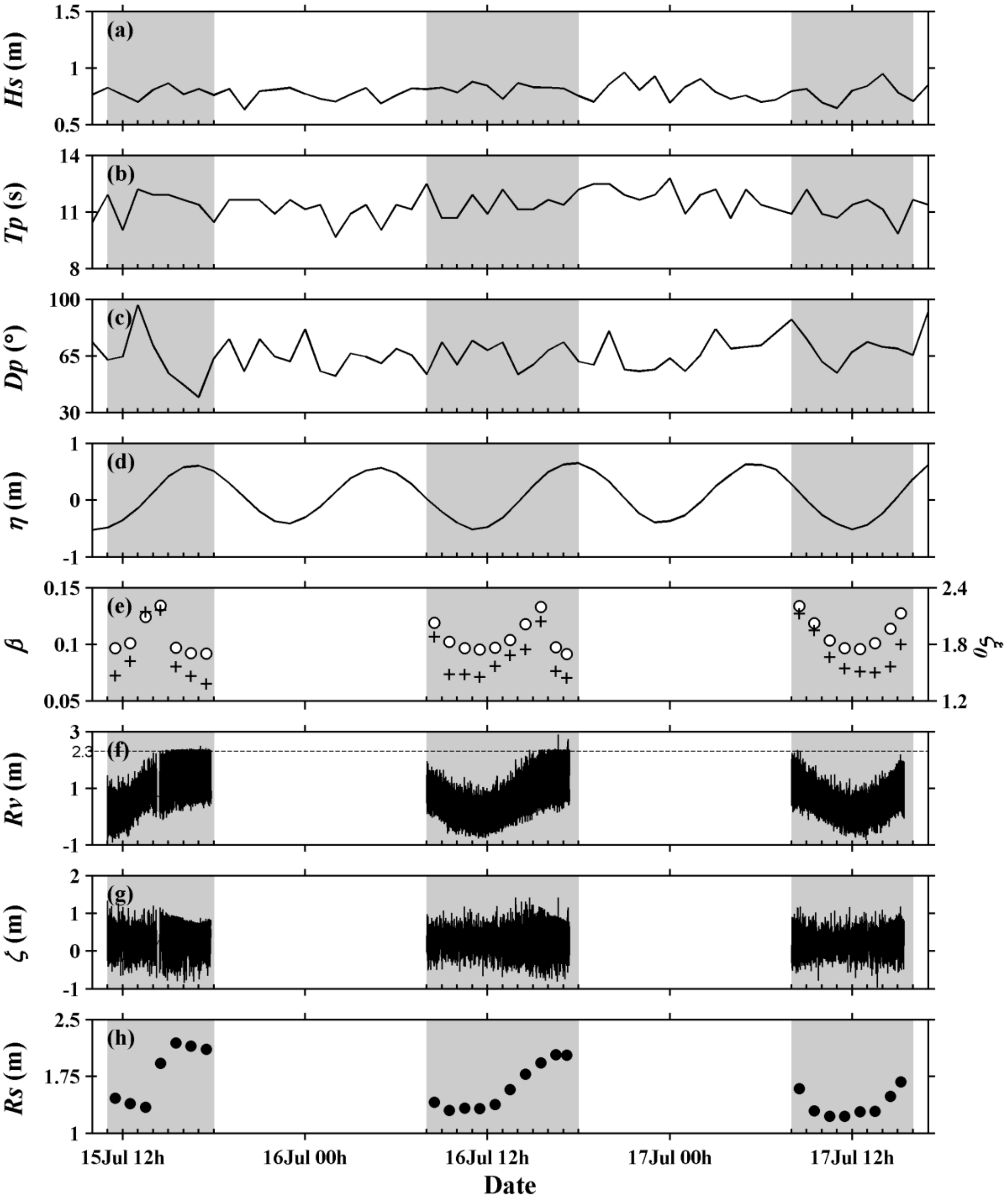

Figure 2.5. Time series of hydrodynamic and morphological parameters. Offshore characteristics (calculated hourly using the ADCP at 12 m depth): (a) significant wave height; (b) peak wave period; (c) peak wave direction; (d) mean sea level. (e) Beach slope calculated as the best linear fit of the measured profile between the locations of mean ± 2σ of the shoreline positions for each data run (circles, left axis); Iribarren number calculated using Equation 2.1 (pluses, right axis). (f) Time series of runup elevation relative to NZGD (solid line) with horizontal dashed line at 2.3 m highlighting elevation of beach step. (g) Time series of swash maximum relative to the mean (setup) level of each time series. (h) Significant runup height calculated hourly using the time series of runup elevation. Gray patches indicate daylight periods when the images were acquired.

relation (at the 99% confidence level) was observed between significant runup height and offshore significant wave height, which was expected given the small range of *Hs* during the experiment. This is also consistent with *Howd et al.* (1991) who found the magnitude of the incident band measured in the trough to be a strong function of tide due to depth-dependent saturation over the crest. The lack of dependence of *Rs* on ξ_0, on the other hand, is somewhat surprising, considering the strong dependency of runup on both ξ_0 and β reported in previous laboratory (*Mase*, 1988) and field studies (*Holman and Sallenger*, 1985; *Ruggiero et al.*, 2004). Nevertheless, there is a positive trend between runup and ξ_0 when the values obtained during high tide (runs 5–7, 16–17) are excluded from the analysis. Note that the beach slope drops considerably for these data runs while the runup height reaches the highest levels (Figure 2.5). This pattern is still more evident by regressing *Rs* against β as the correlation coefficient r^2 jumps from ~0 to 0.52 when the high-tide runs are excluded from the analysis (not shown). The regression results emphasize that the main control on runup was the tide (r^2 between *Rs* and η amounted to 0.88, significant at the 99% confidence level). It is difficult though to evaluate the contribution of the local slope to this relationship because the concave shape of the beach means that the influence of the slope would follow the same tidal trend below the beach step.

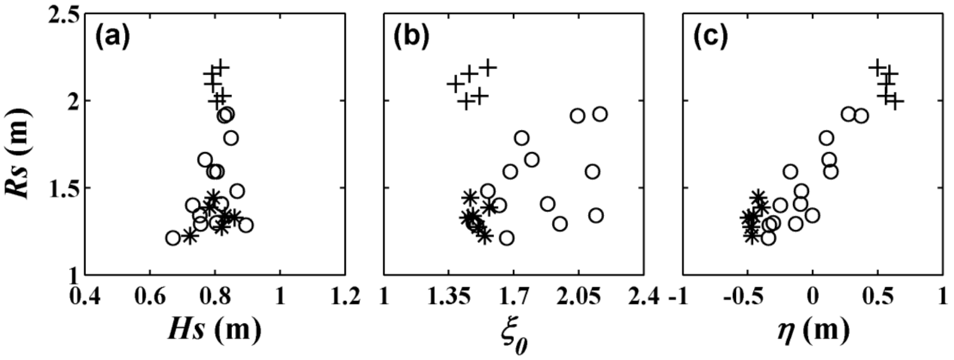

Figure 2.6. Regression plots of significant runup height *Rs* as a function of (a) offshore significant wave height, (b) Iribarren number and (c) tidal level. Asterisks, circles and crosses represent statistics from time series obtained during low tide (runs 1, 10–12, 21–22), mid tide (runs 2–4, 8–9, 13–15, 18–20, 23–25) and high tide (runs 5–7, 16–17), respectively.

Table 2.1. Results of regression analysis.

Y	**X**	**m**	**b**	**r^2**
Rs	*Hs*	*1.59*	*0.32*	*0.06*
Rs	ξ_0	*-0.03*	*1.64*	*0*
Rs	η	*0.8*	*1.61*	***0.88***

$Y = mX + b$. Correlation coefficient squared r^2 significant at the 99% confidence level showed in bold.

In addition to the runup statistics, the swash maxima distribution P(ζ), shown in Figure 2.7 was also found to change systematically over the different levels of tide. During low tide (e.g. time series 1, 10 and 22) P(ζ) was slightly positive-skewed (i.e. higher proportion of smaller waves). At the intermediate levels of tide (e.g. time series 2, 8, 13 and 19) P(ζ) tended to assume a Gaussian distribution but became more and more negative-skewed as the tide increased. Finally, during high tide (time series 5–7, 16–17) the swash maxima distribution was consistently negative-skewed, with relatively few low waves compared to the other stages of tide. The dependence of skewness of swash maxima on tide is highlighted in Figure 2.8. The highly-skewed distributions observed at high tide resemble cut off Gaussians at elevations correspondent to the flat part of the beach profile (step) between cross-shore positions of -20 and -10 m (Figure 2.3; see also Figures 2.5f and 2.5g). The effect of the step on the swash distribution was assessed by deriving runup elevation time series with a synthetic profile, where a linear fit of the lower beach face was extended shoreward over the beach step. The flat-beach-corrected distributions, shown by the solid lines in Figure 2.7, are significantly different than the uncorrected statistics for the rightmost, high-tide panels, although they do not differ significantly over the other stages of tide.

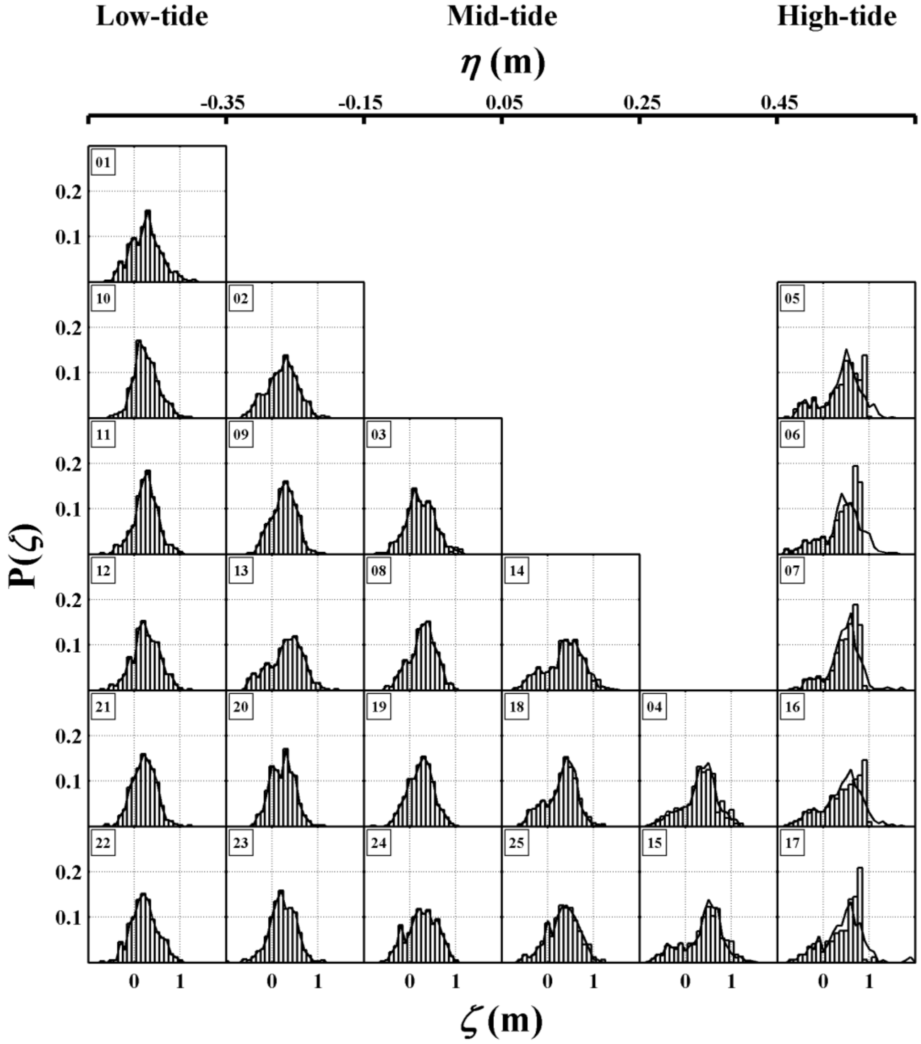

Figure 2.7. Swash maxima distribution P(ζ), calculated for the 25 runup time series. The bars represent the distributions associated with the real time series and the solid lines represent those obtained from time series derived by using a synthetic profile, where a linear fit of the lower beach face was extended shoreward to replace the beach step between cross-shore positions of -20 and -10 m. Each individual panel has been sorted according to the tidal level η (top axis) associated with the respective run, which is indicated by the numbers in the top-left corners.

Time series of offshore and shoreline power spectra are shown in Figures 2.9a and 2.9b. Although both time series show little energy at the unsaturated infragravity frequencies, the swash spectra has a tidally-modulated peak at incident frequencies (between 0.07 and 0.09 Hz) that increases in energy with the tide, with the power ranging by an order of magnitude between high and low tide. This modulation does not happen offshore, where the spectral peak is centered at virtually the same frequencies as the runup spectra but the energy levels barely change with the tide. Conversely, the energy in the swash spectra at infragravity frequencies tends to increase from high to low tide, although virtually no energy at infragravity frequencies can be observed in 12 m depth. Whereas no tidal-modulation in the offshore spectrum can be observed, the wave energy within the surf zone is obviously controlled by wave breaking according to the level of tide (Figure 2.9c). As the tide goes down, the waves start to break farther from the shoreline and the probability of breaking around the location of the sandbar increases. The majority of the waves were breaking during the lowest water levels which implied higher dissipation of the incident wave energy (consistent with observations of the swash spectra).

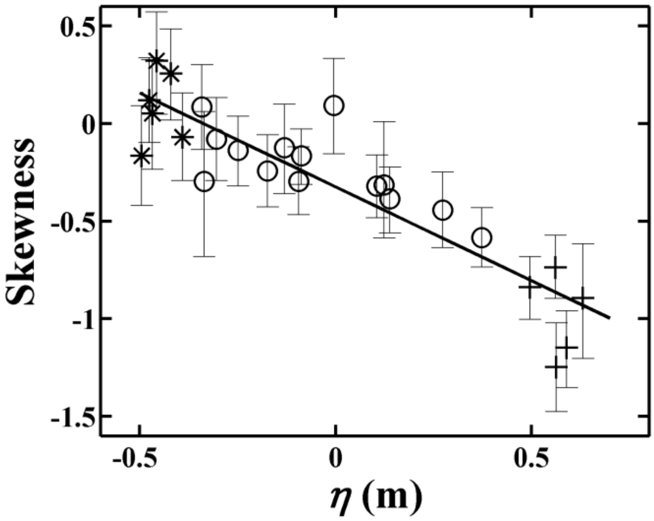

Figure 2.8. Skewness of swash maxima (γ) as a function of tidal level. Solid line represents the best linear fit given by the equation $\gamma = -0.96\eta - 0.32$ ($r^2 = 0.81$, significant at the 99% confidence level). Asterisks, circles and crosses represent statistics from time series obtained during low tide (runs 1, 10–12, 21–22), mid tide (runs 2–4, 8–9, 13–15, 18–20, 23–25) and high tide (runs 5–7, 16–17), respectively. 95% confidence bars were defined for each skewness estimate using a bootstrap technique in which 3000 new samples, drawn with replacement from the actual sample, were computed using a Monte Carlo algorithm. The confidence limits were estimated from the distribution of the skewness associated with these bootstrap samples, for each of the 25 sets of swash maxima.

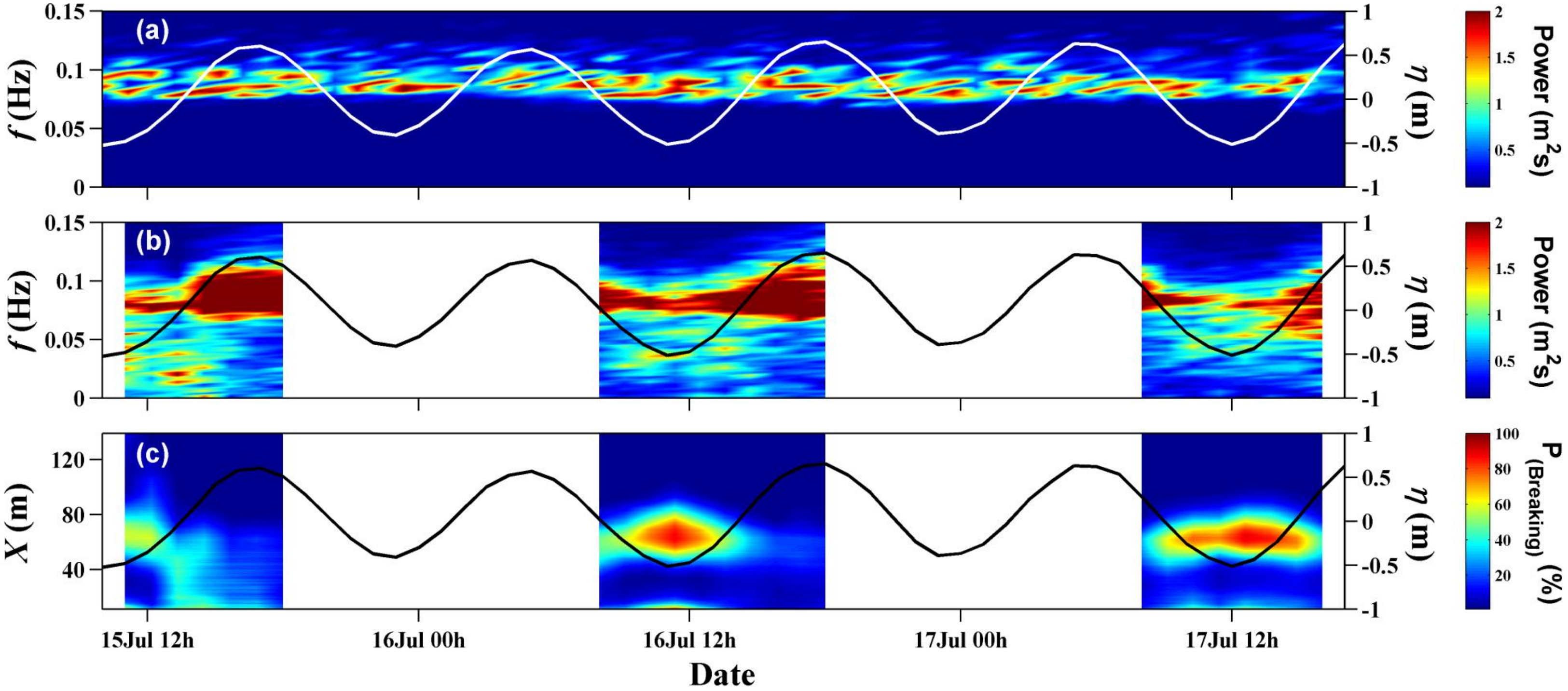

Figure 2.9. Time series of hydrodynamic properties with solid line in each panel (right axis) representing tide level. (a) Offshore wave spectrum time series calculated from the pressure time series recorded by the ADCP at 12 m depth. (b) Runup spectrum time series calculated from the runup time series. (c) Probability of breaking time series calculated as the probability of exceedence of a pixel intensity threshold that characterized the presence of foam on the time stacks for each cross-shore pixel location. Cross-shore distances have origin at mean swash location for the 25 data runs.

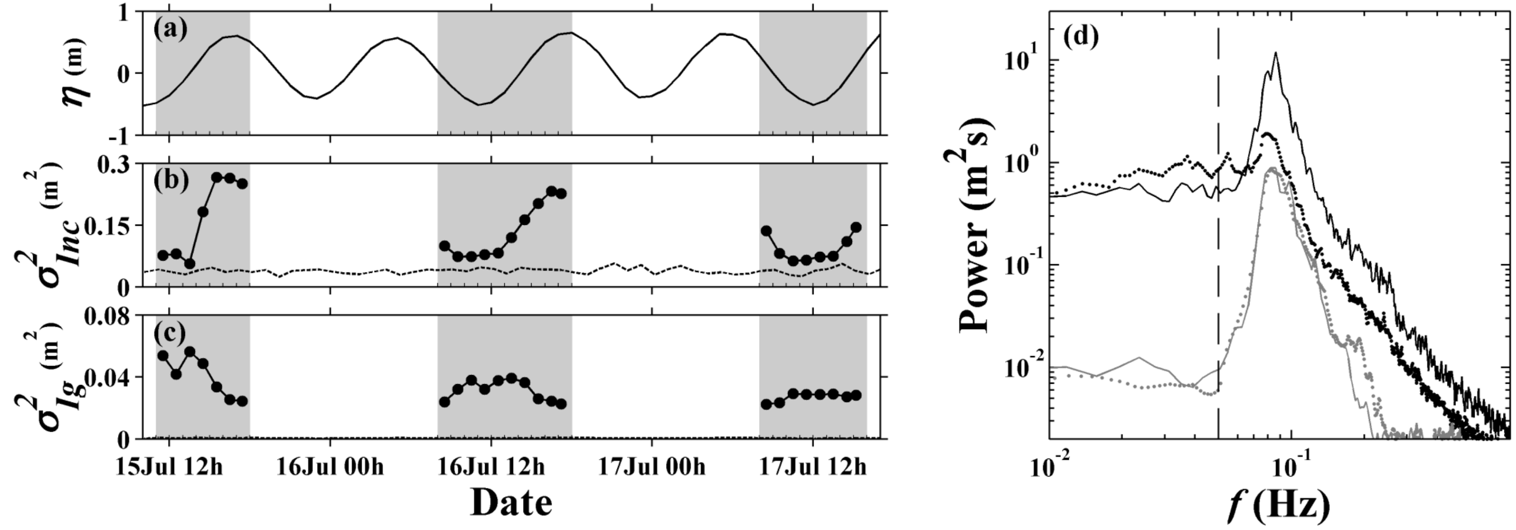

Figure 2.10. (a) Tide levels. (b) Runup (solid line with circles) and offshore (dotted line) variance σ^2 at the high (> 0.05 Hz) frequency region. (c) Runup (solid line with circles) and offshore (dotted line) variance at the low (≤ 0.05 Hz) frequency region (offshore variance at the low region is hardly seen due to low values). Gray patches indicate daylight periods when the images were acquired. Note the different scales for σ^2 at high and low frequencies. (d) Average of spectra obtained during low tide (runs 1, 10–12, 21–22, dotted line) and high tide (runs 5–7, 16–17, solid line), plotted on a log-log scale (runup spectra are shown in black, offshore spectra in gray). Vertical dashed line highlights frequency used to separate incident and infragravity variances.

2.4 Discussion

2.4.1 Spectral analysis

We observed tidally-modulated changes in the degree of wave breaking over the sandbar to have major implications to the properties of the swash spectrum. Figure 2.10 shows the swash and offshore variances partitioned into incident and infragravity frequencies and also the swash and offshore spectra averaged over low and high tide. At the incident band, not only was the magnitude of the peak affected by changes in wave breaking (Figures 2.9b, 2.10b and 2.10d), but also the rate of energy decay. The slope of the saturated region of the spectrum, estimated by the best linear fit of the energy density between the peak frequency and 0.3 Hz (on a log-log scale) decayed at rates that varied between f^{-4} and f^{-3}, with the steeper roll-offs normally associated with the mid-high tide, peaked spectra (Figure 2.11). Although in previous studies the differences in energy decay rate with increasing frequency have been attributed to different methods of runup detection (*Guza and Thornton*, 1982; *Raubenheimer and Guza*, 1996), it is possible that, for the present dataset, the dominant effect is modulation of the degree of incident energy dissipation over the bar and the lowering of the incident spectral peak at low tide.

In contrast to the energy at the incident band, the energy at infragravity band of the swash spectrum was enhanced at the lower stages of tide, even though offshore energy at infragravity frequencies was very low and not observed to be tidally-modulated as in other datasets (e.g. *Okihiro and Guza*, 1995; *Thomson et al.*, 2006). It is apparent in Figures 2.9 and 2.10 that the overall energy in the swash is being predominantly controlled by dissipation at incident frequencies, which have variance levels of about an order of magnitude higher than infragravity levels at high tide. However, infragravity variance tends to increase as the tide decreases and eventually energy levels at these two regions of the spectrum become of the same order of magnitude at low tide, suggesting that part of the energy lost from the incident band is not being dissipated but transferred to infragravity frequencies.

Our observations are consistent with many other studies (e.g. *Masselink*, 1995; *Ruessink*, 1998a; 1998b; *Baldock and Huntley*, 2002; *Janssen et al.*, 2003; *Baldock*, 2006, among others) showing that wave breaking, in our case modulated by tides, is key to the increase of infragravity energy in the surf zone (and therefore swash). This is also consistent with the two most widely accepted mechanisms for infragravity generation as they both rely on wave breaking, either as a release of the onshore propagating bound wave, originated from gradients in radiation stress within wave groups (*Longuet-Higgins and Stewart*, 1964) or through the modulation in the breakpoint position (*Symonds et al.*, 1982; *Lippmann et al.*, 1997).

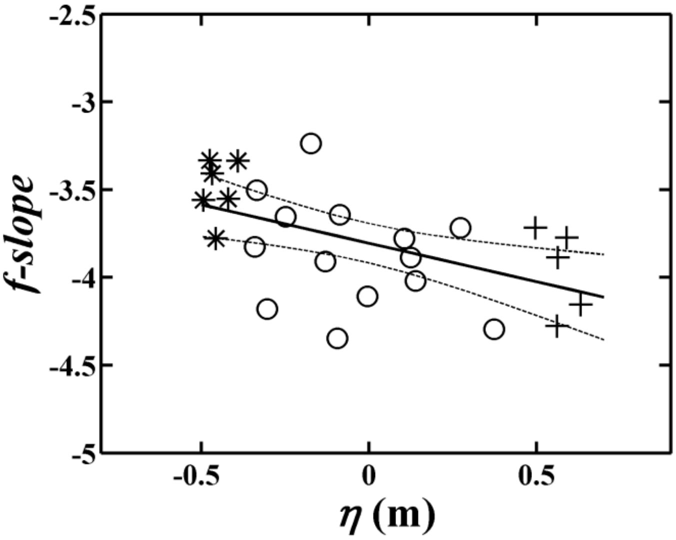

Figure 2.11. Regression plot of the slope of the saturated band of the runup spectra on a log-log scale *f*-slope as a function of tidal level, with the solid line representing the best linear fit given by the equation *f-slope* = $-0.44\eta - 3.8$ ($r^2 = 0.29$, significant at the 99% confidence level). Asterisks, circles and crosses represent statistics from time series obtained during low tide (runs 1, 10–12, 21–22), mid tide (runs 2–4, 8–9, 13–15, 18–20, 23–25) and high tide (runs 5–7, 16–17), respectively. The 95% confidence interval for the regression analysis is shown by the dashed lines.

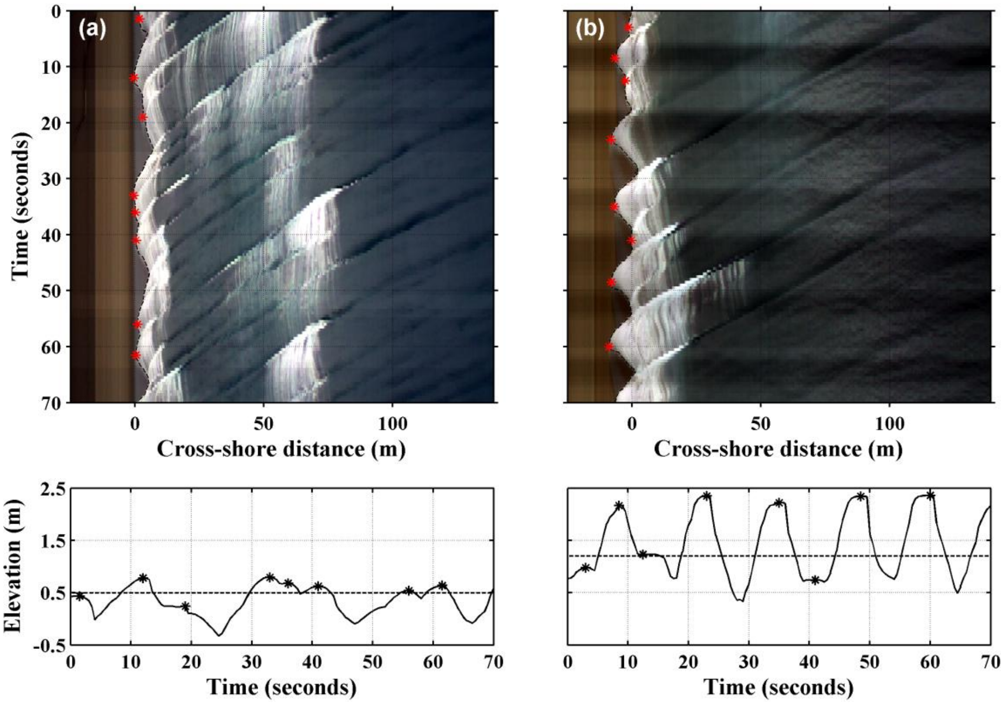

Figure 2.12. 70-sec fragments of time stacks obtained at Tairua Beach on (a) 17 July 2008, at 10.30 during mid-low tide and on (b) 16 July 2008, at 15.30 during mid-high tide (top panels) with the respective time series of vertical runup elevation (bottom panels). Asterisks highlight the detected swash maxima. Dashed lines on top panels are digitized swash positions. Horizontal dashed lines on bottom panels are mean runup elevation (setup level) for each hour-long time series. Elevations are relative to NZGD. Cross-shore distances have origin at mean swash location for the 25 data runs and increase offshore.

Although the mechanisms mentioned above might have been associated with infragravity forcing in the surfzone at low tide, we observed in our data that secondary waves (with higher frequencies than incident) occurred at low tide when the infragravity energy increased (Figure 2.12a). The incident and secondary waves appear to combine at the beach face to modulate low-frequency oscillations. As can be seen in Figure 2.12a, there is an increasing number of wave crests shoreward of the sandbar location (~80 m) at low tide. These waves can be followed propagating towards the shoreline, where eventually they start climbing on the beach face before the backwash of the previous waves starts to take place. Although it is difficult to establish whether bore-bore interactions between these individual waves combine to result in runup time series characterized by higher energy at infragravity frequency, we notice that at high tide, where the increasing number of wave crests is not evident (Figure 2.12b), the infragravity signal disappears, and the oscillations at the shoreline are dominated by the incident peak (T~12 s).

The increase in the number of wave crests shoreward of the sandbar at the lower stages of tides could be a result of the decomposition of the primary wave motion into higher-frequency secondary waves over the bar. The generation of these secondary waves, as the primary motions propagate over the sandbar, has been previously reported in both laboratory (*Beji and Battjes*, 1993) and field experiments (*Elgar et al.*, 1997; *Masselink*, 1998; *Sénéchal et al.*, 2002), and according to *Masselink* (1998), might be a common process on barred beaches. *Beji and Battjes* (1993) showed that an increasing nonlinear transfer of energy between the primary and phase-locked, harmonic frequencies occurs as the waves propagate over the seaward, sloping-face of the sandbar, becoming even stronger as they cross the flat section of it due to triple resonant interactions, and that these harmonics might be eventually released along the deepening shoreward section of the bar due to amplitude dispersion. It appears that these secondary waves might be important in controlling swash hydrodynamics, especially during low tide when the incident peak is increasingly dissipated by breaking.

We investigated the low-tide increase in infragravity energy using higher-order spectral (bispectral) analysis. Bispectral analysis has been successfully employed to study nonlinear transfer of energy between frequencies in both the surf (*Elgar and Guza*, 1985; *Sénéchal et al.*, 2002) and the swash zone (*Bryan and Coco*, 2010). The technique examines the phase locking between the oscillations at triplets (f_1, f_2, f_3), where f_1 and f_2 are two basic frequencies and $f_3=f_1+f_2$. If the modes are independent of each other, as is the case of a field of waves with random phases, no significant bicoherence between them is expected to be observed in the bispectrum. However, considering that swash cycles are somewhat parabolic, and the parabolic shape is composed of the sum of phase-coupled harmonics with frequencies *f*, 2*f*, 3*f* and so on, and zero phase, the bispectral signature of the swash might be expected to show significant bicoherence at (*f*, *f*), (*f*, 2*f*), (2*f*, *f*) and so forth (e.g. *Bryan and Coco*, 2010, Figure 2).

Figure 2.13 summarizes the bispectral results, averaged for time series obtained at low, mid and high tide. The peaks between the incident frequency (around 0.08 Hz) and the harmonics can be observed as expected, although they are not strong and look smeared into a line. This is consistent with the results of *Sénéchal et al.* (2002) who found wave breaking to weaken the strength of the nonlinear couplings. There are also significant peaks in the bicoherence located at frequencies higher and lower than the incident peak. The higher peak was close to (0.12, 0.12 Hz), which roughly corresponds to the mean swash period (calculated in the time-domain as the duration of the time series divided by the number of local maxima and found to vary from 8.5 and 9.5 s). It is possible that these peaks are associated with swash interactions. *Bryan and Coco* (2010) showed bispectra generated from synthetic swash series in which each swash cycle was made dependant on the previous one. This interaction created an infragravity pattern in the time series caused by sequences of swash cycles (e.g. high-low-high-low crests). Because the incident wave ordering pattern was associated with the infragravity pattern, they were phase-locked. Since the infragravity pattern was not symmetric (the higher incident waves occurred either at the end or beginning of a sequence), the infragravity signal had evidence of harmonics in the bispectrum corresponding to a saw-tooth shape. In our case, the infragravity signal would appear to be at 0.06 Hz (with biphases between -30 and -50 degrees, indicating an asymmetric shape), and the harmonic at 0.12 Hz (with biphase shifting from -30 to -60 degrees as the tide decreases). Note that there is a coherent low tide signature in the bispectra at *f*1=0.06 Hz, *f*2=0.08 Hz. The 0.12 Hz coherence peaks also seem to be associated with the presence of the secondary

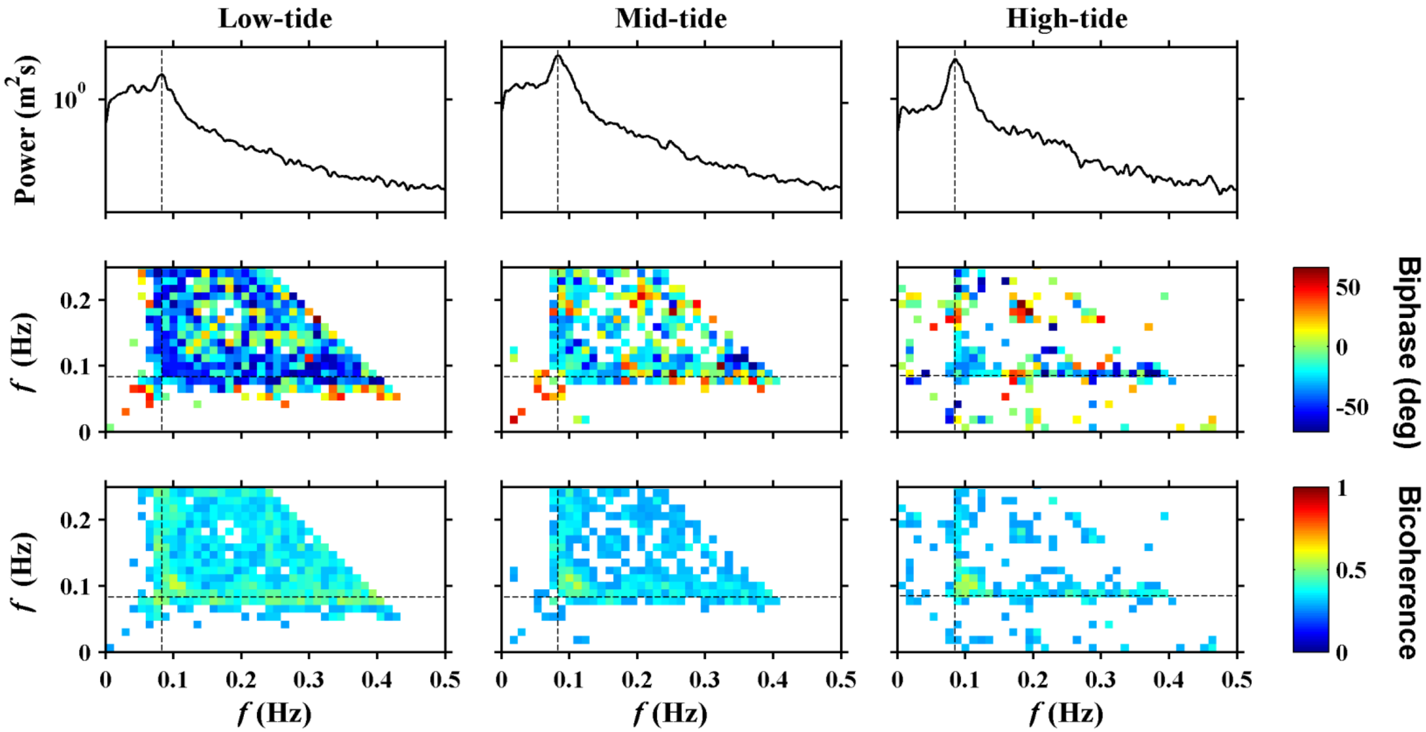

Figure 2.13. Runup spectra (top), biphases (mid) and bicoherences (bottom panels) averaged for time series obtained over low tide (runs 1, 10–12, 21–22, left), mid tide (runs 2–4, 8–9, 13–15, 18–20, 23–25, centre) and high tide (runs 5–7, 16–17, right panels). Black dashed lines highlight the peak frequency of the runup spectra shown on the top. Bispectra were calculated from each runup elevation time series after quadratic detrending, segmenting into sections of 512 s (1024 datapoints) and Fourier transforming, and the results were merged over 12 frequency bins, giving 84 degrees of freedom. Biphase and bicoherence signals below the 95% significance level have been blanked.

waves at the shoreline, so it is possible that the coupling process transfers energy to a ‘real’ wave. Alternatively the secondary waves might be related to shoaling and breaking processes in the surfzone. Observations of current and pressure just seaward of the swash would allow the swash-interaction hypothesis to be tested more thoroughly.

2.4.2 Swash elevation

The absence of significant changes in offshore wave conditions during the field experiment (Figures 2.5a–c, 2.9a, and 2.10) allowed us to control for effects of offshore wave height on runup and closely investigate the effects of other variables, such as beach slope and tide. Significant runup height Rs was found to be as high as $2.7Hs$ under non-breaking conditions, with the ratio Rs/Hs linearly decreasing to 1.5 at low tide when wave breaking was maximum. The incident band of the swash Rs_{Inc}, which accounted for most of the swash amplitude, ranged from ~1.2 to $2.6Hs$ between low and high tide (Figure 2.14a). Although Rs_{Inc}/Hs was not observed to scale with Iribarren number ξ_0 (Figure 2.14b), in disagreement with other observations (*Holman and Sallenger*, 1985; *Raubenheimer and Guza*, 1996), our results are consistent with the relationships obtained in these studies when breaking conditions were predominant. We found ξ_0 to range from 1.45 at low tide (Rs_{Inc}/Hs~1.2) to 2.16 at mid tide (Rs_{Inc}/Hs~2.0), when the swash was oscillating along the steepest section of the profile just under the step (see Figure 2.5e), which is within the range observed by these authors for equivalent Iribarren numbers (see *Holman and Sallenger*, 1985, Figures 7 and 10; *Raubenheimer and Guza*, 1996, Figure 5). Non-breaking conditions, on the other hand, resulted in the magnitude of normalized incident (and total) significant runup height to be consistently higher compared to these predictions (Figures 2.6b and 2.14b), suggesting that under mild offshore wave conditions the presence of a sandbar affects the magnitude of the swash. Our results differ substantially from observations under more dissipative conditions, where the incident band is saturated and most of the swash energy is at infragravity frequencies (e.g. *Guza and Thornton*, 1982, *Rs*/*Hs*~0.7; *Ruessink et al.*, 1998, *Rs*/*Hs*~0.18; *Ruggiero et al.*, 2004, *Rs*/*Hs*~0.26 to 0.61).

The tidal modulations have been observed to be manifested not only in the amplitude of swash oscillations, but also in the skewness of swash maxima distribution. The strong negative skewness, characteristic of high-tide time series (Figures 2.7 and 2.8) was shown to be related to the presence of the beach step at the elevation of about 2.3 m (Figures 2.3, 2.5f and 2.7). At high tide, this abrupt decrease in beach slope seems to limit vertical swash excursions farther above that height by both increasing bottom friction (the swash runs over a longer distance to reach a given elevation) and water percolation (the sand is likely to be unsaturated at this location). Without the beach step, one would have expected that even higher variance levels could have been observed at high tide, when most waves were not breaking over the sandbar. The slightly positive skewness in the swash maxima distribution at low tide, on the other hand, suggests a higher proportion of small negative maxima (smaller than the setup level). Indeed, *Holland and Holman* (1993) observed an increase in the proportion of negative ζ as the spectral width of the time series increased, which agrees with the noticeable spectral broadening observed during low tide in this dataset (see Figure 2.9b). The enhanced number of small swash maxima during low tide is also consistent with the observations of the secondary waves at the shoreline evident in Figure 2.12 and also supported by the reduction of about 10% in the average swash period (not shown).

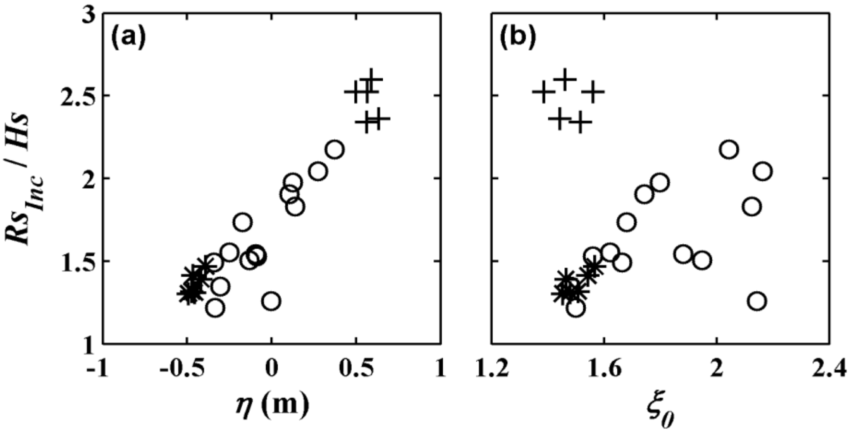

Figure 2.14. Regression plots of significant runup height for the incident frequency band (> 0.05 Hz) normalized by offshore significant wave height, as a function of: (a) tidal level, (b) Iribarren number. Asterisks, circles and crosses represent statistics from time series obtained during low tide (runs 1, 10–12, 21–22), mid tide (runs 2–4, 8–9, 13–15, 18–20, 23–25) and high tide (runs 5–7, 16–17), respectively.

2.5 Conclusion

Swash oscillations were observed to be strongly modulated by tide on an intermediate barred beach under mild wave conditions. The water depth over the offshore sandbar crest played a major role in controlling these modulations as it determined whether small waves broke over it or not according to the level of tide (i.e. water depth and therefore wave steepness over the crest). The concave profile may also have contributed to these tidal variations. These effects led to a tidal-modulation in wave energy dissipation that ultimately controlled the energy driving the swash and hence its amplitude (even without significant changes in offshore wave conditions). The dissipation took essentially at incident frequencies and also resulted in the slope of the saturated region of the spectra becoming gentler.

Swash hydrodynamics were found to be dominated by incident wave frequencies (consistent with the reflective slope) although this dominance became weaker during low tide as incident energy was increasingly dissipated by breaking over the bar. On the other hand, infragravity wave motions at the shoreline became more and more important as the tide decreased. We have provided evidence that secondary waves occur especially at low tide, and that the presence of these secondary waves might be related to an increase in the energy at infragravity frequencies through a mechanism of bore-bore capture.

Significant runup height was found to increase by a factor of two at high tide compared to low tide, when most waves were breaking over the sandbar, and these changes were not observed to be modulated either by beach slope or by offshore wave conditions. This suggests that tidal-induced wave breaking dissipation might be a major process in controlling swash hydrodynamics on barred intermediate beaches under mild offshore wave conditions and can have significant implications for both parameterizations and modeling of runup oscillations on these systems.

Chapter 3

Observations of alongshore variability of swash motions on an intermediate beach

R. M. C. Guedes, K. R. Bryan, G. Coco (2012), Observations of alongshore variability of swash motions on an intermediate beach, *Continental Shelf Research*, 48, 61-74, doi:10.1016/j.csr.2012.08.022.

Contribution of authors

Chapter 3 presents the article entitled "Observations of alongshore variability of swash motions on an intermediate beach", published in September 2012 in the *Continental Shelf Research*. The major contribution from this article is to show that alongshore variability in sandbar morphology may result in alongshore variability in swash oscillations.

My co-authors planned and executed the experiment before my PhD started. I extracted all the runup observations from the video, developed code for the statistical techniques, analysed all the data, prepared the figures and wrote the first and subsequent drafts of the paper. My co-authors edited drafts, provided advice on direction and helped with the response to the reviewer's comments.

Abstract

Alongshore variability in swash motions — shoreline oscillations about the mean water level on the beach face — were investigated using video images and a high-resolution morphology survey on an intermediate beach. Under mild, swell-dominated offshore wave conditions, alongshore variation of up to 78% in significant runup height *Rs* (defined as 4 times the standard deviation of the swash time series) was observed. This variation was predominantly driven by energy at the incident (>0.05 Hz) frequencies (where most of the swash energy was observed), and, consistent with previous observations, was mainly controlled by changes in the slope of the beach face (measured at the mean swash location). However, alongshore patterning in wave breaking over the sandbar caused variation in the degree of wave dissipation along the beach and also resulted in alongshore changes to swash motions. Although alongshore changes in beach slope and wave breaking patterning over the bar were observed to be typically correlated, both were needed in a regression model to provide the best explaination of alongshore changes in *Rs*. At infragravity frequencies (<0.05 Hz), alongshore variability was not well associated either with changes in beach slope or wave breaking patterning. Low-mode edge waves were observed in the swash measurements and their contribution to the total energy spectrum was greatest near the location where a shoal was observed, suggesting this shoal may play a role in forcing. The edge waves may have contributed to the swash variability observed at infragravity frequencies. However, in these reflective conditions, the infragravity band plays a secondary role in controlling alongshore variations to swash motions.

Keywords: swash, beach slope, wave breaking, alongshore variability, edge waves.

3.1 Introduction

Swash is the oscillation of the water's edge on the beach and is a key component of sediment exchanges between the ocean and the beach face (*Masselink and Hughes*, 1998; *Puleo et al.*, 2000). Swash flow changes both in time (as a result of changes in the wave climate and/or tidal levels) and space (as a result of changes in the cross-shore and alongshore beach profile). Aside from some notable investigations (e.g., *Holland and Holman*, 1996; *Ruggiero et al.*, 2004; *Ciriano et al.*, 2005; *Stockdon et al.*, 2006) most studies of swash hydrodynamics have focused on the relationship between wave climate and runup height but lacked a detailed assessment of the variability that can occur in the alongshore direction. Interest in alongshore variability in swash characteristics is both scientific, since it might be associated with infragravity wave signatures at the shoreline (e.g., *Holman and Bowen*, 1984; *Ciriano et al.*, 2005) and practical, since alongshore variability in runup could be used in coastal zone management of localized hazards (e.g., hot-spots or localized berm breaching and subsequent inundation).

The characteristics of the swash motions such as amplitude and spectral features have been studied in numerous laboratory (e.g., *Miche*, 1951; *Mase*, 1988; 1989; 1995; *Foote and Horn*, 2002; *Cowen et al.*, 2003) and field studies (e.g., *Huntley et al.*, 1977; *Guza and Thornton*, 1982; *Holman and Sallenger*, 1985; *Holman*, 1986; *Raubenheimer and Guza*, 1996; *Ruessink et al.*, 1998; *Stockdon et al.*, 2006; *Guedes et al.*, 2011; among many others). Yet, there is still considerable debate on how environmental parameters control the characteristics of these oscillations. *Miche* (1951) found that runup height R increases with (monochromatic) offshore wave height H_0 until a certain saturation limit that depends on beach slope β and wave frequency f. *Guza and Thornton* (1982) observed saturation of the vertical swash motions at sea-swell (incident) frequencies, although for the low-frequency (typically between 0.004 and 0.05 Hz) infragravity motions, a linear dependency on H_0 was observed. *Holman and Sallenger* (1985) observed a similar behavior under dissipative conditions, characterized by small values (0.4–1) of the Iribarren number ξ_0

$$\xi_0 = \frac{\beta}{\left(H_0/L_0\right)^{1/2}}, \tag{3.1}$$

where H_0 and L_0 are deep water wave height and wavelength. For higher ξ_0 no clear saturation of the incident swash was observed. They also found an overall good agreement between R, normalized by H_0, and ξ_0, which was further supported by subsequent research (e.g., *Holman*, 1986; *Raubenheimer and Guza*, 1996). *Stockdon et al.* (2006) observed the incident band of runup to be well parameterized by some modified (dimensional) version of ξ_0, although the infragravity band showed typically no significant relationship with β and scaled better with a parameter that was dependent on H_0 and L_0 solely. Conversely, *Guedes et al.* (2011) observed changes in R by up to a factor of 2 on a steep barred beach that were attributed mainly to changes in the degree of wave breaking over the bar, and, to a lesser degree, to changes in the local beach slope. Under highly dissipative conditions (ξ_0<0.3), contrasting behaviours have also been observed. For instance, *Ruessink et al.* (1998) found the runup height (which was dominated by infragravity frequencies) to be well parameterized by H_0 although a strong dependence of R on β was observed by *Ruggiero et al.* (2004). *Ruessink et al.* (1998), and more recently *Sénéchal et al.* (2011), suggested that saturation at infragravity swash frequencies can also occur during extreme storms.

Temporal variations in swash are often dominated by changes to the relative importance of infragravity and incident wave motions. Low-frequency, infragravity motions usually dominate the variance in the inner and swash zones under dissipative conditions (e.g. *Ruessink et al.*, 1998; *Ruggiero et al.*, 2004; *Sénéchal et al.*, 2011) and can be forced by nonlinear interactions between two wave trains w_1 and w_2 with similar frequencies. The linear superposition between these waves is manifested as intermittent groups of large and small waves at the difference frequency f_1-f_2 and wavenumber k_1-k_2. *Longuet-Higgins and Stewart*

(1962; 1964) showed that the gradients in radiation stress within these groups force a second-order, phase-locked (bound) wave which is 180° out of phase with the wave group. As the short waves break in the surf zone, the bound wave may be released and reflected at the shoreline as a free long wave, radiating offshore (leaky waves) or trapped in the nearshore by refraction and reflection (edge waves). Free long waves are also forced by temporal and spatial variations in the breakpoint position (*Symonds et al.*, 1982; *Lippmann et al.*, 1997).

Alongshore changes in swash amplitude have been shown to be strongly dependent on changes in foreshore beach slope β. *Holman and Sallenger* (1985) reported only small alongshore changes in runup height R on a natural beach which were positively correlated with the Iribarren number ξ_0 (and therefore beach slope since all alongshore observations were subjected to the same offshore wave conditions). *Ruggiero et al.* (2004), in contrast, observed alongshore changes in R of up to a factor of 2 in one single data run, with bigger swash motions over the alongshore regions where the foreshore was steeper. *Stockdon et al.* (2006) also found positive correlation between alongshore measurements of R (total and incident) and β and reported R to have the most alongshore variability when the beach topography was highly non-uniform due the presence of cusps, megacusps or welded swash bars. On the other hand, a negative correlation between alongshore series of infragravity swash height and β was observed when the cusp field was well developed. Many authors have shown the effect of cusp morphology on swash characteristics (e.g., *Holland and Holman*, 1996; *Ciriano et al.*, 2005; *Bryan and Coco*, 2010).

In essence, alongshore variations in swash have largely been attributed to beach face slope variations (*Holman and Sallenger*, 1985; *Ruggiero et al.*, 2004; *Stockdon et al.*, 2006) or, at a smaller spatial scale, to the influence of cusps (*Ciriano et al.*, 2005; *Stockdon et al.*, 2006; *Holland and Holman*, 1996; *Bryan and Coco*, 2010). However, *Guedes et al.* (2011) indicated (using measurements of swash at one location with almost constant offshore wave conditions) that tidal modulations to wave breaking over the bar also control changes in swash motions. Tidal changes can also cause large differences to alongshore breaking patterns, particularly in cases when the alongshore bar is irregular. These breaking patterns not only cause irregular dissipation of incident energy which will likely cause alongshore patterning of incident swash, but also patterning in the incident group structure. As a consequence, alongshore variations in the swash at infragravity ranges might be expected, quite separate from any effect beach cusps might have. Moreover, it is not clear to what degree edge waves are sensitive to such local variations in forcing conditions as they propagate alongshore. The objective of this work is to determine the importance of alongshore variability in wave breaking relative to beach slope patterns in controlling incident and infragravity swash motions on an intermediate beach with relatively alongshore uniform beach morphology. Section 3.2 describes the field data and the data analysis. The results are shown in Section 3.3 where the alongshore variability of swash is presented and compared to that of the beach slope and wave breaking patterns using regression analysis. In Section 3.4 the results are interpreted for the incident and infragravity bands of the swash and the importance of the environmental parameters are discussed. The conclusions are presented in Section 3.5.

3.2 Methods

3.2.1 Field site

The dataset used for this study was obtained from video and in situ measurements collected at Tairua Beach, New Zealand (Figure 3.1) during a field experiment undertaken on 15–17 July 2008. Tairua is a fairly steep ($\tan\beta \sim 0.1$) pocket beach, about 1.2 km in length, composed of medium–coarse sand. The beach faces NE towards the Pacific Ocean and is exposed to medium wave energy with average offshore significant wave height and mean spectral period of 0.9 m and 5.8 s (*Gorman et al.*, 2003). The tides are semi-diurnal and typically range between 1.2

(neap) and 2 m (spring tides). The beach is classified as intermediate in the model proposed by *Wright and Short* (1984) and characterized by a rhythmic sandbar and the common presence of strong rip currents (*Gallop et al.*, 2009; 2011). The sandbar remained remarkably alongshore-uniform during the 3 days, at a cross-shore distance of about 60 m from the shoreline (Figure 3.2) and with alongshore-averaged water depths over the crest ranging from 1.1 to 2.2 m due to tidal variations (see *Guedes et al.*, 2011). However, a broader shoal was observed closer to the southern end of the beach (-150 m $< y <$ -100 m, where y represents the alongshore coordinate of the grid defined for this study) where the sandbar trough was filled with sand and up to 0.7 m shallower compared to the trough depth at other alongshore locations (Figure 3.2).

3.2.2 Measurements

During the experiment, field measurements of offshore wave climate, beach face topography, and video images of the beach were obtained (*Guedes et al.*, 2011). Here, we analyze in detail three 60-min long periods from 16 July 2008, during low tide (11.00am–12.00pm), mid tide (08.00–09.00am) and high tide between 16.00–17.00pm (times are given in New Zealand Standard Time NZST).

Waves were measured using an Acoustic Doppler Current Profiler (ADCP) deployed in about 12 m water depth (~800 m from the coast). Time series of subsurface pressure were recorded every hour for 20 min, at 2 Hz and converted to offshore free surface elevation η_0 using linear wave theory. Offshore significant wave height Hs was calculated as 4σ (where σ is the standard deviation) of the free surface time series. Peak period Tp was determined as the inverse of the spectral peak frequency. Hourly mean water level η was calculated as the mean of each time series and adjusted to the local vertical datum. Peak direction Dp was determined from the directional velocity spectrum obtained by the ADCP.

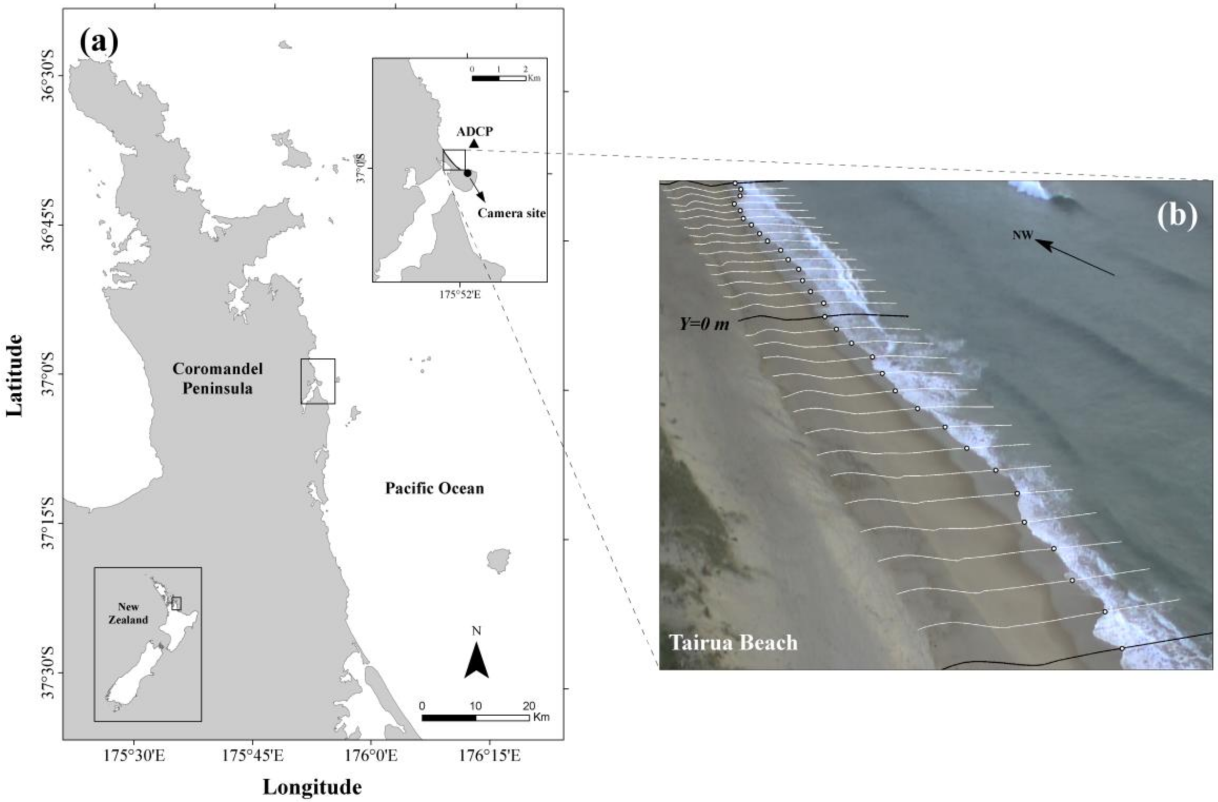

Figure 3.1. (a) Field site location. (b) Oblique image obtained at Tairua Beach on 16 July 2008 at 08.01am (New Zealand Standard Time), at mid tide. Lines represent the alongshore locations where the swash was measured with black lines highlighting the alongshore limits and the central position of the array. Lines are parallel in real world coordinates with 10-m alongshore spacing. White circles show the pixel locations where the swash was identified for this image.

Beach topography was surveyed on 16 July with a land-based lidar laser scan (see Figure 3.2). Within the surveyed region, an area extending over 300 m alongshore was selected for detailed study, encompassing the higher-resolution part of the field of view of the video camera. The hugely-dense "point-cloud" obtained from the beach scan was filtered using algorithms created to remove outliers and non-desired points (e.g., people standing on the beach). The algorithms repeatedly eliminated points below/above some standard deviation-based threshold within a moving window. The window-size [dx, dy] (where x and y represent the cross-shore and alongshore directions, respectively) was [0.5, 2.0] m which was small along x to limit the effect of the changes in elevation related to beach slope, and large along y to allow the detection of the outliers. The remaining points were then rotated and interpolated to a regular spacing of 0.5 m in the cross-shore and 1.0 m in the alongshore direction (the grid has its origin located at the alongshore position of the black line close to the center of Figure 3.1b and increases towards the NW direction). Finally, the grid was extrapolated offshore of the most seaward surveyed location at each alongshore position (this was necessary since at low tide the swash extended beyond the area covered by the survey). The extrapolation was performed by extending the linear fit through the lowermost measured points at each alongshore position.

High-resolution images with number of pixels [nu, nv] = [1528, 2016] (where u are the pixels along the vertical and v along the horizontal direction) were acquired continuously at 2 Hz, using a digital camera mounted at the southern end of the beach at approximately 42 m above the mean sea level (Figure 3.1b shows an example image). Swash oscillations were extracted at 31 alongshore locations, spaced 10 m apart (Figure 3.1b), which were parallel and oriented perpendicular to the beach in real-world coordinates. Pixel values were sampled along each of these lines, creating time series of pixel intensity (time stacks) from which the swash was identified (following *Aagaard and Holm*, 1989; *Guedes et al.*, 2011). For the mid-tide dataset of images only, the swash positions were also extracted at

1 m alongshore resolution, which is close to the maximum pixel resolution of the camera along the *y* direction near the northern end of the array (the image frames were used instead of extracting the time stacks). Conversions between pixel and ground coordinates were made using the colinearity equations described by *Holland et al.* (1997) with corrections for lens distortions (Figures 3.3a–c show examples of rectified images that have been averaged over 10 min of video footage). The vertical resolution of this technique, estimated by mapping the cross-shore pixel resolution to an elevation within the swash zone, varied as a function of both beach slope and distance from the camera and was less than 9 cm (with averages over each transect ranging from 1 to 2 cm from the closest to the farthest one).

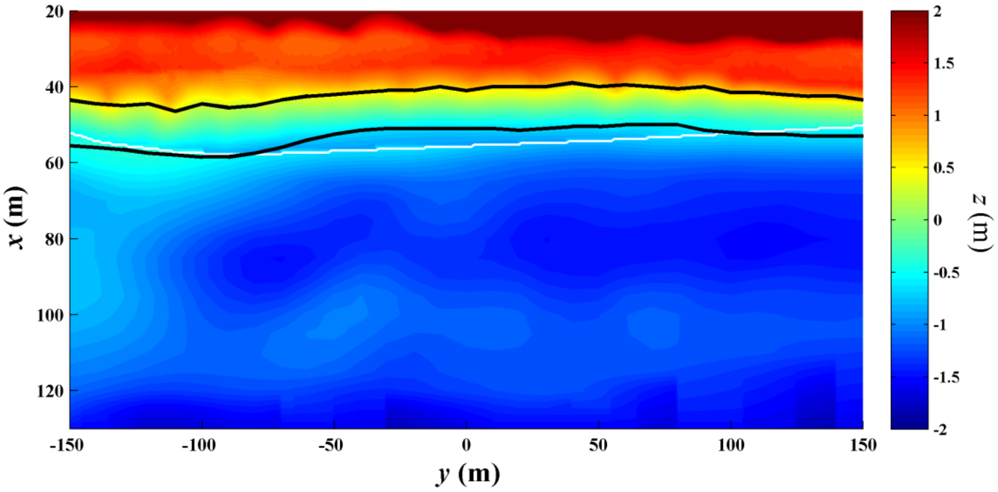

Figure 3.2. Nearshore bottom elevation map derived from the Lidar survey undertaken on 16 July 2008 and the bathymetry estimated from the images from the same day using the method described in Section 3.2.3. Color bar represents elevation *z* relative to the mean sea level at low tide. Black thick lines show mean swash locations calculated from the time stacks at low and high tide. White line delimits the elevations interpolated from the Lidar survey from those obtained using the images. *x* and *y* are the cross-shore and alongshore grid coordinates, respectively.

3.2.3 Data analysis

The swash was defined at each alongshore location as the most shoreward edge of water identifiable on the images. This definition has been shown to be consistent with swash measurements obtained using resistance wires deployed near the seabed (*Holman and Guza*, 1984; *Holland et al.*, 1995). The edge was detected using an image processing algorithm developed to distinguish the sharp contrast typically observed between the foamy swash front and the darker sandy beach. Manual swash detections were required in some images where the algorithm failed due to poor lighting contrasts. Time series of vertical runup elevation R were derived from the digitized swash locations since the beach topography was accurately known from the lidar survey. In total, 3×31, 60-min long time series of runup elevation were generated over the three periods of interest. Additionally, a matrix composed of 301, 60-min long runup series (spaced every 1 m alongshore) was also generated at mid tide.

The beach slope β within the swash area was calculated from the surveyed beach face morphology using two different approaches to account for the possible effect of a beach step present between the cross-shore positions of ~25 and 40 m (see Figure 3.2). *Guedes et al.* (2011) found that the presence of the beach step affected the swash maxima distribution at high tide. The first approach ($\beta_{2\sigma}$) defined β at each i^{th} alongshore position $y_i(t)$, where t is time, as the best linear fit of the measured cross-shore profile $h(x)$ between the locations of mean ± 2σ of the shoreline positions for each data run. The beach step was included in the calculation of $\beta_{2\sigma}$ at high tide. The second approach (β_{mean}) did not include the beach step and β was defined as the best linear fit of $h(x)$ between the location of mean shoreline position ± 10 cm for each data run.

Nearshore bathymetry was estimated offshore of the region where the swash was measured using the method developed by *Plant et al.* (2008). The technique uses time series of image intensity sampled from georeferenced pixels and identifies wavenumbers k where the coherence of intensity between pairs of pixels is maximized. The method is based on a tomographic approach that uses a nonlinear inverse method to solve for wavenumbers at discrete sets of frequencies and provides accuracy estimates that reflect the sampling design, the signal coherence and the resolution of the solution (*Plant et al.*, 2008). The bathymetry is inverted from the estimated wavenumbers using the linear dispersion relationship:

$$(2\pi f)^2 = gk\tanh(kh), \tag{3.2}$$

where g is the acceleration due to gravity and h is the local water depth. The values of h that minimize the error between k predicted by Equation (3.2) and that estimated from the images are found using an iterative scheme. The method was used to estimate the nearshore bathymetry on 2048-second long pixel time series, extending from 50 m < x < 150 m and -150 < y < 150 m and spaced every 2 and 5 m along x and y, respectively. A coarser domain with spacing [dx, dy] = [5, 10] m was defined for estimating k and h, for computational reasons. The accuracy estimated using the technique of *Plant et al*. (2008) was typically less than 0.1 m for the area extending from the trough to the crest of the sandbar (although errors greater than 1 m were obtained close to the shoreline and offshore of the crest).

The contribution of breaking waves was estimated for the three periods of interest as the probability of breaking $P_{br}(x,y,t)$ using the method described by *Guedes et al.* (2011) (Figures 3.3d–f). The technique is based on the identification of breaking-generated foam on the time stacks, through the definition of pixel intensity thresholds, and the calculation of the probability for this foam to be observed in each pixel. Although this method does not distinguish the foam directly associated with the breaking wave roller from residual foam left on the sea surface after the waves break, one can expect the latter to be more frequent as wave breaking increases.

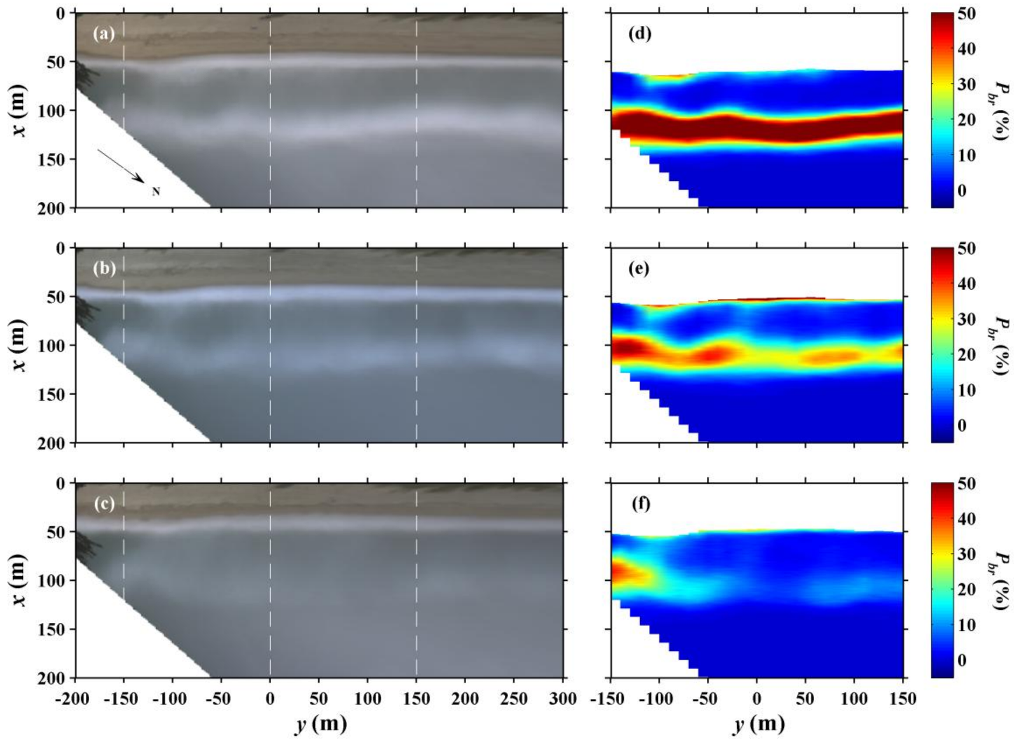

Figure 3.3. Averaged images obtained on 16 July 2008, at (a) low tide (11:30am), (b) mid tide (08.30am), and (c) high tide (16.30am), rectified to plan views using geometric transformations (see Section 3.2.2). White dashed lines represent alongshore locations of southernmost, central and northernmost time stacks. Images were averaged over 10-min periods. Spatial distribution of the probability of breaking, calculated at (d) low tide (11.00am–12.00pm), (e) mid tide (08.00–09.00am), and (f) high tide (16:00–17:00pm) with the method described in Section 3.2.3 *x* and *y* are the cross-shore and alongshore grid coordinates, respectively. Color bar represents the probability of breaking.

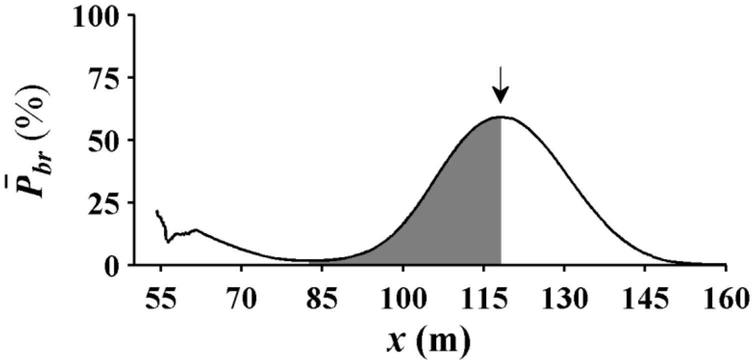

Figure 3.4. Alongshore-averaged probability of breaking $\overline{P}_{br}(x)$ at low tide. Vertical arrow highlights the maximum probability from where Max(P_{br}) is quantified. Gray shading shows the area over which $\int P_{br} \mathrm{d}x$ is quantified.

Alongshore series of $P_{br}(y,t)$ were calculated in two ways, exemplified in Figure 3.4. The first consisted of calculating the area under the curves between the cross-shore locations of minimum (shoreward of the crest) and maximum P_{br} ($\int P_{br}\mathrm{d}x$). The second approach quantified $P_{br}(y,t)$ as the maximum probability observed at any cross-shore pixel location, Max(P_{br}). Additionally, the cross-shore position of wave breaking $X_{br}(y,t)$ was determined as the location of maximum probability of breaking.

Swash statistics were calculated from the 93 (detrended) hourly time series of runup elevation R obtained from the time stacks. Significant run up height Rs was estimated as $4\sigma_R$. Power spectra were calculated from each time series, segmented into sections of 128 s and tapered with a Hanning window. The energy density was partitioned into high ($f > 0.05$ Hz) and low frequency bands ($f \leq 0.05$ Hz) and integrated to account for the variance in the incident σ^2_{Inc} and infragravity σ^2_{Ig} regions, respectively. Wavenumber-frequency spectra $E(k, f)$ were computed from groups of 16 adjacent time series (maximum separation lag of 150 m) using the iterative maximum likelihood estimator (IMLE) developed by *Pawka* (1983). The series were segmented and tapered as for the frequency spectrum calculations. A wavenumber resolution of 0.0005 m^{-1} was chosen for the analysis. In the case where measurements were collected at 1-m resolution, a 2-dimensional *Fourier* transform (not shown) confirmed that the patterns detected using the IMLE were not an artifact of the alongshore array design.

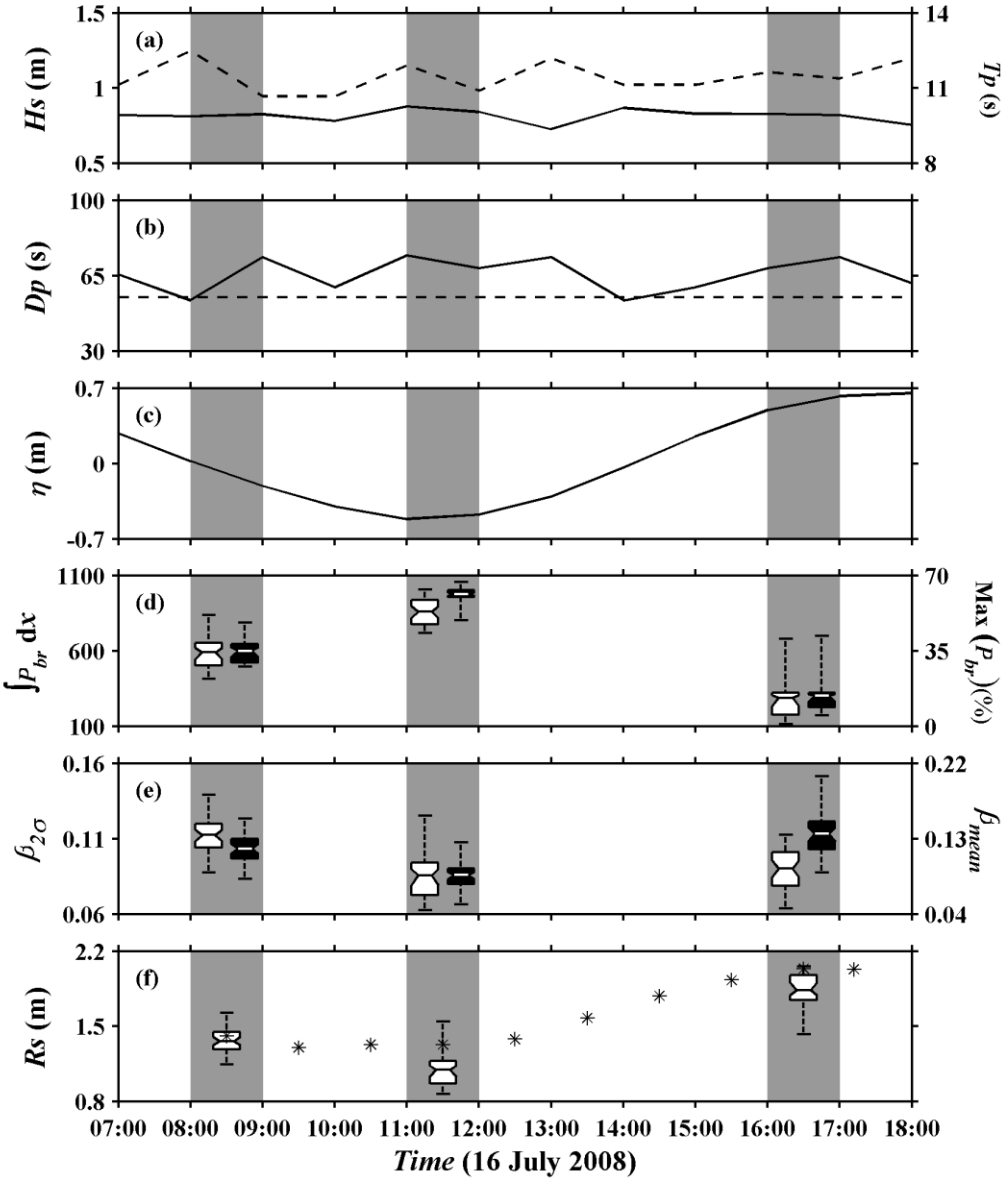

Figure 3.5. Time series of hydrodynamic and morphological parameters with gray shading highlighting the 3 periods analyzed. (a) Offshore significant wave height *Hs* (solid line, left axis) and peak wave period *Tp* (dashed line, right axis). (b) Offshore peak wave direction *Dp* with horizontal dashed line indicating shore-normal incidence direction. (c) Mean sea level η. (d) Degree of wave breaking quantified as $\int P_{br}\mathrm{d}x$ (left axis, white boxes) and Max(P_{br}) (right axis, black boxes). (e) Beach slope calculated as $\beta_{2\sigma}$ (left axis, white boxes) and β_{mean} (right axis, black boxes). (f) Significant runup height *Rs* with asterisks showing the data presented in *Guedes et al.* (2011). For each box in panels (d–f) the central mark is the alongshore average, the edges of the box are the 25th and 75th percentiles and the vertical dashed lines extend to the most extreme data points for all alongshore observations. The boxes in panels (d–e) were slightly displaced horizontally from their central position for better visualization.

3.3 Results

3.3.1 Observations

During the three periods selected for analysis, the offshore hydrodynamic conditions remained remarkably consistent. Gently-sloping waves were measured in 12 m water depth, with Hs and Tp around 0.8 m and 11.5 s (Figure 3.5a), approaching the coast from the northeast direction, typically less than 10° from shore-normal incidence (Figure 3.5b). The video recordings of swash motions spanned part of a tidal cycle ranging in elevation between -0.49 and 0.56 m (Figure 3.5c). The alongshore-averaged amount of wave breaking changed due to tidally-induced variations in the water depth over the sandbar crest, with strong wave breaking at low tide and weak during high tide (Figure 3.5d; see also Figure 3.3). The alongshore-averaged beach face slope β calculated using the two methods showed different patterns. The concave shape of the beach face resulted in β_{mean} following the same trend as the tide (Figure 3.5e, black boxes). However, $\beta_{2\sigma}$ was affected by the beach step just above the beach face (see Figure 3.2) with the values at high tide being on average 20% smaller compared to those obtained at mid tide (Figure 3.5e, white boxes). The significant runup height Rs increased by 70% on average between low and high tide and displayed a consistent relationship to both η and β_{mean} (Figure 3.5f).

Alongshore changes were also observed in the surf and swash zones (Figures 3.5d–f). Alongshore ranges in $\beta_{2\sigma}$ and β_{mean} were up to 0.6 and 0.12 (accounting respectively for an increase of 100% and 144% from the smallest to the highest values for these two variables). At low tide, when wave breaking was strong at all alongshore locations, $P_{br}(y)$ was relatively uniform (see also Figures 3.3a and 3.3d). At high tide, though, the alongshore variability was higher due to stronger wave breaking at the southern end of the beach, where the shoal was observed (see Figures 3.2, 3.3c and 3.3f). Alongshore changes in Rs were up to 0.68 and 0.63 m at low and high tide, representing an increase from the smallest to the

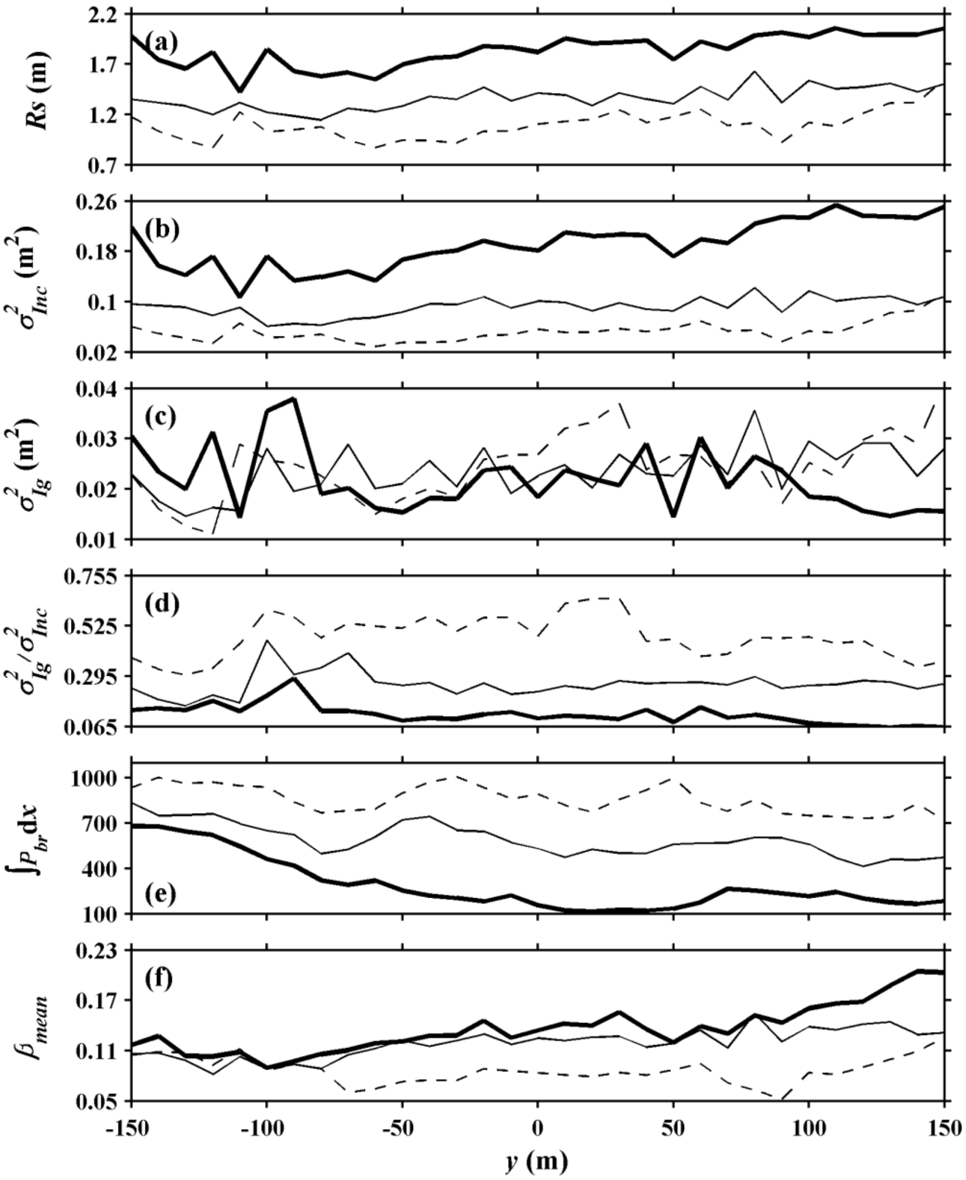

Figure 3.6. Alongshore series with dashed, thin and thick lines representing data obtained at low, mid and high tide: (a) significant runup height Rs. (b) Variance integrated over the incident σ2Inc (f>0.05 Hz) and (c) over the infragravity σ2Ig (f<0.05 Hz) regions of the spectrum. (d) Ratio between σ2Ig and σ2Inc. (e) Degree of wave breaking quantified as ∫Pbrdx. (f) Beach slope calculated as βmean.

highest values of 78% and 44%, respectively (substantially higher at low tide since *Rs* was smaller).

Figure 3.6 shows the alongshore series of the total and partitioned swash variance observed for the three periods analyzed, with the alongshore series of $\int P_{br}\mathrm{d}x$ and β_{mean} also shown. A linear alongshore trend exists during all periods for *Rs* with values normally higher towards the northern end of the beach (Figure 3.6a). Small scale alongshore variability in *Rs* and partitioned variances (Figure 3.6a-c) between y ~ [-130 m to -90 m] and y ~ [40 m to 100 m] may be associated with the incipient cusp field evident at these locations (see Figure 3.2).

The incident swash variance σ^2_{Inc} had similar spatial and temporal patterns to *Rs* (Figure 3.6b). At infragravity frequencies, conversely, there is no clear alongshore trend, yet some of the highest variances can be observed towards the southern end of the beach at high tide (Figure 3.6c). Additionally, σ^2_{Ig} was found to be typically larger at low tide compared to high tide, in contrast to σ^2_{Inc} and *Rs* (as also observed by *Guedes et al.*, 2011). The ratio between σ^2 at infragravity and incident frequencies showed a distinct behavior with $\sigma^2_{Ig}/\sigma^2_{Inc}$ consistently increasing from high to low tide (Figure 3.6d). The alongshore series of $\int P_{br}\mathrm{d}x$ and β_{mean} showed opposing trends with the former predominantly decreasing and the latter increasing from the southern to the northern side of the beach (Figures 3.6e and 3.6f).

In order to understand the competing role of the alongshore versus temporal variability in the environmental parameters the proportion of the total variance explained by its temporal P_t and spatial P_y components were defined as:

$$P_t = \frac{\overline{\left[\left\langle \chi(t,y)\right\rangle - \chi_m\right]^2}}{\left\langle \left[\chi(t,y) - \chi_m\right]^2 \right\rangle}, \tag{3.3}$$

$$P_y = \frac{\left\langle \left[\overline{\chi(t,y)} - \chi_m\right]^2 \right\rangle}{\left\langle \left[\chi(t,y) - \chi_m\right]^2 \right\rangle}, \tag{3.4}$$

where χ is a generic environmental parameter, overbar and angle bracket denote respectively temporal and spatial average and subscript m denotes average over the whole dataset. The results are reported in Table 3.1. The temporal contributions to the total variance P_t were greater than the alongshore contributions P_y for all environmental parameters except for the infragravity variance σ^2_{Ig}. P_t was a factor of 7 and 8 higher than P_y for Rs and σ^2_{Inc} respectively. For σ^2_{Ig}, on the other hand, P_y was an order of magnitude greater than P_t. The temporal contributions to the total variance were also higher than the alongshore contributions for the amount of wave breaking over the bar and the beach slope although the percentages explained by P_t were substantially greater for wave breaking (Table 3.1).

Table 3.1. Proportion of the total variance in the space-time series χ explained by their temporal P_t and spatial P_y contributions, calculated using Equations (3.3) and (3.4).

χ	P_t	P_y
$\beta_{2\sigma}$	0.42	0.21
β_{mean}	0.48	0.29
$\int P_{br}dx$	0.77	0.16
Max(P_{br})	0.88	0.05
Rs	0.83	0.12
σ^2_{Inc}	0.84	0.10
σ^2_{Ig}	0.03	0.37
$\sigma^2_{Ig}/\sigma^2_{Inc}$	0.82	0.09

Not only did the relative magnitude between the incident and infragravity swash bands change alongshore but also the shape of the spectra. Figure 3.7 shows the runup spectra calculated at mid tide at all the alongshore positions. Although prominent peaks at infragravity frequencies can be observed for some alongshore regions (e.g. $y < -110$ m, $y > 50$ m), others are characterized by a relatively white spectrum at infragravity frequencies (e.g. 0 m $< y <$ 50 m). The infragravity peaks are usually at or near either the first $f_p/2$ or second sub-harmonics $f_p/3$ (where f_p is the incident peak frequency). These patterns were similar at low and high tide, although at low tide the infragravity peaks were greater than the incident peaks at some locations and at high tide the former were typically an order of magnitude smaller than the latter (not shown).

3.3.2 Regression analysis

The influence of environmental conditions on the alongshore and temporal properties of the swash was investigated using regression analysis (the results of all linear regression are reported in Table 3.2). Figure 3.8a shows a scatter plot of significant runup height against beach slope β_{mean}. A significant linear correlation was observed at each of the 3 stages of the tide with correlation coefficients r^2 of 0.37, 0.81 and 0.52 at low, mid and high tide, respectively (all reported regressions were significant with p-value < 0.05). The weaker correlation was observed at low tide, where the extrapolation of the bathymetry may have affected the evaluation of the beach slope. The strongest dependence of runup height on β_{mean} occurred at mid tide, where the swash ran over the somewhat linear part of the beach face and where there was still wave breaking at all alongshore locations (Figures 3.3b and 3.3e). At high tide, where the alongshore variability in wave breaking was greatest and where part of the swash cycles extended over the beach step, the correlations were considerably smaller than at mid tide. Analysis of the relationship between $\beta_{2\sigma}$ and Rs showed the same patterns described above at low and mid tide (with slightly smaller correlation coefficients), although at high tide

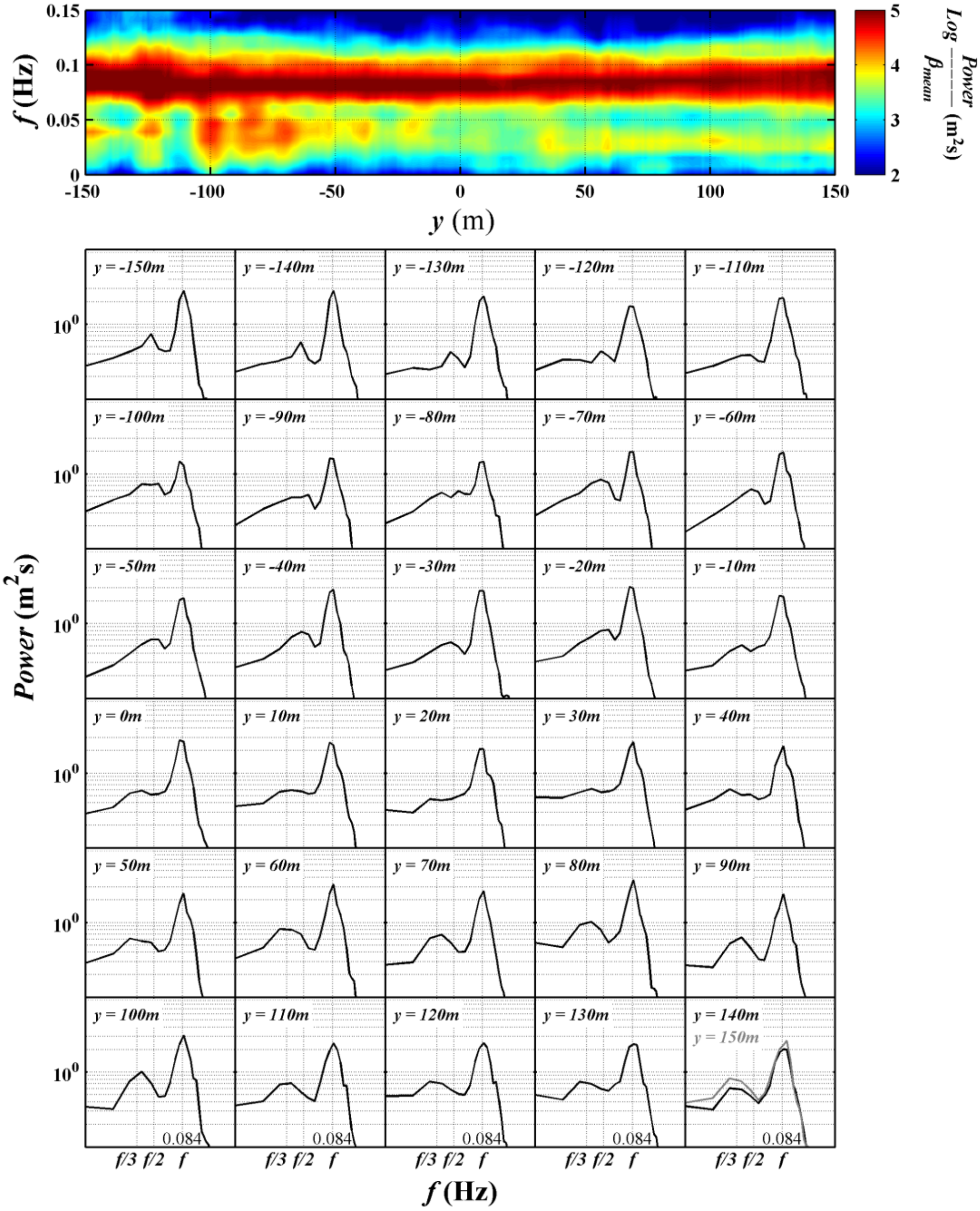

Figure 3.7. Top panel: alongshore series of runup spectra normalized by the beach slope βmean. Spectra were calculated from the mid-tide time series which were spaced at 1-m intervals. Color bar represents the logarithm of the normalized power. Bottom panels: Spectra obtained from the same period every 10-m alongshore (positions are indicated in the top left corner of each panel). Alongshore-averaged frequencies corresponding to the peak (f), first (f/2) and second sub-harmonic (f/3) are indicated.

$\beta_{2\sigma}$ decreased due to the beach step and no significant linear correlation was observed. When the whole dataset is analyzed, we notice that (1) the correlation between β_{mean} and Rs is significant (r^2=0.66, about 20% smaller than the value observed at mid tide); (2) the regression line intercept obtained at high tide is a factor of 2 higher than that obtained at low and mid tide which suggests other parameters control temporal changes in Rs, consistent with *Guedes et al.* (2011); and (3) there is a trend with wave breaking increasing towards the lowest values of Rs and β_{mean} (Figure 3.8a).

Figure 3.8b shows the correlations between Rs and $\int P_{br}\mathrm{d}x$. Significant linear correlation was observed at low and high tide although the linear dependence was weak (r^2=0.15 and 0.17, respectively). However, Rs showed a stronger nonlinear relationship to wave breaking at high tide with r^2 increasing to 0.41 when a quadratic regression model was used (Table 3.3). At mid tide, where the correlation between Rs and β_{mean} was greatest, no significant linear relationship between Rs and $\int P_{br}\mathrm{d}x$ was observed. The regression over the whole dataset showed a strong linear correlation between these two variables with r^2=0.75 (14% higher that the correlation coefficient between Rs and β_{mean} for the whole dataset). This suggests that although alongshore changes in Rs were better correlated with changes in beach slope (when the beach step is not included in the slope calculations), changes in wave breaking explain the Rs variability better when the temporal variability is also included.

The effects of combining changes in beach slope and wave breaking in the swash were evaluated using a multiple regression model. Table 3.3 synthesizes the results obtained using a quadratic model with different combinations of "independent" variables to represent beach slope (β_{mean}) and wave breaking over the bar (Max(P_{br}) and X_{br}). Using all the three independent variables in the model improved the model performance for all tides and also using the whole dataset (compare the adjusted correlation coefficients r^2_{adj} and the root mean square errors E_{rms}). However, the improvement was most evident at low tide, when r^2_{adj}

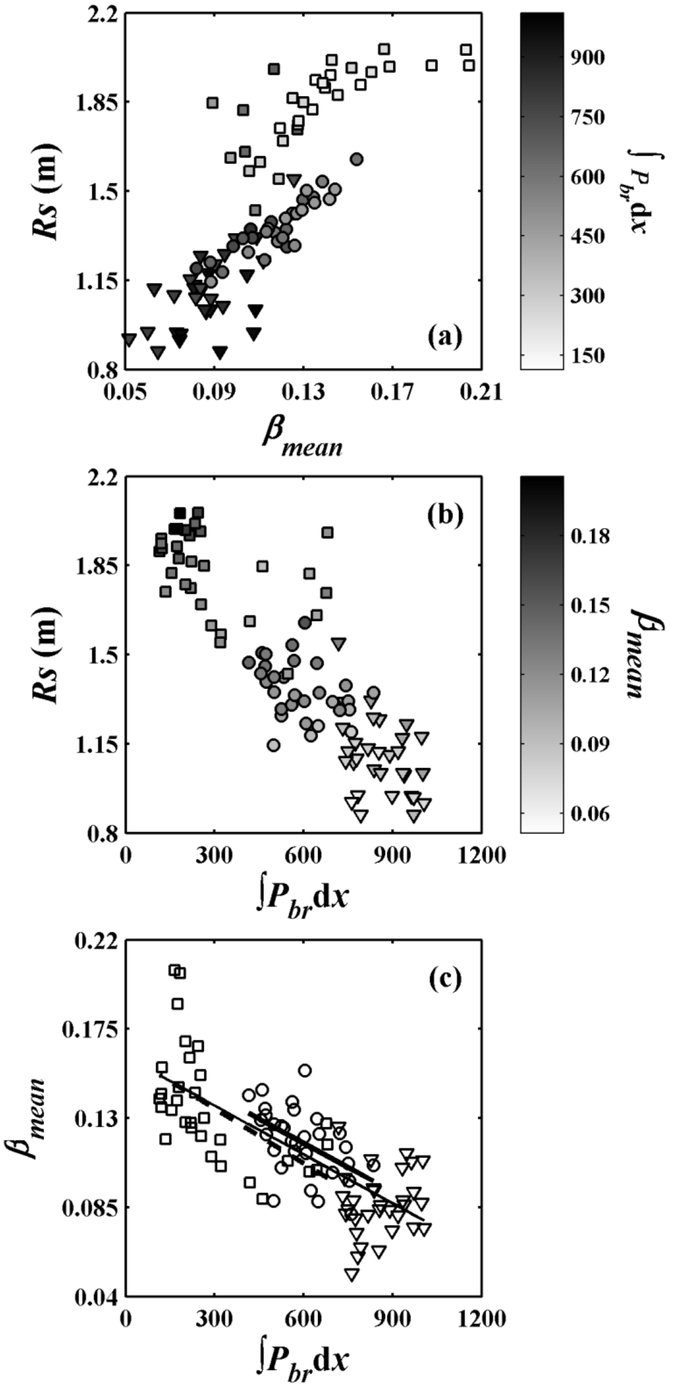

Figure 3.8. Scatter plots of environmental parameters with triangles, circles and squares representing data obtained at low, mid and high tide respectively: (a) significant runup height *Rs* as a function of beach slope quantified as β_{mean} with color bar representing the amount of wave breaking calculated as $\int P_{br}$dx. (b) *Rs* as a function of $\int P_{br}$dx with color bar representing β_{mean}. (c) β_{mean} as a function of $\int P_{br}$dx. Thick solid, dashed and thin solid lines are the best linear fit between β_{mean} and $\int P_{br}$dx for the data obtained at mid and high tide and over the whole dataset respectively (the three cases where significant linear relationship at the 95% confidence level was observed).

increased by 50% and 80% compared to the model using X_{br} and β_{mean} only, respectively. Although at high tide there was also a substantial improvement when using the three independent variables (r^2_{adj}=0.66, respectively 29% and 78% higher than using β_{mean} and Max(P_{br}) alone), at mid tide the enhancement was small (with r^2_{adj} barely 5% higher than that obtained with the model using β_{mean} only). Overall, best results were achieved with the quadratic model over a linear one, for the three stages of tide (up to 80% higher at low tide, not shown). This is because the two variables adopted as a proxy of wave breaking in the model showed a nonlinear relationship to *Rs* within each tide period, whereas the linear and quadratic models using β_{mean} alone had essentially the same skill.

Table 3.2. Regression analysis results.

	x	*y*	*m*	*b*	r^2
Low tide	β_{mean}	*Rs (m)*	*5.558358*	*0.6151*	***0.37***
	$\int P_{br}dx$	*Rs (m)*	*-0.000627*	*1.6332*	***0.15***
	β_{mean}	$\sigma^2_{Inc}(m^2)$	*0.716397*	*-0.0090*	***0.45***
	$\int P_{br}dx$	$\sigma^2_{Inc}(m^2)$	*-0.000069*	*0.1124*	***0.13***
	β_{mean}	$\sigma^2_{Ig}(m^2)$	*0.144143*	*0.0120*	*0.12*
	$\int P_{br}dx$	$\sigma^2_{Ig}(m^2)$	*-0.000031*	*0.0507*	***0.17***
Mid tide	β_{mean}	*Rs (m)*	*5.826599*	*0.6707*	***0.81***
	$\int P_{br}dx$	*Rs (m)*	*-0.000369*	*1.5772*	*0.13*
	β_{mean}	$\sigma^2_{Inc}(m^2)$	*0.724831*	*0.0063*	***0.71***
	$\int P_{br}dx$	$\sigma^2_{Inc}(m^2)$	*-0.000027*	*0.1080*	*0.04*
	β_{mean}	$\sigma^2_{Ig}(m^2)$	*0.183494*	*0.0019*	***0.43***
	$\int P_{br}dx$	$\sigma^2_{Ig}(m^2)$	*-0.000021*	*0.0356*	***0.21***
High tide	β_{mean}	*Rs (m)*	*4.061148*	*1.2842*	***0.52***
	$\int P_{br}dx$	*Rs (m)*	*-0.000390*	*1.9478*	***0.17***
	β_{mean}	$\sigma^2_{Inc}(m^2)$	*1.079916*	*0.0438*	***0.67***
	$\int P_{br}dx$	$\sigma^2_{Inc}(m^2)$	*-0.000106*	*0.2210*	***0.24***
	β_{mean}	$\sigma^2_{Ig}(m^2)$	*-0.099998*	*0.0353*	***0.21***
	$\int P_{br}dx$	$\sigma^2_{Ig}(m^2)$	*0.000012*	*0.0182*	*0.12*
All tides	β_{mean}	*Rs (m)*	*9.267611*	*0.3787*	***0.66***
	$\int P_{br}dx$	*Rs (m)*	*-0.001101*	*2.0673*	***0.75***
	β_{mean}	$\sigma^2_{Inc}(m^2)$	*1.732476*	*-0.0848*	***0.65***
	$\int P_{br}dx$	$\sigma^2_{Inc}(m^2)$	*-0.000206*	*0.2309*	***0.75***
	β_{mean}	$\sigma^2_{Ig}(m^2)$	*-0.020556*	*0.0256*	*0.01*
	$\int P_{br}dx$	$\sigma^2_{Ig}(m^2)$	*0.000003*	*0.0214*	*0.02*

$y=mx+b$. Correlation coefficient r^2 significant at the 95% confidence level showed in bold.

Table 3.3. Multiple regression results. Independent variables P_{br} and β were quantified as Max(P_{br}) and β_{mean}, respectively. r^2 is the correlation coefficient for each model. r^2_{adj} is the correlation coefficient adjusted for the number of observations n and unknown coefficients p as: $1-\left(1-r^2\right)\left[\left(n-1\right)/\left(n-p\right)\right]$. E_{rms} is the root mean square error, given in meters. Models with best skill (high r^2_{adj}, small E_{rms}) for each stage of tide are highlighted in bold.

Dependent variable	***Independent variables***	r^2	r^2_{adj}	E_{rms}	***n***
		Low tide			
Rs	P_{br}	*0.03*	*-0.04*	*0.15*	*31*
Rs	β	*0.39*	*0.35*	*0.12*	*31*
Rs	X_{br}	*0.46*	*0.42*	*0.11*	*31*
Rs	P_{br}, β	*0.64*	*0.57*	*0.09*	*31*
Rs	P_{br}, X_{br}	*0.57*	*0.49*	*0.10*	*31*
Rs	β, X_{br}	*0.57*	*0.48*	*0.10*	*31*
Rs	P_{br}, β, X_{br}	*0.74*	*0.63*	*0.08*	*31*
		Mid tide			
Rs	P_{br}	*0.14*	*0.08*	*0.11*	*31*
Rs	B	*0.83*	*0.82*	*0.05*	*31*
Rs	X_{br}	*0.12*	*0.06*	*0.11*	*31*
Rs	P_{br}, β	*0.84*	*0.81*	*0.05*	*31*
Rs	P_{br}, X_{br}	*0.26*	*0.11*	*0.10*	*31*
Rs	β, X_{br}	*0.88*	*0.85*	*0.04*	*31*
Rs	P_{br}, β, X_{br}	*0.90*	*0.86*	*0.04*	*31*
		High tide			
Rs	P_{br}	*0.41*	*0.37*	*0.13*	*31*
Rs	β	*0.54*	*0.51*	*0.11*	*31*
Rs	X_{br}	*0.06*	*0.00*	*0.16*	*31*
Rs	P_{br}, β	*0.65*	*0.59*	*0.10*	*31*
Rs	P_{br}, X_{br}	*0.42*	*0.31*	*0.13*	*31*
Rs	β, X_{br}	*0.62*	*0.54*	*0.10*	*31*
Rs	P_{br}, β, X_{br}	*0.76*	*0.66*	*0.08*	*31*
		All tides			
Rs	P_{br}	*0.78*	*0.78*	*0.16*	*93*
Rs	B	*0.66*	*0.66*	*0.20*	*93*
Rs	X_{br}	*0.48*	*0.47*	*0.25*	*93*
Rs	P_{br}, β	*0.84*	*0.83*	*0.14*	*93*
Rs	P_{br}, X_{br}	*0.87*	*0.86*	*0.12*	*93*
Rs	β, X_{br}	*0.76*	*0.75*	*0.17*	*93*
Rs	P_{br}, β, X_{br}	*0.93*	*0.92*	*0.09*	*93*

Quadratic models: $Y=b_0+b_1X_1+b_2X_2+b_3X_1X_2+b_4X_1^2+b_5X_2^2$, where Y is the predicted variable, X_q is the q^{th} independent variable, b_0 is the intercept and b_k, k=1,2,… are the regression coefficients.

Figure 3.8c shows the scatter plot between $\int P_{br}\mathrm{d}x$ and β_{mean}. There is a negative relationship between the amount of wave breaking and the beach slope over the complete dataset with changes in $\int P_{br}\mathrm{d}x$ explaining 55% of β_{mean} changes. When regressing the data from each stage of tide, a negative relationship occurred also at mid and high tide with r^2 amounting to 0.26 and 0.31, respectively. At low tide, when part of the beach face was not surveyed and when wave breaking was more homogeneous alongshore, no significant linear relationship was observed.

The scatter plot of the ratio between the variance at infragravity and incident frequencies σ_{Ig}/σ_{Inc} versus significant runup height Rs is shown in Figure 3.9. A negative linear relationship was observed at high tide, with changes in Rs explaining 26% of the observed changes in σ_{Ig}/σ_{Inc}. Although no significant linear relationship was observed between these variables at low and mid tide, a strong negative correlation was found using the whole dataset with r^2=0.67 which is consistent with the increase in the relative contribution of the infragravity frequencies as wave breaking increases and the incident wave energy is dissipated.

3.4 Discussion

3.4.1 Environmental control

The amount of wave breaking was observed to be negatively correlated with the foreshore beach slope when the beach step was not included (Figure 3.8c). This is not surprising given that the concave shape of the beach face means that its alongshore-averaged slope decreases substantially at low tide (Table 3.4) when the water depth over the sandbar is smaller and there is more wave breaking over it (Figures 3.3, 3.6e). Nevertheless, the significant linear correlation also observed using only the mid and high tide datasets indicates that there is indeed some degree of dependence between the local beach slope β_{mean} and the degree of wave breaking over the bar. This dependence suggests a morphological coupling between the sandbar and the shoreline (e.g. *Castelle et al.*, 2010) and is consistent with observations of rhythmic sandbar features coupled with shoreline rhythmicity (e.g. *Sonu*, 1973; *Coco et al.*, 2005; *Castelle et al.*, 2010).

Guedes et al. (2011) showed that changes in the degree of bar-induced wave breaking dissipation can be the dominant control on changes to swash motions. In that study the breaking patterns were essentially modulated by tidal-induced changes in the water depth over the sandbar crest. The limited alongshore variability in the sandbar morphology observed in this study would be expected to yield limited effect on alongshore runup variability. However, a relatively broad shoal was observed near the southern end of the beach which resulted in some degree of alongshore variability in wave breaking, most evident during high tide. At high tide the negative correlation between $P_{br}(y)$ and $Rs(y)$ was greatest (Table 3.3), suggesting that these small alongshore changes in bar morphology did reflect alongshore changes in swash height, although it does not appear to have been the dominant process controlling these changes. Our observations suggest that well-developed three-dimensional sandbar morphology might yield substantial alongshore runup variability. Generality of previous studies analyzing runup elevations at a single location might be limited and future studies should account for the effect of alongshore variability in both the beach face and the sandbar.

Consistent with *Ruggiero et al.* (2004), although in this case for a much steeper beach, alongshore runup variability was predominantly induced by alongshore changes in beach slope. Though alongshore variations in wave breaking also appear to have affected the magnitude of the swash motions, $Rs(y,t)$ correlated consistently better with $\beta_{mean}(y,t)$ than $\mathrm{Max}(P_{br})(y,t)$ or $\int P_{br}\mathrm{d}x(y,t)$ (see Tables 3.2 and 3.4). However, the multiple regression results show that one must account for alongshore changes in wave breaking patterns in order to best predict alongshore variations in runup height. The model showed the best skill when measures of the fraction of broken waves and the cross-shore positions of breaking were

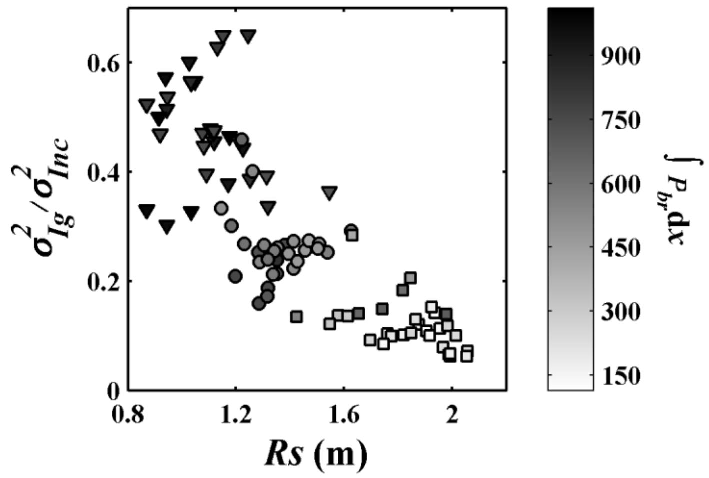

Figure 3.9. Scatter plot of the ratio between the variance integrated over infragravity σ^2_{Ig} and incident frequencies σ^2_{Inc} as a function of significant runup height *Rs*. Triangles, circles and squares represent data obtained at low, mid and high tide respectively. Color bar represents the amount of wave breaking calculated as $\int P_{br}dx$.

simultaneously used as inputs which possibly results from neither of these quantities being an optimum descriptor for wave energy dissipation. As mentioned earlier, the method used for estimating the probability of breaking did not distinguish breaking-generated foam (directly associated with wave dissipation) from residual foam, left behind the waves after they break. Additionally, though the cross-shore position of wave breaking is potentially related to the depth of the bar crest and therefore the wave dissipation over it, it does not explain alongshore changes in dissipation patterns that might occur shoreward of the bar crest (such as over the region where the shoal was observed). The nonlinear relationship observed between *Rs* and wave breaking might be also associated with the inability to have a precise measure of wave energy dissipation.

3.4.2 Incident swash

A large part of the temporal variations in the swash amplitude was driven by dissipation of the incident band of the swash. Analysis of Figures 3.6a and 3.6b shows that the incident swash variance σ^2_{Inc}, which amounted (on average) to 89%

and 68% of the total swash variance at high and low tide (Table 3.5) follows a similar behavior to *Rs*. The infragravity variance tends to follow an opposing trend, as also observed by *Guedes et al.* (2011). However, an interesting pattern can be observed. Between mid and high tide, 64% and 71% of the total changes in (alongshore-averaged) *Rs* and σ^2_{Inc} were observed (see Table 3.4). Conversely, most of the alongshore-averaged changes in beach slope β_{mean} (64%) occurred between low and mid tide. For the small wave heights that occurred during the experiment, the period between mid and high tide represents a transition when most waves changed from breaking to non-breaking over the sandbar (see Figure 3.3). It appears that this transition plays a major role in the dissipation pattern of the incident wind waves (notice that 56% of the alongshore-averaged changes in Max(P_{br}) were observed during the mid-to-high tide period, in agreement with the incident dissipation pattern).

The degree of dominance of the incident over the infragravity band of the swash was associated with the Iribarren number ξ_0 (Figure 3.10, r^2=0.56). The high intercept obtained from regression analysis between these two variables implies that this relationship does not hold for extreme energetic conditions, where the Iribarren number is typically smaller than 0.3 and the infragravity band has been shown to account from 85% to 98% of the total energy in the swash (*Ruessink et al.*, 1998; *Ruggiero et al.*, 2004; *Sénéchal et al.*, 2011).

Table 3.4. Alongshore-averaged parameters.

	Low tide	***Mid tide***	***High tide***
Rs (m)	*1.10*	*1.36*	*1.84*
σ^2_{Inc} (m^2)	*0.053*	*0.092*	*0.188*
σ^2_{Ig} (m^2)	*0.024*	*0.023*	*0.021*
β_{mean}	*0.086*	*0.118*	*0.136*
Max(P_{br}) (%)	*61.1*	*34.9*	*14.2*

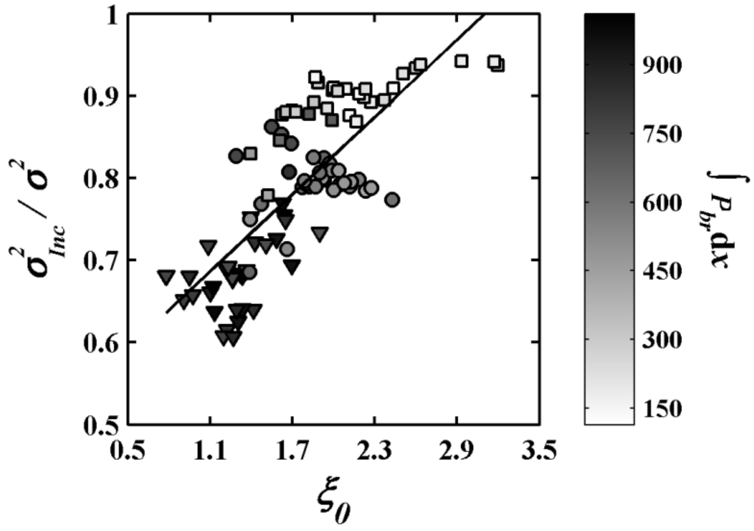

Figure 3.10. Scatter plot of the relative amount of incident variance σ^2_{Inc}/σ^2 as a function of the Iribarren number ξ_0, calculated using Equation (3.1) and β_{mean} as the beach slope. Triangles, circles and squares represent data obtained at low, mid and high tide respectively. Color bar represents the amount of wave breaking calculated as $\int P_{br}\mathrm{d}x$. The equation of the regression line is $\sigma^2_{Inc}/\sigma^2 = 0.16\xi_0 + 0.51$.

Table 3.5. Percentages of the total swash variance at incident and infragravity frequencies.

		Low tide	***Mid tide***	***High tide***
σ^2_{Inc}	*min*	*61*	*69*	*78*
	max	*77*	*86*	*94*
	mean	*68*	*80*	*89*
	std	*4*	*3*	*3*
σ^2_{Ig}	*min*	*23*	*14*	*6*
	max	*39*	*31*	*22*
	mean	*32*	*20*	*11*
	std	*4*	*3*	*3*

3.4.3 Infragravity swash

The infragravity band of the swash spectrum showed large alongshore variability during all periods (Figures 3.6c, 3.7, Table 3.1), despite the absence of well-developed three dimensional features on the beach face (Figure 3.2). The biggest changes in σ^2_{Ig} (up to a factor of 3) happened during low tide, when both wave breaking and σ^2_{Ig} were greatest (Figures 3.3, 3.6, Table 3.4). During mid and high tide, though, alongshore changes were also large with σ^2_{Ig} varying by more than a factor of two. The σ^2_{Ig} was found to be significantly correlated with β_{mean} at mid and high tide (Table 3.2), in contrast to the results reported by *Stockdon et al.* (2006) who found generally no correlation between these variables when three dimensional morphological features were not well developed. However, the patterns were not consistent, with positive correlation observed during mid tide and negative during high tide (see Table 3.2). The infragravity variance σ^2_{Ig} was also found to be significantly correlated with $\int P_{br}\mathrm{d}x(y)$ at low tide (when no significant correlation between σ^2_{Ig} and β_{mean} was observed) and mid tide (when wave breaking and beach slope were not significantly correlated). Nevertheless, none of these correlations were strong (in agreement with *Stockdon et al.*, 2006) and one would expect the alongshore modulation of infragravity variance to have been also controlled by processes other than the local beach face slope and the adjacent degree of wave breaking over the bar.

The shape of the spectrum at infragravity frequencies displayed distinct alongshore patterns. In contrast to some previous observations (e.g. *Guza and Thornton*, 1982; *Ruessink et al.*, 1998; *Holland and Holman*, 1999), prominent peaks were observed below the sea/swell frequencies at distinct alongshore positions (Figure 3.7), especially at low and mid tide when relatively more energy was present at infragravity frequencies. There were also alongshore positions where the infragravity spectral shape was considerably flatter. The alongshore variation in the infragravity peaks might be indicative of the presence of edge waves. Figure 3.11 shows the wavenumber-frequency spectra $E(k,f)$ obtained at mid tide using the IMLE technique. Assuming a stationary wave field, the wave energy associated with edge waves would be expected to extend along ridges in wavenumber-frequency space governed by the dispersion relationship for edge waves. Here, the dispersion relationship was evaluated using a numerical model that accounts for nearshore bathymetry (*Howd et al.*, 1992) to include the effects of the sandbar on the theoretical dispersion lines (*Bryan et al.*, 1998). Although most of the energy in $E(k,f)$ is concentrated in the wavenumber-frequency regions corresponding to leaky waves, some ridges within the low-mode edge wave region can be observed (Figure 3.11). The most prominent ridge lies near the lower mode number n=0 with some energy also lying between modes n=1 and n=2, and peaks between $f_p/2$ and $f_p/3$ (consistent with the frequency spectra) and wavelengths around 40–60 m. These patterns appeared for the three periods analyzed (not shown). Although the mechanisms responsible for generating the edge wave signals observed here are not clear, these observations agree with other studies showing the importance of lower-mode edge waves in the infragravity band of the swash spectra (e.g. *Oltman-Shay and Guza*, 1987) and might be related with the alongshore modulation of infragravity swash found in this dataset.

The edge wave dispersion patterns were not homogeneous along the beach. Frequency-wavenumber spectra estimated over moving sequences of adjacent time series (each sequence spanning 90 m alongshore) show that the low-mode edge wave dispersion patterns were modified according to the alongshore location of these sequences (Figure 3.12). Numerical model predictions of the low-mode dispersion lines using the average profile over each section (Figure 3.12, dashed lines) show such variability to be explained by small alongshore variations in the bar-trough morphology although a mismatch between the locations of some of the ridges in $E(k,f)$ and modeled dispersion lines can be observed. Such differences possibly originated from inaccurate estimates of the nearshore bathymetry (low frequencies are particularly sensitive to the offshore bathymetry, which was inferred from the video images), the effects of alongshore currents (e.g. *Howd et*

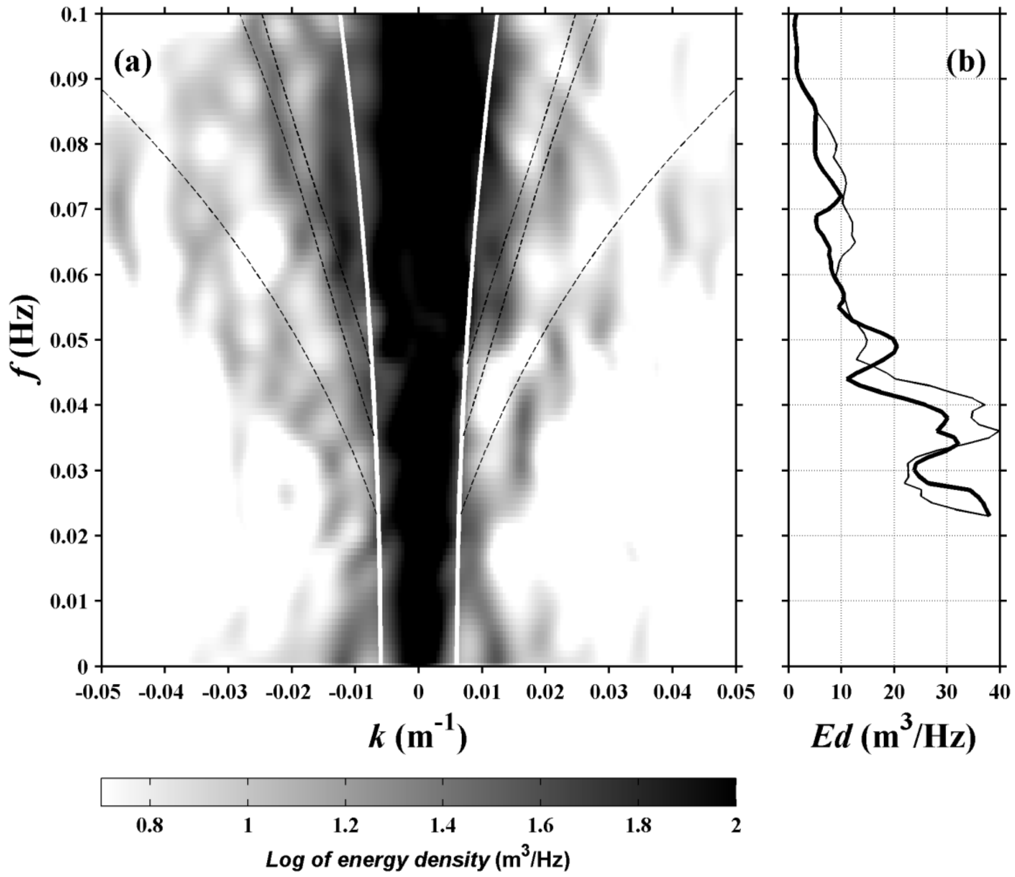

Figure 3.11. (a) Wavenumber-frequency spectra $E(f,k)$ of runup elevation time series estimated at mid tide using the IMLE method, over 16 time series spaced every 10 m alongshore, between -150 m ≤ Y ≤ 0 m. White thick solid lines show the leaky wave cut-off calculated as $\omega^2 = gk$ (where ω is the radian frequency $2\pi f$) with a wavenumber offset of 0.006 m^{-1} (following *Ciriano et al.*, 2005). White dashed lines show numerical model predictions of modes n=0, 1 and 2 edge waves from the bottom to the top. Color bar represents the logarithm of energy density *Ed*. (b) Maximum energy density over the region corresponding to the numerical model prediction of mode-zero edge wave (evaluated for each frequency, between the wavenumber satisfying the dispersion relationship ± 0.005 m^{-1}), plotted against wave frequency f. Thick and thin lines are associated with positive and negative wavenumbers respectively. Contributions from leaky modes have not been included.

al., 1992; *Oltman-Shay and Howd*, 1993; *Bryan and Bowen*, 1998) which were not measured during the experiment (notice that the low-mode ridges are not symmetric along the *k*-space) or linear approximations in the edge wave model (*Ciriano et al.*, 2005). The relative contribution of edge waves to the total energy density spectrum also changed alongshore. Figure 3.13 shows that the percentage of energy within the region corresponding to edge waves in the $E(k,f)$ was greatest near the southern end of the beach, where the shoal was observed (see Figure 3.3). This pattern was observed for the three stages of tide (Figure 3.13) and suggests that edge waves might have been predominantly forced around the location where the shoal was observed, due to enhanced nonlinear energy transfer over the shoal, and dissipated part of their energy as they propagated away from this region. This is also consistent with observations of *Henderson and Bowen* (2002) who showed infragravity energy to be higher near the region of infragravity forcing.

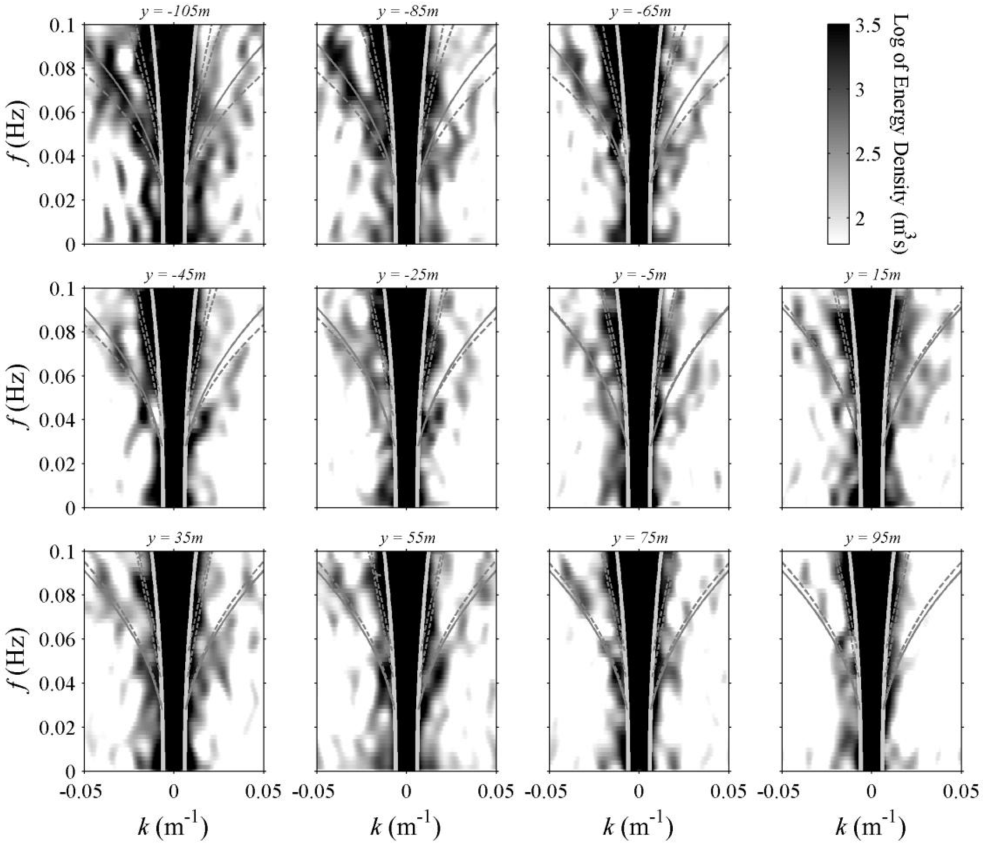

Figure 3.12. Wavenumber-frequency spectra $E(f\text{-}k)$ of runup elevation time series estimated at high tide using the IMLE method. Spectra were estimated over sequences of 10 adjacent hourly time series spaced every 10 m alongshore (central alongshore position is shown at the top of each panel). Thick solid lines show the leaky wave cut-off with a wavenumber offset of 0.006 m^{-1} (see the caption of Figure 3.11). Dashed lines show numerical model predictions of modes n=0, 1 and 2 edge waves from the bottom to the top, using a profile averaged over the alongshore location of each estimate. Thin solid lines show numerical model predictions of mode n=0 edge wave using a profile averaged over the whole analyzed region.

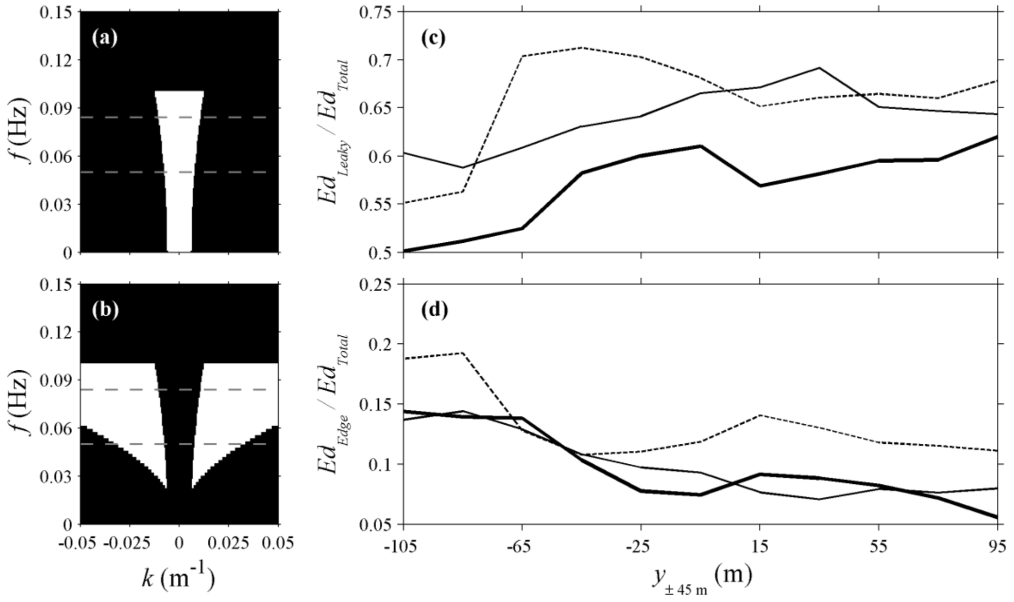

Figure 3.13. Left panels: frequency *f* plotted as a function of alongshore wavenumber *k* showing the *f*-*k* space (in white) over which the *E*(*k*,*f*) was integrated to estimate the leaky (a) and edge waves (b) contributions (shown on the right). Right panels: proportion of energy density *Ed* within the regions corresponding to leaky (c) and edge waves (d) plotted as a function of alongshore position on the beach with dashed, thin and thick lines representing data obtained at low, mid and high tide. Each *E*(*k*,*f*) spectrum was calculated using 10 adjacent time series spanning 90 m along the beach centered at $y_{\pm 45\ \mathrm{m}}$.

3.5 Conclusion

Large alongshore variability in swash motions was observed on an intermediate beach not characterized by the presence of well-developed, three dimensional morphological features such as prominent beach cusps, mega-cusps or crescent sandbars. Most of the variability occurred as a result of changes in the incident band of the swash which was always the dominant component of the swash motions. These changes were observed to be primarily driven by variations in the local beach face slope although alongshore variability in wave breaking over the bar also contributed to these changes. However, when tidal variations were also accounted for, variation in bar-induced wave breaking was the dominant control on swash height. Accounting for the combining effects of beach slope and wave breaking dissipation was found to be critical to explaining alongshore changes in swash height.

The shape of the spectra at infragravity frequencies was not always white but showed prominent peaks for some alongshore locations on the beach, near the frequencies corresponding to half and one-third of the incident peak. These infragravity peaks were possibly associated with the presence of low-mode edge waves which were detected in the swash observations during the three stages of the tide. These alongshore-trapped waves might have been predominantly forced around the location where a shoal was observed and appear to have dissipated part of their energy as they propagated along the coast away from the shoal. The low modes might have caused part of the alongshore variability in infragravity swash height observed here which was not well explained by changes in the local beach face slope or the degree of wave breaking over the bar. However, the infragravity band is often not dominant under intermediate and reflective conditions such as those observed in this study and therefore edge waves are not expected to be the dominant process driving alongshore changes in swash motions under these conditions.

Chapter 4

Observations of wave energy fluxes and swash motions on a low-sloping, dissipative beach

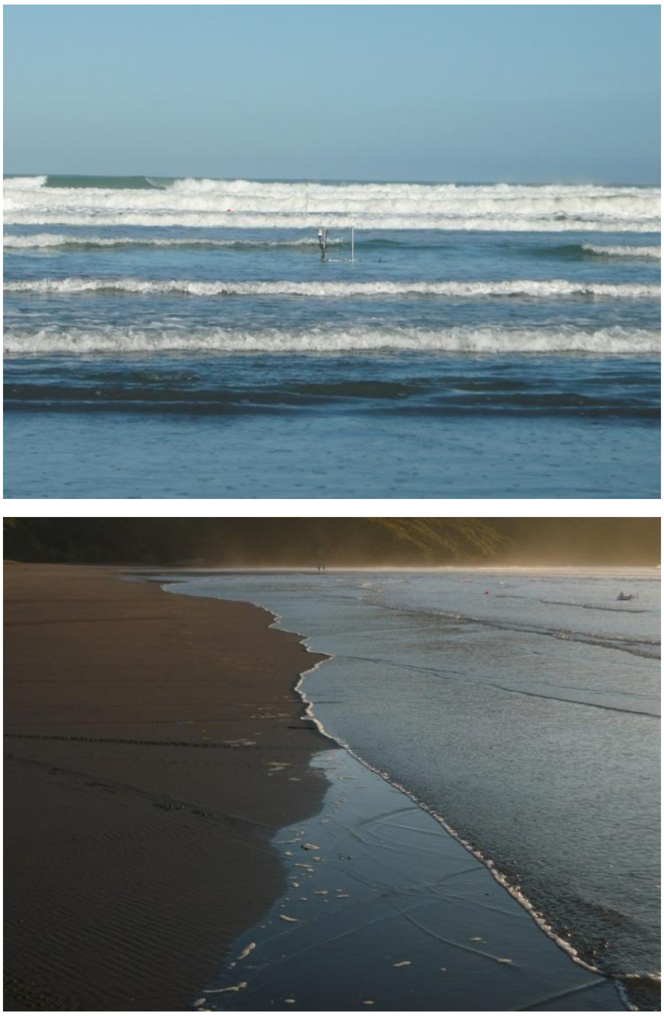

R. M. C. Guedes, K. R. Bryan, G. Coco (in preparation), Observations of wave energy fluxes and swash motions on a low-sloping, dissipative beach, submitted to *Journal of Geophysical Research*.

Contribution of authors

Chapter 4 presents the article entitled “Observations of wave energy fluxes and swash motions on a low-sloping, dissipative beach”, submitted in December 2012 to the *Journal of Geophysical Research*. In this study, an extensive field collection of offshore and surfzone wave measurements, intertidal beach morphology surveys and video runup data are analysed to investigate the surfzone control on swash oscillations on a low-sloping, dissipative beach.

The entire field dataset was obtained during a field experiment in Raglan, New Zealand, which I designed and executed as part of my PhD. I also wrote the code to perform the statistical methods, processed and analysed all the data, produced the figures, and wrote the manuscript. My co-authors assisted with the planning and execution of the field experiment, edited drafts, and provided advice on direction.

Abstract

Field observations of swash and ocean waves show that runup saturation at infragravity frequencies (< 0.05 Hz) can occur under mild offshore energy conditions if the beach slope is sufficiently gentle. Infragravity saturation was observed for higher-frequency (> 0.025–0.035 Hz) infragravity waves, where typically less than 5% of the (linear) energy flux was reflected from the beach and where, similar to the sea-swell band, the swash energy was independent of offshore wave energy. The infragravity frequency range of saturation was determined by the tide, with saturation extending to lower frequencies at low tide when the local beach face slope over the concave-shaped profile was gentler. Runup was strongly dominated by infragravity frequencies, which accounted on average for 96% of the runup variance, and its energy levels were entirely consistent with strong infragravity wave dissipation observed in the surfzone, particularly when including the nonlinear contributions to the wave energy fluxes. Our observations show evidence of nonlinear interactions involving infragravity and high-frequency, harmonic waves, and suggest that these harmonics could play a role in the wave energy balance near the shoreline on low-sloping, dissipative beaches.

Keywords: swash, waves, infragravity, energy flux, dissipation.

4.1 Introduction

Energy spectra of wave-driven shoreline oscillations (runup) can be dominated by low-frequency infragravity motions (0.004–0.05 Hz), below the sea-swell frequency range (0.05–0.4 Hz) that normally dominates the offshore wave spectrum (e.g., *Guza and Thornton*, 1982; *Guza et al.*, 1984; *Holman and Bowen*, 1984; *Holland et al.*, 1995; *Raubenheimer et al.*, 1995; *Ruessink et al.*, 1998; *Ruggiero et al.*, 2004; *Sénéchal et al.*, 2011). This frequency downshift implies dissipation of (steeper) waves at sea-swell frequencies, which occurs mostly due to breaking in shallow water (e.g. *Thornton and Guza*, 1983), and energy transfer to gently-sloping infragravity waves (e.g. *Henderson et al.*, 2006), for which breaking is less likely to occur. Infragravity swash motions can provide the main mechanism for sediment transport on low-sloping, dissipative beaches (*Butt and Russell*, 2000) and therefore predicting their occurrence and magnitude is a critical component of shoreline change models. Yet, we do not have a clear understanding of the processes that control the infragravity wave transformations between the very shallow surfzone and swash zone as only few field observations (e.g., *Holland et al.*, 1995; *Raubenheimer et al.*, 1995) have linked cross-shore wave evolution patterns in shallow water to infragravity swash motions.

Low-frequency infragravity waves can be excited by interactions of short waves at sea-swell frequencies in the shoaling region. *Longuet-Higgins and Stewart* (1962) showed that a pair of short waves with closely-spaced frequencies f_1 and f_2 and wavenumbers k_1 and k_2 excite group-bound, out-of-phase infragravity waves with frequency and wavenumber $f_1 - f_2$ and $k_1 - k_2$, due to low-frequency modulations of mass and momentum fluxes associated with the wave groups. As the water depth decreases and the short wave pair shoals, the interaction becomes nearly resonant, since the bound wave frequency and wavenumber approach those satisfying the dispersion relationship, causing energy to be more easily transferred from the short to the infragravity waves (e.g., *Battjes et al.*, 2004). This transfer has been demonstrated in field observations, where statistically-significant phase coupling involving pairs of sea swell and infragravity waves at their difference frequency has been observed using bispectral analysis (e.g. *Hasselmann et al.*, 1963; *Elgar and Guza*, 1985; *Herbers et al.*, 1994; *Ruessink*, 1998a; *Sheremet et al.*, 2002).

Within the surfzone, the sea-swell wave amplitude becomes depth-limited (e.g., *Thornton and Guza*, 1983; *Howd et al., 1991*; *Raubenheimer et al.*, 1996) and the groupiness of short waves drastically decreases (*List*, 1991) due to wave breaking. The group-bound long waves are believed to be 'released' and propagate onshore as free waves (*Longuet-Higgins and Stewart*, 1962; *Janssen et al.*, 2003), eventually reflecting from the beach. Infragravity forcing may also take place near the edge of the surfzone due to group-induced temporal and spatial variations in the breakpoint position (*Symonds et al.*, 1982; *Lippmann et al.*, 1997). Nearshore infragravity energy increases with offshore sea-swell wave energy (*Holman*, 1981; *Guza and Thornton*, 1982; 1985). However, recent observations have shown that infragravity dissipation might limit energy increases in very shallow water, due to bottom friction (e.g. *Henderson and Bowen*, 2002), infragravity wave breaking (e.g., *Battjes et al.*, 2004; *van Dongeren et al.*, 2007) or nonlinear energy transfers from low frequency back to higher frequency motions (e.g., *Henderson et al.*, 2006; *Thomson et al.*, 2006).

Swash motions are dominated by infragravity frequencies when dissipation influences the sea-swell wave energy range more than the infragravity energy range. Such conditions are usually met on gently-sloping, dissipative beaches, characterized by low values of a nondimensional beach steepness parameter, the Iribarren number ξ_0 (*Iribarren and Nogales*, 1949; *Battjes*, 1974)

$$\xi_0 = \frac{\beta}{\left(H_0/L_0\right)^{1/2}}, \qquad (4.1)$$

where β is the beach slope (for a planar beach), H_0 is the deep water wave height and L_0 is the deep water wavelength. However, the roles of offshore conditions (H_0 and L_0) and surfzone conditions (β) in controlling infragravity swash are still debated. For example, *Guza and Thornton* (1982) measured swash motions under mildly dissipative conditions (β and H_0 roughly between 0.03–0.05 and 0.5–1.5 m respectively, ξ_0 ~ 0.3–1.4) and found that whereas vertical swash excursions (runup) at sea-swell wave frequencies were saturated (independent of H_0), infragravity runup R_{Ig} increased linearly with H_0, at a rate of 0.7. Similar linear dependence was found by *Ruessink et al.* (1998) for a site exposed to highly dissipative conditions (β ~ 0.017, H_0 ~ 0.5–5 m, ξ_0 ~ 0.05–0.3) although a much smaller coefficient of proportionality, 0.18, was observed. *Holman and Sallenger* (1985), analyzing a dataset obtained under broader (and overall more reflective) environmental conditions (ξ_0 ~ 0.5–4), found R_{Ig} (normalized by H_0) to be linearly dependent on ξ_0, suggesting that beach slope and wavelength may also be important. The beach slope effect was confirmed by *Ruggiero et al.* (2004) who observed alongshore changes in R_{Ig} under highly dissipative conditions (ξ_0 ~ 0.05–0.25) to be linearly dependent on β. Alternatively, *Stockdon et al.* (2006) examined infragravity runup for a dataset composed of measurements from 10 different field experiments that spanned a range of ξ_0 and found R_{Ig} to be best predicted using a parameter dependent only on H_0 and L_0 (and no significant linear relationship with β). More recently, *Guza and Feddersen* (2012) showed that infragravity runup may also depend on incident wave directional and frequency spreading.

There is also mounting evidence that infragravity swash can be saturated, or independent of offshore wave conditions (*Ruessink et al.*, 1998; *Ruggiero et al.*, 2004; *Sénéchal et al.*, 2011) in a similar way to swash at incident frequencies (e.g., *Huntley*, 1977; *Guza and Thornton*, 1982; *Holman and Sallenger*, 1985; *Raubenheimer and Guza*, 1996). Infragravity swash saturation is consistent with breaking of infragravity waves and has typically been observed under highly energetic offshore wave conditions (when the long waves are steeper). *Ruessink et al.* (1998) suggested the lowest frequency for which saturation occurs f_s to be related to ξ_0, with f_s within the infragravity range for ξ_0 roughly less than 0.3. The authors observed different patterns for R_{Ig} when $\xi_0 < 0.3$ and linked these differences to infragravity saturation. *Ruggiero et al.* (2004) found infragravity saturation to extend into somewhat lower frequencies for alongshore regions where the beach face slope was gentler (for equal offshore wave conditions). Infragravity swash saturation has been typically inferred from the characteristics of the swash spectra and their relationship with offshore wave conditions.

This work explores the exchanges of energy between the inner surfzone and the swash using new in-situ observations of cross-shore wave evolution in very shallow water coupled with video observations of wave breaking patterns and swash motions, obtained on a low-sloping dissipative beach. Although swash observations are common, and infragravity saturation has been documented in previous studies, the swash infragravity levels have not been linked to the flux of energy from the surfzone, and how and where the energy transfer between incident and infragravity frequencies occurs has not been fully explored. We use simultaneous measurements of water pressure and velocity obtained at different cross-shore distances from the shoreline (controlled by changes in tide) to estimate cross-shore linear and nonlinear wave energy fluxes and nonlinear energy transfers among frequencies, based on equations described by *Henderson et al.* (2006) and *Sheremet et al.* (2002). Our findings indicate that infragravity dissipation is strong within the surfzone, increases with infragravity wave frequency and plays a pivotal role in controlling the run-up spectrum.

4.2 Theory

In order to investigate the possible surfzone control on infragravity swash observations, an energy balance between infragravity growth and dissipation was evaluated from simultaneous observations of pressure and velocity in the surfzone. In addition, the cross-shore locations and frequency components involved with such growth and dissipation were determined using bispectrum analysis.

4.2.1 Energy balance

Henderson et al. (2006) proposed a conservative, depth-integrated, alongshore-uniform energy balance for infragravity waves in shallow water

$$\frac{\partial F(f)}{\partial x} = W(f)\,, \tag{4.2}$$

to describe cross-shore changes in infragravity net energy flux $F(f)$, based primarily on the energy transfer $W(f)$ to infragravity waves from waves at other frequencies, where f is the cyclic frequency. The cross-shore coordinate x is defined as positive seaward.

The net energy flux $F(f)$ at infragravity frequency f is calculated following *Henderson et al.* (2006) as

$$F(f) = hC_f(\eta, u) + C_f(\eta, M) + C_f(S_{xx}, u)\,, \tag{4.3}$$

where $C_f(a, b)$ denotes the co-spectrum of real-valued variables a and b, h is the mean water depth, η is the sea-surface elevation around the mean water level, and u is the cross-shore velocity (positive seaward). M and S_{xx} represent the slowly varying part of the sea swell mass flux and cross-shore component of the sea swell radiation stress, respectively, and are given by

$$M = \eta' u'\,, \tag{4.4}$$

and

$$S_{xx} = g^{-1} h u' u' + \eta' \eta' / 2\,, \tag{4.5}$$

where g is the acceleration due to gravity and primes ($'$) denote band-passed filtering between 0.05 and 0.4 Hz. Note that Equations (4.3) and (4.5) have been scaled to be dimensionally consistent with Equation (2) in *Sheremet et al.* (2002). The first term on the right hand side of (4.3) corresponds to the linear component $F_L(f)$ of the net energy flux and, assuming cross-shore propagation, can be decomposed into shoreward propagating $F_L^-(f)$ and seaward propagating $F_L^+(f)$ components (*Sheremet et al.*, 2002):

$$F_L^{\pm}(f) = \frac{\sqrt{gh}}{4}\left[C_f(\eta,\eta) + (h/g)C_f(u,u) \pm \left(2\sqrt{h/g}\right)C_f(\eta,u)\right], \qquad (4.6)$$

with $F_L(f) = F_L^+(f) - F_L^-(f)$ (the sign convention adopted here for the two components is the opposite of that in *Sheremet et al.* (2002), where u is positive shoreward). The second and third terms on the right hand side of (4.3) are nonlinear corrections which have similar magnitudes when integrated over infragravity frequencies (*Henderson et al.*, 2006). The nonlinear component of the net energy flux $F_{NL}(f)$ is defined here as the sum of these two terms.

The nonlinear energy transfer term in (4.2), assuming nearly shore-normal shallow water waves, is defined as (*Henderson et al.*, 2006)

$$W(f) = C_f\left(S_{xx}, \partial u/\partial x\right), \qquad (4.7)$$

with positive and negative values indicating energy transfer to and from waves with frequency f, respectively. The cross-shore gradient of the cross-shore velocity $\partial u/\partial x$ is calculated from the shallow water mass conservation equation with the wave mass flux term neglected:

$$\frac{\partial u}{\partial x} = -\frac{1}{h}\left(\frac{\partial \eta}{\partial t} + u\frac{\partial h}{\partial x}\right), \qquad (4.8)$$

where t is time and all other symbols have been previously defined.

4.2.2 Forced waves

Following previous studies (e.g. *Elgar and Guza*, 1985; *Herbers et al.*, 1994; *Ruessink*, 1998a; *Sheremet et al.*, 2002) the source of wave energy associated with forced infragravity waves is investigated in terms of the digital bispectrum $B(f_1, f_2)$ (*Hasselmann et al.*, 1963)

$$B(f_1, f_2) = \mathrm{E}\left[A_{f_1} A_{f2} A^*_{f_1+f_2}\right], \tag{4.9}$$

where E[ ] represents the expected-value, A_{f_n} are complex Fourier coefficients at the n^{th} frequency component and the asterisk indicates complex conjugate. The bispectrum measures the statistical dependence among three waves with frequencies (f_1, f_2, f_1+f_2). $B(f_1, f_2)$ vanishes if the wave triads are independent and have random phases, such as in a linear wave field. On the other hand, nonlinear coupling between two primary waves and a forced, secondary wave yields a $B(f_1, f_2)$ which is statistically different than zero. A relative measure of the phase coupling between the wave triads can be obtained by the normalized magnitude and phase of the bispectrum, defined as the bicoherence $b(f_1, f_2)$ and biphase $\theta(f_1, f_2)$ and calculated respectively as (*Kim and Powers*, 1979)

$$b(f_1, f_2) = \frac{\left|B(f_1, f_2)\right|}{\left(\mathrm{E}\left[\left|A_{f1} A_{f2}\right|^2\right] \mathrm{E}\left[\left|A_{f_1+f_2}\right|^2\right]\right)^{1/2}}, \tag{4.10}$$

and

$$\theta(f_1, f_2) = \tan^{-1}\left[\frac{\mathrm{Im}\{B(f_1, f_2)\}}{\mathrm{Re}\{B(f_1, f_2)\}}\right], \tag{4.11}$$

where Im{ } and Re{ } represent the imaginary and real parts. Different combinations of the A_{f_n} coefficients have been used to normalize the bispectrum in (4.10) and calculate $b(f_1, f_2)$ (e.g. *Herbers et al.*, 1994; *Ruessink*, 1998a). The normalization factor adopted here follows *Kim and Power* (1979) and *Elgar and Guza* (1985) and ensures $0 \leq b \leq 1$. The 95% significance level on zero bicoherence $b_{95\%}$ is calculated as (*Haubrich*, 1965)

$$b_{95\%} \geq (6/DoF)^{1/2}, \qquad (4.12)$$

where *DoF* is the number of degrees of freedom.

4.3 Method

4.3.1 Description of field experiment and data reduction

The field data were collected between 08–09 November 2010 at Ngarunui Beach, Raglan, an exposed, dissipative beach located on the west coast of New Zealand's North Island (Figure 4.1). Ngarunui is about 2 km in length, constrained by an inlet to the north and a headland to the south, and frequently characterized by the presence of groundwater seepage above the swash zone (*Huisman et al.*, 2011). The beach is composed by fine–medium, black sand (*Sherwood and Nelson*, 1979) (the median grain size at the measurement positions was about 400 μm) and a gentle slope (the average slope β_{mean} over the intertidal region was about 0.014, see Figure 4.2). The field site commonly experiences energetic offshore wave conditions with average offshore significant wave height H_0 and mean spectral period T_m of 2.0 m and 7.0 s, respectively (*Gorman et al.*, 2003). The tides are semidiurnal and typically range between 1.8 (neap) and 2.8 m (spring tides) within the adjacent estuary (*Heath*, 1976) (the tidal range on the open coast was as high as 3.1 m during the period of the experiment).

Simultaneous time series of pressure and velocity were recorded using three Acoustic Doppler Velocimeters (ADVs) in the intertidal region and an Acoustic Doppler Current Profiler (ADCP) offshore in about 17 m water depth (Figure 4.1 shows the location of the instruments). Two of the ADVs were deployed along a cross-shore transect extending over 50 m (*NiwaInn* ADV, X = 220 m and *NiwaOut* ADV, X = 270 m, where X is the cross-shore coordinate of the grid defined for this study) and collected data at 8 Hz. The acoustic sensors were pointed downward and measured velocity at ~0.05 m above the bed. The third

ADV (*UoW* ADV) was mounted at the same cross-shore location of *NiwaOut* but 50 m farther in the alongshore (northward) direction Y, and measured at a sample rate of 4 Hz. However, the probe was upward looking and measured orbital velocity at ~0.95 m above the bed. All three instruments collected 20-min-long time series every half-an-hour, over three partial tidal cycles (when the sensors were submerged). After a quality control (following *Elgar et al.*, 2005) to remove bad time series or individual data points (i.e. those recorded when any of the sensors was in too shallow or out of the water) a total of 38, 47 and 36 simultaneous time series of pressure and velocity remained for *NiwaInn*, *NiwaOut* and *UoW* ADV, respectively. The measurements spanned cross-shore distances from the shoreline ΔX_S from 50 m (h = 0.55 m) to 184 m (h = 2.60 m). The ADCP collected hourly, 20-min-long, simultaneous time series of near-bottom pressure and near-surface velocity. The measurements were taken at 2 Hz and spanned the entire period when the ADVs were deployed. In addition, time series of (nearshore) mean water level h were collected every 5 min by averaging 2-min-long pressure records, obtained at 4 Hz using a Data Logger collocated on the frame used to deploy *UoW* ADV.

The morphology of the intertidal region of the beach was surveyed using a Real Time Kinematic (RTK) GPS. The GPS receiver was installed on a Quad bike that travelled over the beach around low tide, yielding dense coverage of the intertidal morphology. Analysis of an overlapping area surveyed on the two different days that included the position of the ADVs suggests that intertidal morphology changes were minimal (typically smaller than 0.03 m). A local grid was defined by translating and rotating the coordinate system of the survey, so as to have the origin at the location of a bench mark on the beach, and cross-shore coordinates X parallel to the line formed by *NiwaInn* and *NiwaOut* ADVs and increasing offshore (see Figure 4.1b).

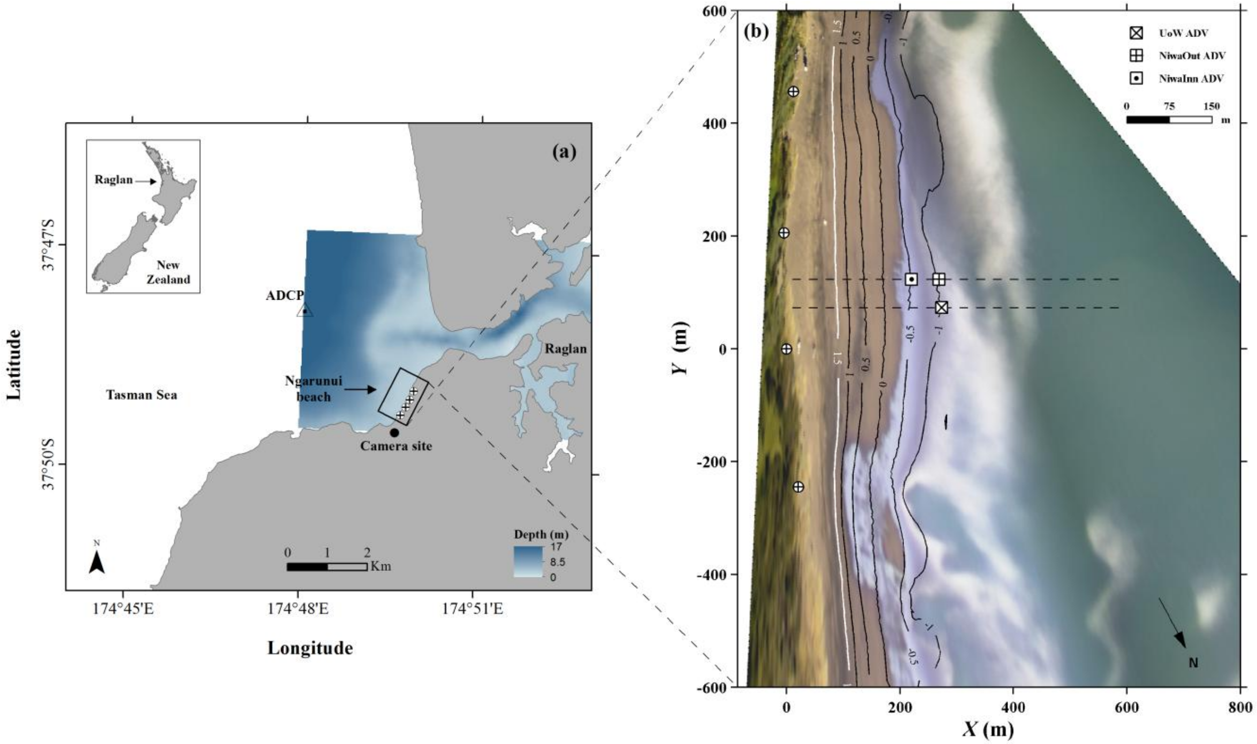

Figure 4.1. (a) Field site location with positions of cameras and ADCP indicated by black circle and the triangle respectively. White circles with black crosses show locations of bench marks (also shown on panel (b)). Bathymetry was digitized and interpolated from the New Zealand Nautical Chart NZ4421. (b) Mosaic composed by 20-min time-exposure (averaged) images obtained using two cameras on 09 November at 15:40 (DST), rectified to a plan view. Bright areas indicate regions of preferred wave breaking. White Squares and dashed lines show locations where ADVs were deployed and time stacks were defined respectively. Contour lines show intertidal bathymetry measured with the RTK with white line highlighting the beach contour corresponding to the highest mean water level (measured at location of *UoW* ADV) under which waves were measured. *X* and *Y* are the cross-shore and alongshore coordinates of the local grid defined for this study.

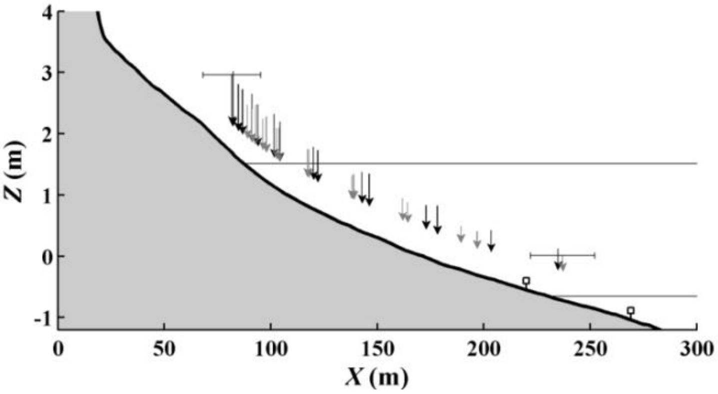

Figure 4.2. Beach profile averaged over the region where the three ADVs were deployed (see Figure 4.1b). Cross-shore positions of *NiwaInn* ADV (X=220 m) and *NiwaOut* and *UoW* ADVs (X=270 m) are shown by the white squares. Horizontal lines show the shallowest and deepest mean water levels (measured at location of *UoW* ADV) at which waves were measured in the surfzone. Vertical arrows point to the mean position of each swash run with their length corresponding to the respective value of (alongshore-averaged) Rs. Black and gray arrows are associated with data obtained on day 08 and 09 respectively. Horizontal bars at the top of lowermost and uppermost arrows highlight the cross-shore extension of the swash ($R_{mean} \pm 2\sigma_R$) for these two time series.

High-resolution images of the beach (1528 x 2016 pixels) were collected continuously at 2 Hz during daylight hours. The images were acquired using two digital cameras, mounted at the southern end of the beach (Figure 4.1a) at about 95 m above mean sea level. The combined field of view of the cameras spanned most of the subaerial beach and the surfzone. Figure 4.1b shows a mosaic created using time-averaged images defined from both cameras, rectified to a planview using known geometric transformations.

Swash oscillations were measured at two alongshore locations on the beach using the video images. Two cross-shore lines (*Niwa* and *UoW* lines) were defined on the images at the alongshore locations where the respective ADVs were deployed, as shown in Figure 4.1b (conversions between pixel and ground coordinates were made using the colinearity equations described by *Holland et al.* (1997) with corrections for lens distortions). Time stacks with cross-shore pixel resolution of ~0.2 m were defined over these lines by interpolating the intensities on each selected image frame at the locations of these two lines (see *Aagaard and Holm* (1989) and *Guedes et al.* (2011) for more detailed description of the technique). The period selected for creating the time stacks included the daylight hours when the ADVs were collecting data, and resulted in 32, 30-min-long, 2-Hz time stacks defined over each line (e.g., Figure 4.3b). The swash was defined as the most shoreward moving-edge of water identifiable on the time stacks (see Figure 4.3b) and was manually digitized. This definition has been shown by *Holman and Guza* (1984) and *Holland et al.* (1995) to be consistent with swash measurements obtained using resistance wires deployed near the seabed. Finally, the digitized swash positions from the time stacks were converted into time series of vertical runup elevation by mapping each cross-shore swash position to an elevation Z, which was accurately know from the (interpolated) RTK survey. The gentle slope of the beach resulted in high vertical pixel resolution over the intertidal region (~0.003 m).

The cross-shore wave breaking structure was defined by using the probability of wave breaking $P_{br}(x)$ which can be extracted from video images. The method was modified from *Guedes et al.* (2011) who used time stacks to approximate $P_{br}(x)$ as the probability of pixel intensity being greater than a threshold at any cross-shore location. Here, individual breaking waves were identified by taking the gradient of the pixel intensities in the time stacks over time, $\partial I/\partial t$, and locating sequences of positive followed by negative intensity gradients that typically characterized a broken wave. The result was an estimate of the number of breaking waves $N_{br}(x)$. The probability of breaking $P_{br}(x)$ was calculated by dividing $N_{br}(x)$ by the total number of individual wave crests observed during the same periods in 17 m water depth, which was defined from the ADCP pressure series as the length of the time series divided by the mean spectral period. Figure 4.3c shows examples of $P_{br}(x)$ obtained from the *Niwa* time stack near low, mid and high tide. Though this technique does not account for nonlinear interactions such as harmonic decomposition (e.g. *Elgar et al.*, 1997) which potentially increased the number of individual waves in the shoreward direction (see Section 4.5.3), $P_{br}(x)$ was consistent with the patterns visually observed from the time stacks (see Figure 4.3).

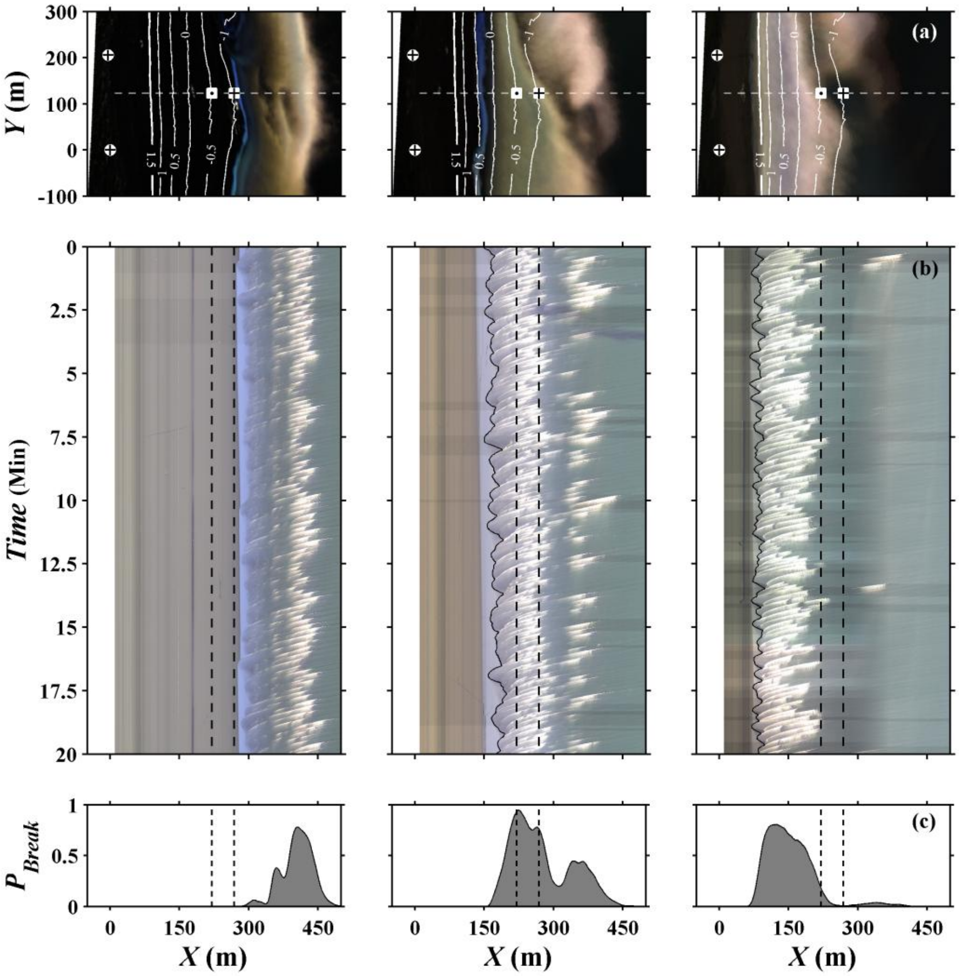

Figure 4.3. (a) Mosaics composed by 20-min variance images obtained using the two cameras deployed at Ngarunui Beach, rectified to plan views using known geometric transformations. Contour lines show intertidal bathymetry measured with the RTK. Horizontal dashed lines show one of the two locations where time stacks were defined (*Niwa* line). Inner and outer squares show positions of *NiwaInn* and *NiwaOut* ADVs respectively. White circles with crosses show two of the bench marks on the beach. (b) Time stacks created over the cross-shore location highlighted by the dashed line in (a). Black solid lines show digitized swash locations, when available. (c) Probability of breaking P_{break} estimated from the time stacks in (b), as a function of cross-shore position. Vertical dashed lines in (b) and (c) highlight the cross-shore positions of the two ADVs shown in (a). Left, mid and right panels are associated with data obtained near low tide (08 November, 17:10, η = -1.54 m), mid tide (08 November, 14:40, η = -0.08 m), and high tide (08 November, 11:40, η = 1.51 m) (times are in DST).

4.3.2 Analysis

The hydrodynamic data were analyzed in the frequency domain using spectral analysis. Runup and pressure surfzone spectra with frequency resolution *df* of 0.0039 Hz were estimated from Fourier transforms of the time series, segmented into 256 s, 75% overlapping sections, that were linearly detrended and tapered with a Hanning window. Offshore spectra with the same frequency resolution were estimated from the velocity time series collected by the ADCP at three different depth cells located just below the sea surface (spectra from the three cells were averaged). Linear wave theory was used to convert the pressure (ADVs) and velocity data (ADCP) into sea surface elevation.

Energy fluxes and nonlinear energy transfers were calculated by evaluating Equations (4.3)–(4.8) with the simultaneous time series of u and p collected by each ADV. A Lanczos filter was used to band-pass u and p to calculate time series of M and S_{xx} in (4.4) and (4.5). Time series of $\partial u/\partial x$ were estimated in (4.8) by (central) finite-differencing p to evaluate $\partial\eta/\partial t$, and approximating $\partial h/\partial x$ by "-" the local slope at the location of each ADV (although in the text we refer to the absolute value of beach slope, the frame of reference implies that the slope in fact is negative). The co-spectrum $C_f\ (a,\ b)$ in (4.3), (4.6) and (4.7) was estimated using the same parameter setting as for the spectrum.

Bicoherences and biphases were calculated from the ADVs as (4.10) and (4.11), after removing seaward propagating infragravity waves from the data, following *Elgar and Guza* (1985) and *Sheremet et al.* (2002). Seaward propagating infragravity waves are free and mix the phase structure between shoreward propagating infragravity waves at equivalent frequencies and sea-swell waves. The separation was performed by decomposing the data into surface elevation time series of shoreward propagating η^- and seaward propagating η^+ waves as (*Guza et al.*, 1984; *Sheremet et al.*, 2002)

$$\eta^{\pm} = \frac{1}{2}\left(p \pm u\sqrt{h/g}\right), \tag{4.13}$$

high-passing η^{+} to remove outgoing infragravity waves and adding back the two components. The bispectra estimated from these data had the same frequency resolution and *DoF* as the auto- and cross-spectra calculated using the ADV data. The relatively short time length of the time series was compensated by averaging bicoherence and biphase over several frequency pairs (see Section 4.4.3).

4.4 Results

4.4.1 Observations

Offshore sea-swell waves in 17 m water depth were mild during the field experiment and decreased in energy from the first to the second day. Offshore significant wave height H_0 decreased from about 1.3 to 1.0 m from the first to the third tidal cycle, where H_0 was defined using the ADCP spectra as

$$H_0 = 4\left(\int_{0.05\mathrm{Hz}}^{0.24\mathrm{Hz}} E_d(f)df\right)^{1/2}, \tag{4.14}$$

with $E_d(f)$ denoting the energy density and the term inside the parenthesis representing the variance associated with the defined frequency band. Peak period T_p, calculated as the inverse of the peak frequency in $E_d(f)$, decreased from about 12 to 10 s during the same period (see Figure 4.4a). Offshore peak wave direction *Dp*, determined from the ADCP, was roughly constant near 270° (W).

The beach morphology was relatively alongshore-homogeneous over the intertidal region where the ADVs were deployed. The three instruments were placed near the center of the embayment of a mega-cusp with wavelength about 800 m (Figure 4.1b), where the intertidal cross-shore profile was concave upward (Figure 4.2). The local slope $\tan\beta$ increased by a factor of 4 from 0.008 at the lowermost to 0.032 at the uppermost location where swash was measured ($\tan\beta$ was ~0.01 at the location of the ADVs) and no sandbar was observed over the intertidal region. The Iribarren number ξ_0 (4.1), calculated using the local slope at the mean swash location tanβ and linear wave theory to estimate L_0, was characteristic of highly dissipative conditions, with small values changing by a factor of 4 (following tanβ) from low tide ($\xi_0 \sim 0.1$) to high tide ($\xi_0 \sim 0.4$). A NE-directed ($+Y \rightarrow -Y$) alongshore current, calculated by averaging the ADVs' velocity records **V**, was present, and increased in magnitude from negligible values at high tide (when the instruments were outside the surfzone) to about 0.4–0.5 m/s near the shallowest locations. A seaward component in **V** was observed, especially for measurements from *NiwaInn* and *NiwaOut* ADVs, and was likely caused by the presence of a rip channel that extended diagonally through the beach, from [X, *Y*] ~ [150, 500] m passing seaward of the outer ADVs (Figures 4.1b and 4.3a). The channel acted as a trough around mid-tide, separating an outer breaking region seaward of $X \sim 350$ m from an inner breaking region, where the waves broke continuously until they reached the swash zone (Figure 4.3; see also Figure 4.5). In contrast, at high tide the outer breaking region was too deep and breaking occurred mostly over the inner surfzone, shoreward of the channel, and near low tide the channel was shallow enough to be within the inner breaking region.

Figure 4.4 shows an overview of the wave conditions offshore, in the surf and swash zones during the experiment. Most of the energy in 17 m water depth was within sea swell frequencies (Figure 4.4a), with little energy (typically corresponding to less than 5% of the total wave variance σ^2_{ADCP}) observed at infragravity frequencies (see Figure 4.4e). Consistent with previous observations (e.g., *Okihiro and Guza*, 1995; *Thomson et al.*, 2006), offshore infragravity energy was somewhat tidally-modulated (Figure 4.4e, open circles), with the variance integrated over infragravity frequencies $\sigma^2_{Ig,\mathrm{ADCP}}$ significantly correlated with the tide η, with $r^2 = 0.23$ (hereinafter, correlation coefficients r^2 are significant with p-value < 0.05). In contrast to the waves in 17 m water depth, most of the swash energy was constrained within infragravity frequencies, with peaks between 0.01

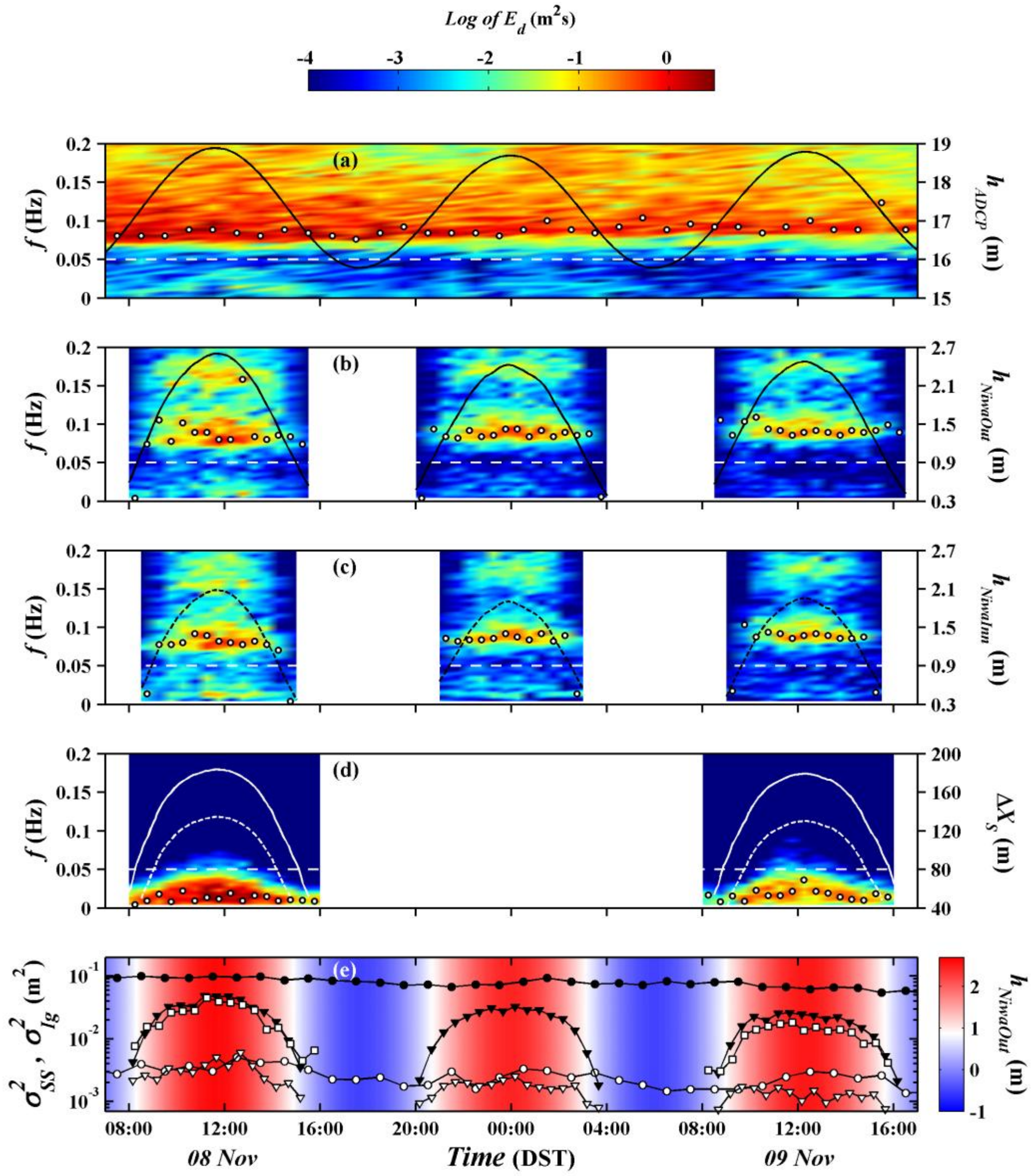

Figure 4.4. (a–d) Logarithm of energy density E_d as a function of frequency f and time, with white circles showing the peak frequency for each data run. (a) Offshore E_d obtained from the ADCP, with solid line (right axis) showing the mean local water depth h_{ADCP}. Surfzone E_d obtained from the (b) *NiwaOut* and (c) *NiwaInn* ADVs, with solid and dashed (black) lines (right axes) showing the mean local water depth $h_{NiwaOut}$ and $h_{NiwaInn}$ respectively. (d) Swash E_d calculated from the (video) runup time series, obtained over the alongshore location of NiwaOut and NiwaInn ADVs, with solid and short-dashed lines (right axis) showing the distance ΔX_S from these two ADVs to the shoreline, respectively. Horizontal white dashed line in panels (a)–(d) highlight the frequency used to separate incident and infragravity bands. (e) Time series of wave variance integrated over incident (solid markers) and infragravity (open markers) bands, obtained from: ADCP (circles), *NiwaOut* ADV (triangles) and video runup data (squares) (incident runup variances ranged between ~10^{-4} and 10^{-3} m^2 and are not shown here). Colors represent the mean water depth at the location of *NiwaOut* ADV.

and 0.02 Hz (Figure 4.4d), near the infragravity wave peaks observed offshore. The infragravity runup variance $\sigma^2_{Ig,\mathrm{R}}$ was nearly 2 orders of magnitude larger than the sea-swell runup variance $\sigma^2_{SS,\mathrm{R}}$, accounting on average to 96% of the total swash variance σ^2_{Ig} (similar to observations under highly energetic offshore wave conditions). Moreover, the infragravity swash variance decreased from the first to the second day and was also modulated by the tide, with $\sigma^2_{Ig,R}$ increasing by an order of magnitude from low to high tide within each tidal cycle (Figure 4.4e).

Similarly to the waves in 17 m water depth, most of the wave energy in the surfzone was within sea swell frequencies (Figures 4.4b, 4.4c and 4.4e). The variances integrated over both sea-swell $\sigma^2_{SS,\mathrm{ADV}}$ and infragravity frequencies $\sigma^2_{Ig,\mathrm{ADV}}$ decreased from the deepest to the shallowest locations (and from the first to the third tidal cycle). However, the sea-swell waves experienced greater dissipation, which resulted in $\sigma^2_{Ig,\mathrm{ADV}}$ accounting for an increasing proportion of the total wave variance σ^2_{ADV} from the deepest (h ~ 2.60 m, $\sigma^2_{Ig,\mathrm{ADV}} \big/ \sigma^2_{\mathrm{ADV}}$ ~ 0.05) to the shallowest locations (h ~ 0.55 m, $\sigma^2_{Ig,\mathrm{ADV}} \big/ \sigma^2_{\mathrm{ADV}}$ ~ 0.40). Over the inner surfzone region between *NiwaInn* ADV and the upper boundary of the swash zone, the sea-swell waves were nearly completely dissipated, as evidenced by the strong infragravity dominance observed in the runup spectra.

4.4.2 Linear energy fluxes

The linear component of the wave energy flux was predominantly shoreward throughout the surfzone (compare Figures 4.5a and 4.5b). The shoreward propagating linear energy flux $F^-_L(f)$ integrated over sea-swell frequencies, $F^-_{L,SS}$, accounted for roughly 98–99% of the (total) sea swell energy flux $(F^-_{L,SS} + F^+_{L,SS})$, consistent with the nearly total sea-swell dissipation observed in the runup spectra. At infragravity frequencies, the contribution of the (linear) shoreward component $F^-_{L,Ig}$ ranged from 90% when the ADVs were farthest from the shoreline to 70% when they were closest, as a result of the shoreward infragravity dissipation. The dissipation of $F_L^-(f)$ was clearly accelerated within the breaking region for both sea swell and infragravity frequencies (Figure 4.5c).

In contrast to $F_L^-(f)$, which mimicked the surfzone spectrum (compare Figures 4.4b and 4.5a), the seaward propagating linear energy flux $F_L^+(f)$ was dominated by infragravity frequencies (Figure 4.5b) and strongly resembled the patterns observed in the runup spectrum (see Figure 4.4d). The infragravity component of the seaward propagating flux $F_{L,Ig}^+$ accounted on average for 74% of the outgoing linear energy flux, and increased by more than a factor of 4 from low to high tide within each tidal cycle (not shown), consistent with the infragravity modulation observed offshore ($F_{L,Ig}^+$ was significantly correlated with the tidally-modulated beach slope at the mean swash location tanβ, $r^2 = 0.44$, whereas its correlation with the tide itself was lower, with $r^2 = 0.32$).

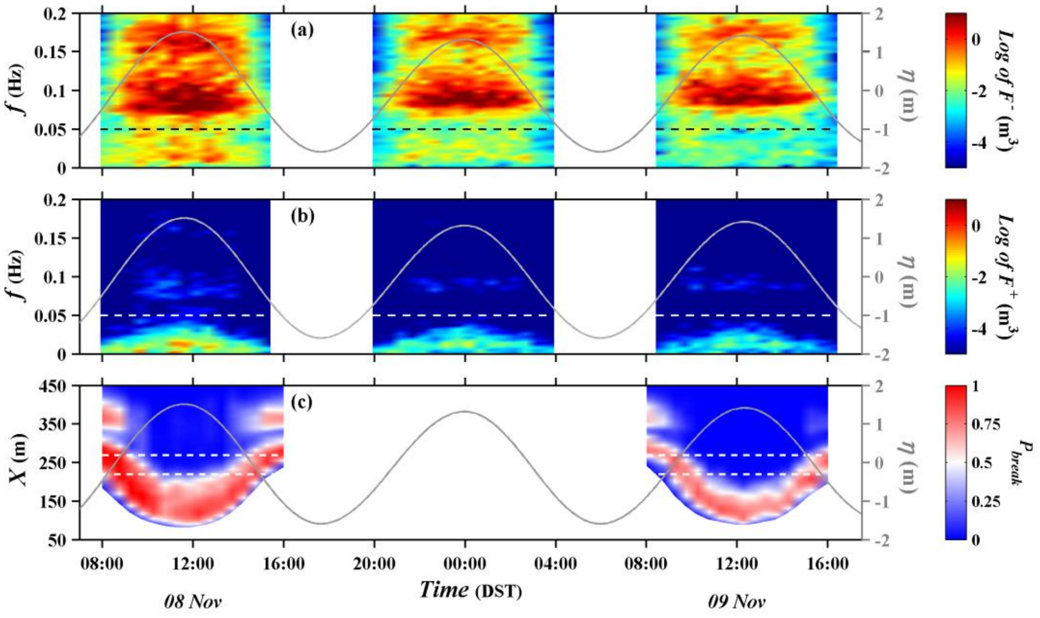

Figure 4.5. Logarithm of (a) shoreward propagating (F^-) and (b) seaward propagating (F^+) components of the linear energy flux as a function of frequency f (left axis) and time. Horizontal dashed lines highlight the frequency used to separate incident and infragravity bands. (c) Probability of breaking P_{break} as a function of cross-shore position X (left axis) and time. White dashed lines indicate cross-shore positions of *NiwaOut* (270 m) and *NiwaInn* (220 m) ADVs. Cross-shore positions shoreward of the mean swash locations have been blanked. In all panels, gray solid lines (right axes) represent tide level η.

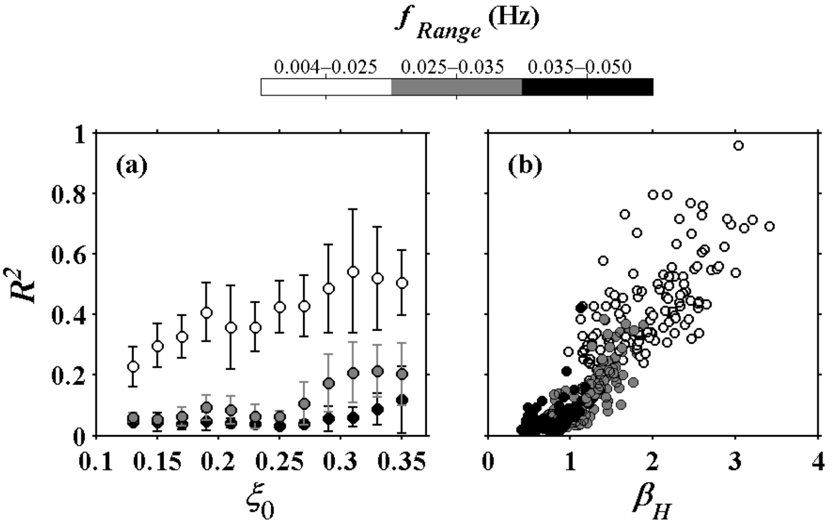

Figure 4.6. Reflection coefficient R^2 of partitioned infragravity bands, shown by the colors, as a function of (a) Iribarren number ξ_0 (Equation 4.1) and (b) normalized bed slope parameter β_H (Equation 4.16). Data for each frequency band have been grouped in panel (a) by 0.02 ξ_0 intervals, with the circles and bars representing the average and standard deviation associated with each group for the three infragravity bands.

Most of the infragravity energy observed in both the runup and outgoing energy flux spectra were within very low infragravity frequencies (< 0.02 Hz). In order to investigate the infragravity behavior in detail, the infragravity band was further divided into three frequency bands Ig_1 ($0.004 < f < 0.025$ Hz), Ig_2 ($0.025 < f < 0.035$ Hz) and Ig_3 ($0.035 < f < 0.05$ Hz), and bulk reflection coefficients R^2 were calculated as (*Elgar et al.*, 1994; *Sheremet et al.*, 2002)

$$R^2 = \frac{\int_{lf}^{hf} F_L^+(f)df}{\int_{lf}^{hf} F_L^-(f)df}, \tag{4.15}$$

where lf and hf represent the low and high frequency cutoff for each of these bands. Figure 4.6a shows R^2 calculated for the three bands plotted as a function of the Iribarren number ξ_0. For the three infragravity bands, R^2 was smaller than one, consistent with shoreward dissipation of the linear infragravity energy flux, and increased with ξ_0 (which changed mostly due to tidal-induced changes in $\tan\beta$). However, the dissipation was clearly greater for Ig_2 and Ig_3, with the bulk reflection coefficient R^2 typically a factor of 3–4 larger for the lowest frequency band Ig_1. R^2 was around 0.05 for both Ig_2 and Ig_3 for $\xi_0 < {\sim}0.3$, suggesting almost complete dissipation for these infragravity bands, although an increase in R^2 was observed for higher ξ_0. A good parameterization for R^2 was obtained using a normalized bed slope parameter β_H proposed by *Battjes et al*. (2004), which accounts for changes in water depth within a wavelength as

$$\beta_H = \frac{h_x}{\omega}\sqrt{\frac{g}{H(\omega)}}, \tag{4.16}$$

where h_x is a 'characteristic' value of bed slope, ω is the radian frequency $2\pi f$ and $H(\omega)$ is the height of waves with radian frequency ω. Here, h_x has been approximated by the slope at the mean swash location $\tan\beta$, ω was taken as the central radian frequency of each infragravity band, and $H(\omega)$ was calculated as (4.14) by replacing $E_d(f)$ by the energy density associated with incoming waves, $F_L^-(f)/\sqrt{gh}$, and setting the limits of integration to lf and hf. The bulk reflection coefficient R^2 was strongly linearly correlated with β_H (Figure 4.6b) with r^2 = 0.78.

4.4.3 Nonlinear energy fluxes and energy transfers

The net energy flux $F(f)$ at infragravity frequencies was dominated by its linear component $F_L(f)$ (Figures 4.7a–d). However, the nonlinear terms $F_{NL}(f)$ increasingly contributed to $F(f)$ from the breaking to the shoaling regions and from the first to the third tidal cycle (when the offshore wave energy was decreasing), specially for the lowest frequency band Ig_1 (Figure 4.7d). In contrast to $F_L(f)$, $F_{NL}(f)$ was mostly seaward-directed (positive values), except for the shallowest locations (Figure 4.7b), and its increasing contribution near mid–high tide resulted in seaward net flux for some frequencies in $F(f)$ that were not observed in $F_L(f)$ (compare Figures 4.7a and 4.7c). Similar to $F_{NL}(f)$, the wave energy transfer $W(f)$ was positive during mid–high tide at infragravity frequencies (Figure 4.7e), indicating energy transfer to infragravity waves from waves at other frequencies. At the shallowest locations within each tidal cycle, when the ADVs were well within the surfzone (see Figure 4.5c), $W(f)$ was typically negative at infragravity frequencies, consistent with nonlinear energy transfer from infragravity waves.

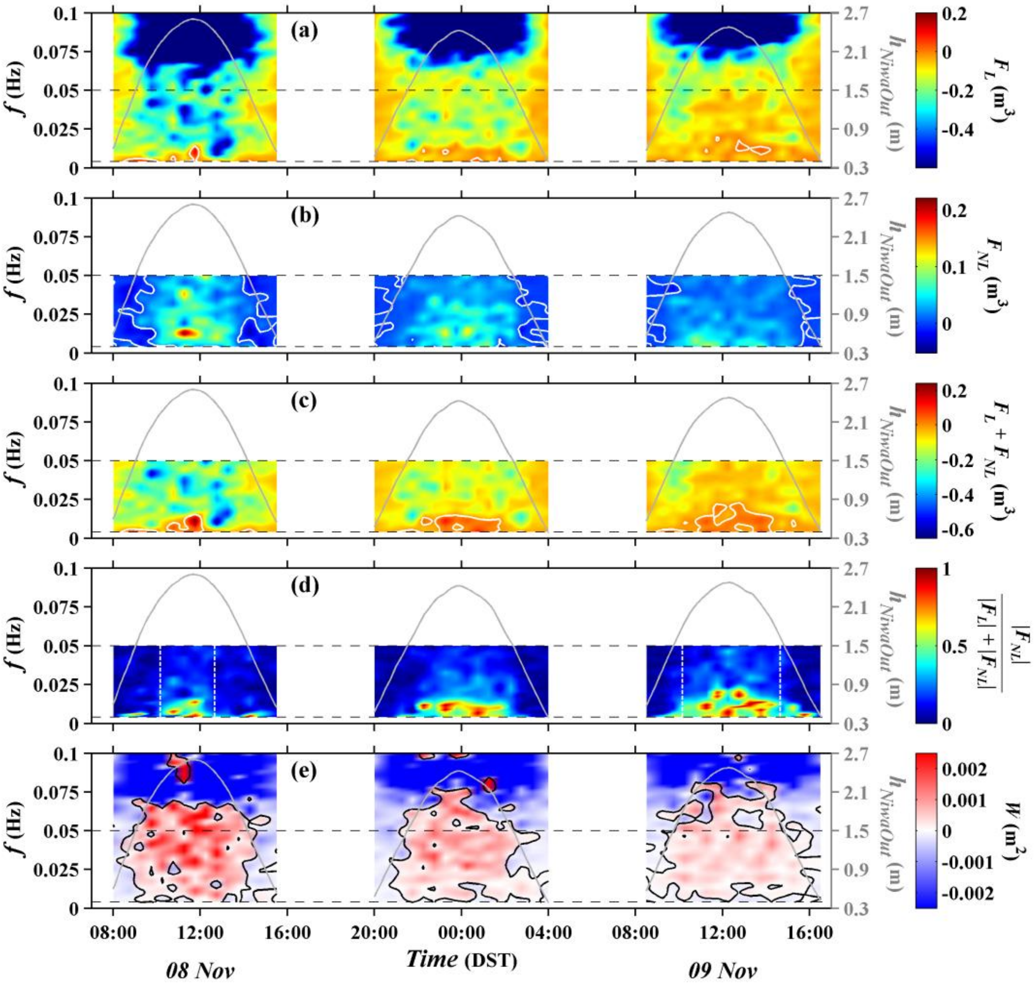

Figure 4.7. Net wave energy flux components and wave energy transfer as a function of frequency f and time. (a) Linear component of the net wave energy flux F_L. (b) Nonlinear component of the net wave energy flux F_{NL} at infragravity frequencies. (c) Total net wave energy flux F at infragravity frequencies. Positive and negative values in panels (a–c) indicate seaward and shoreward net fluxes respectively. (d) Contribution of the nonlinear component to net wave energy flux at infragravity frequencies. White dashed lines delimit shoaling and breaking regions within each tidal cycle (defined here as those where $P_{Break} < 0.05$ and $P_{Break} > 0.05$, respectively). (e) Energy transfer W to (positive values) and from (negative values) waves with frequency f. Contours highlight transitions between positive and negative values. In all panels, data from *NiwaOut* ADV are shown, and gray solid lines (right axes) represent mean local water depth $h_{NiwaOut}$.

The cross-shore structure of $F(f)$ and $W(f)$ was investigated by integrating over the infragravity band (following *Henderson et al.*, 2006):

$$F_{Ig} = \int_{0.004\text{Hz}}^{0.05\text{Hz}} F(f)df, \;\; W_{Ig} = \int_{0.004\text{Hz}}^{0.05\text{Hz}} W(f)df, \tag{4.17}$$

and plotting against the tidally-modulated, mean distance from the shoreline ΔX_S (Figure 4.8). The observed net energy flux integrated over infragravity frequencies F_{Ig} typically diverged (increased seaward) when the ADVs were offshore of the inner surfzone, indicating a net energy gain (blue region), and converged when the ADVs were inside the surfzone, indicating a net energy loss (red region). The cross-shore region of energy gain extended closer and closer to the shoreline from the first (Figure 4.8a) to the third tidal cycle (Figure 4.8c) as the offshore wave energy decreased and the surfzone became narrower. In addition, $F_{Ig}(\Delta X_S)$ was normally higher during ebb tide (triangles) compared to the data obtained during flood tide (circles) within a given tidal cycle. The total nonlinear energy transfer to infragravity waves W_{Ig} was always positive over the cross-shore regions where infragravity gain was observed, consistent with observations of *Henderson et al.* (2006). On the other hand, positive values of W_{Ig} were also observed over regions of infragravity dissipation (e.g. Figure 4.8a, 130 m < ΔX_S < 165 m), suggesting a disagreement with the theoretical wave energy balance in (4.2).

The energy balance in Equation (4.2) was evaluated by calculating cross-shore changes in the (infragravity) net energy flux between simultaneous time series from *NiwaOut* and *NiwaInn* ADVs, $\Delta F_{Ig} = F_{Ig,NiwaOut} - F_{Ig,NiwaInn}$, and plotting against the nonlinear energy transfer to infragravity frequencies, integrated over the two ADVs

$$W_{Ig}^{INT} = \int_{X_{NiwaInn}}^{X_{NiwaOut}} W_{Ig}\, dx, \tag{4.18}$$

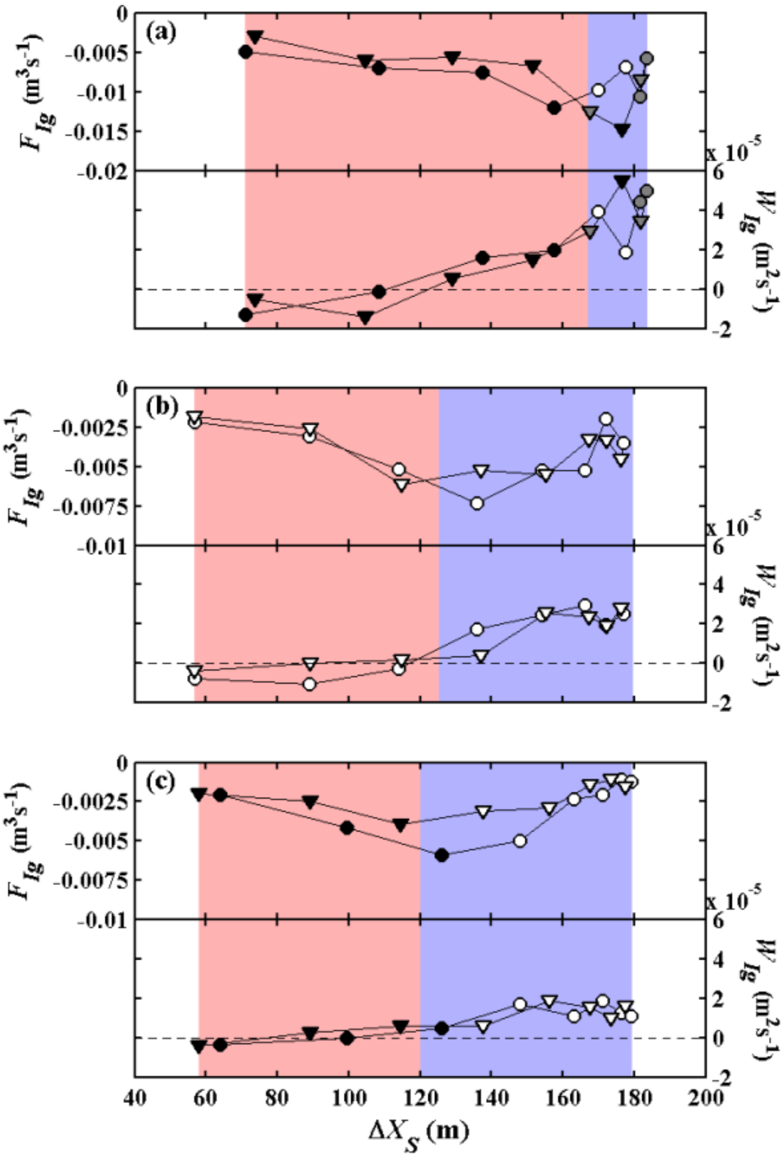

Figure 4.8. Net wave energy flux (top panels, left axes) and wave energy transfer (bottom panels, right axes) integrated over infragravity frequencies (F_{Ig} and W_{Ig}, respectively), as a function of distance from the shoreline ΔX_S. Panels (a–c) are associated with first, second and third tidal cycles respectively. Notice the different scale for F_{Ig} on panel (a). Circles and triangles show data obtained during flood and ebb tide. Black and white markers in panels (a and c) indicate *NiwaOut* ADV shoreward and seaward of the breakpoint position respectively (breakpoint positions are unknown during the second tidal cycle shown in panel (b), which occurred during night time). Gray markers in panel (a) indicate *NiwaOut* ADV seaward of inner breaking region but with a few set waves breaking offshore at outer breaking region (e.g. Figure 4.3b, right panel). Red and blue patches highlight cross-shore region where infragravity loss (F_{Ig} increasing shoreward) and infragravity gain (F_{Ig} increasing seawards) were observed. Data from *NiwaOut* ADV are shown.

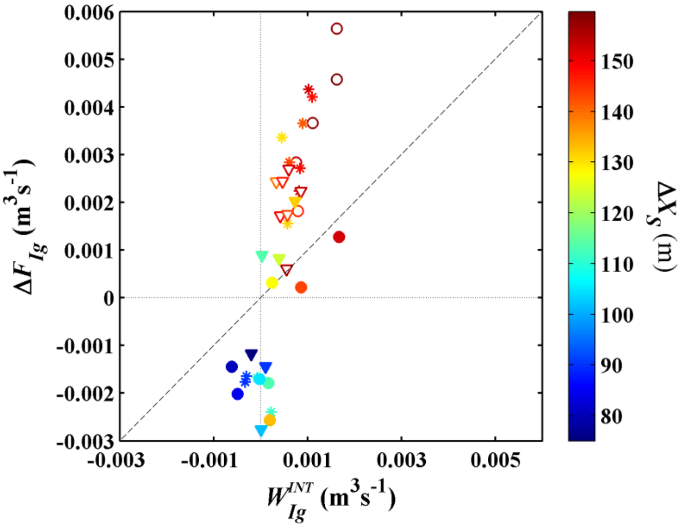

Figure 4.9. Change in total infragravity energy flux ΔF_{Ig} between *NiwaOut* and *NiwaInn* ADVs as a function of nonlinear transfer to (positive values) and from (negative values) infragravity motions W_{Ig}^{INT}. Circles, asterisks and triangles are associated with data obtained during first, second and third tidal cycle respectively. Colors indicate the distance from the shoreline ΔX_S. Solid and open markers (circles and triangles) indicate *NiwaInn* ADV shoreward and seaward of the breakpoint position respectively (breakpoint positions are unknown during the second tidal cycle (asterisks), which occurred during night time). Dashed line indicates agreement with the conservative energy balance.

with *dx* representing the cross-shore distance between the two instruments and W_{Ig}^{INT} evaluated using the trapezoidal rule. The observed ΔF_{Ig} and W_{Ig}^{INT} were significantly correlated (see Figure 4.9) with r^2 = 0.65. Positive and negative values for both energy transfer and changes in energy flux typically occurred when the inner ADV was outside (open circles and triangles) and inside the breaking region (solid circles and triangles), respectively. However, ΔF_{Ig} and W_{Ig}^{INT} did not balance (the slope of their linear regression line was 3.4), in disagreement with observations of *Henderson et al.* (2006) on a steeper barred beach under predominantly low energy conditions.

The bispectra observations showed consistent evidence of nonlinear energy transfers across the shoaling and breaking regions involving swell and harmonic frequencies. Figures 4.10a and 4.10d show example bicoherences $b(f_1, f_2)$ and biphases $\theta(f_1, f_2)$ calculated from *NiwaOut* ADV on 08 November at 22:40 DST, near high tide. Within the sea-swell band, strong bicoherence (b > 0.7) can be observed involving the incident wave peak f_p (f_2 ~ 0.085 Hz) with itself and its higher harmonics ($f_1 = nf_2$, where n is a positive integer), indicating nonlinear coupling between wave triads with frequencies [nf_2, f_2, nf_2+f_2] (Figure 4.10a). The pattern was repeated for the two higher harmonics as well (note the bicoherence peaks extending over f_2 ~ 0.17 Hz and f_2 ~ 0.26 Hz) and were similar to previous bispectra observations in shallow water (e.g. *Elgar and Guza*, 1985; *Sénéchal et al.*, 2002). The biphases associated with these nonlinear interactions typically ranged between 0°–70° (e.g., Figure 4.10b) suggesting waves with shapes changing from skewed (sharp peak and wide trough) to asymmetric (steep front face and gentle back face) forms, respectively (see *Elgar and Guza*, 1985). The cross-shore evolution of bicoherences and biphases involving the incident peak f_p and its harmonics was examined by averaging, for each bispectrum, $b(f_1, f_2)$ and (the modulus of) $\theta(f_1, f_2)$ over the area highlighted by the dark gray trapezium in Figures 4.10a ($\overline{b_{SS}}$) and 4.10b ($\left|\overline{\theta_{SS}}\right|$), which extended from [$f_1$, f_2] = [0.05–0.4, 0.07–0.09] Hz (the biphases $\theta(f_1, f_2)$ were averaged only over pairs for which $b(f_1, f_2) > b_{95\%}$, in order to avoid the random values normally associated with wave triads with non-significant bicoherences). Figures 4.10c and 4.10d show $\overline{b_{SS}}$ and $\left|\overline{\theta_{SS}}\right|$ calculated from *NiwaOut* ADV, as a function of the distance from the mean shoreline location ΔX_S. The nonlinear coupling of sea swell wave triads clearly decreased from the deepest locations outside of the surfzone ($\overline{b_{SS}}$ ~ 0.5) towards the shallowest locations within the inner surfzone region ($\overline{b_{SS}}$ ~ 0.25), and was followed by a systematic evolution from skewed to highly asymmetric shapes.

Significant bicoherence peaks involving infragravity modes were also observed in the bispectra (Figure 4.10a). The nonlinear coupling took place not only between infragravity waves with frequency f_2 and modes close to the incident peak f_1 ~ f_p (and their sum), but also for modes f_1 at higher frequencies, within the range of higher harmonics. Similar to $\overline{b_{SS}}$ and $\left|\overline{\theta_{SS}}\right|$, average bicoherences $\overline{b_{Ig}}$ and biphases $\left|\overline{\theta_{Ig}}\right|$ involving (at least) one infragravity mode were calculated for each bispectrum, by averaging $b(f_1, f_2)$ and $\theta(f_1, f_2)$ over [f_1, f_2] = [0.004–0.5, 0.004–0.05] Hz (light gray area in Figures 4.10a and 4.10b). The infragravity

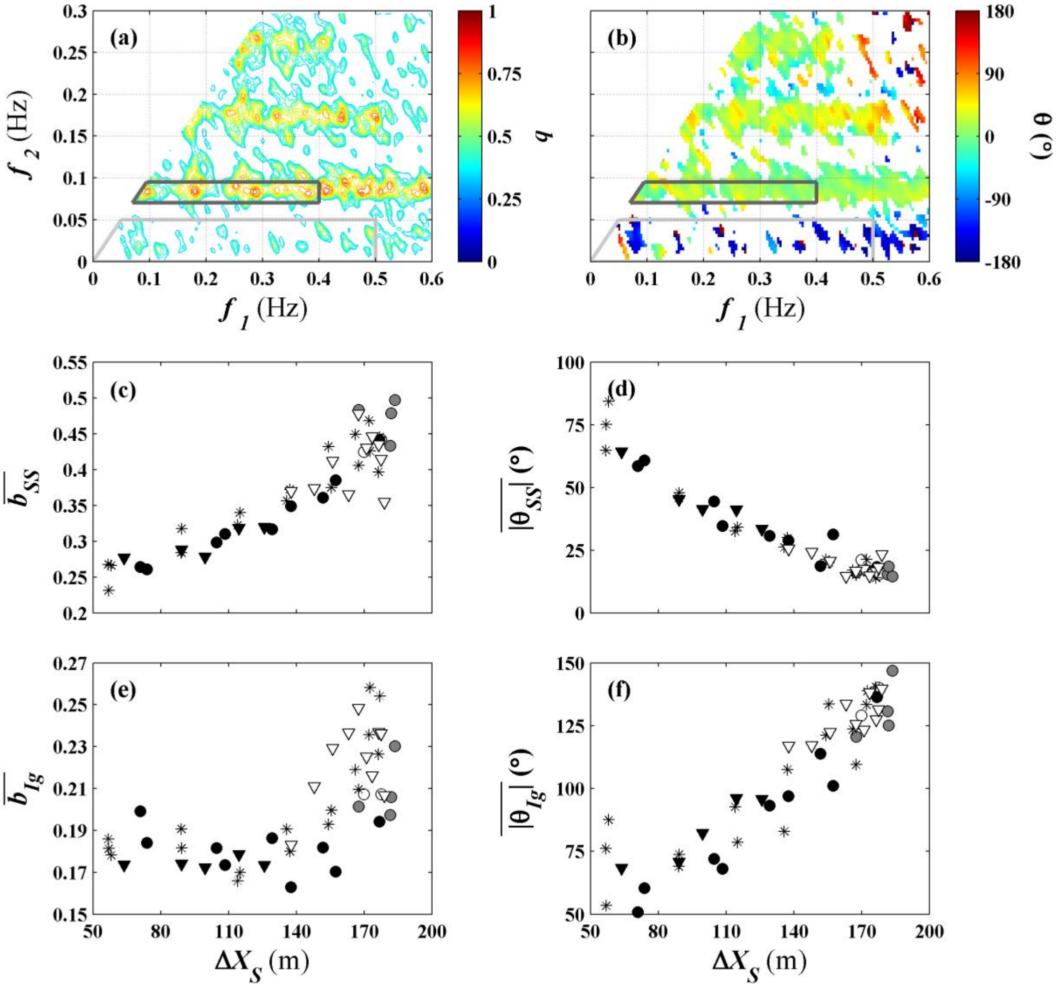

Figure 4.10. Example (a) bicoherence $b(f_1, f_2)$, and (b) biphase $\theta(f_1, f_2)$, calculated from a time series obtained by *NiwaOut* ADV at 22:40 (DST), during the second tidal cycle near high tide. Values associated with frequency pairs where no significant bicoherence (at the 95% confidence level) was observed have been blanked. (c) Bicoherences and (d) the modulus of biphases, averaged over the dark gray area on panels (a and b) to include frequency pairs involving coupling between sea-swell (and higher-frequency) modes, as a function of distance from the shoreline ΔX_S. (e) Bicoherences and (f) the modulus of biphases, averaged over the light gray area on panels (a and b) to include frequency pairs involving coupling between infragravity (and higher-frequency) modes, as a function of distance from the shoreline ΔX_S. Circles, asterisks and triangles are associated with data obtained during first, second and third tidal cycle respectively. Black and white markers in panels (c–f) indicate *NiwaOut* ADV shoreward and seaward of the breakpoint position respectively (breakpoint positions are unknown during the second tidal cycle which occurred during night time). Gray markers in panel (c–f) indicate *NiwaOut* ADV seaward of inner breaking region but with a few set waves breaking offshore at outer breaking region (e.g. Figure 4.3b, right panel). Biphases were averaged only over frequency pairs with bicoherence significantly different than zero (at the 95% confidence level). Data from *NiwaOut* ADV are shown.

bicoherences $\overline{b_{Ig}}$ showed a consistent cross-shore behavior over the three tidal cycles with values sharply decreasing shoreward as the waves started to break, and slightly increasing again at very shallow water (Figure 4.10e). On the other hand, the infragravity biphases $\left|\overline{\theta_{Ig}}\right|$ steadily decreased from ~150° at h = 2.6 m to near 50° at the shallowest locations around h = 0.6 m (Figure 4.10f).

4.5 Discussion

4.5.1 Swash motions

The energy density in the swash was consistent with changes to infragravity energy fluxes between *NiwaOut* and *NiwaInn* ADVs. We predicted infragravity energy fluxes within the swash zone $F_p(f)$ by linear-fitting the net energy fluxes simultaneously observed from the two ADVs (for each infragravity frequency component), and extrapolating the lines to a cross-shore position where the water depth h_{swash} was representative of that in the swash zone (defined here as 0.05 m). Predicted runup energy density $E_{d,p}(f)$ was then defined as

$$E_{d,p}(f) = \frac{F_p(f)}{\sqrt{gh_{Swash}}} \tag{4.19}$$

and compared with the energy density $E_d(f)$ directly estimated from the runup time series. Figure 4.11 shows time series of infragravity variances integrated from $E_d(f)$, as well as from $E_{d,p}(f)$ estimated using the linear $F_L(f)$ (a) and the total $F(f)$ net energy fluxes (b). Measured (Black lines) and predicted (gray lines) runup variances were similar, with the increasing trend from low (↓tanβ) to high tide (↑tanβ) generally well described. However, best results were obtained using $F(f)$, which included the nonlinear energy flux terms (Figure 4.11b). Though one may argue that the value chosen for h_{Swash} is somewhat arbitrary, the variance derived from the linear net flux $F_L(f)$ differed from the measured runup variance between the two days (Figure 4.11a), whereas $F(f)$ yielded more similar temporal changes for predicted and measured runup variances (which were significantly

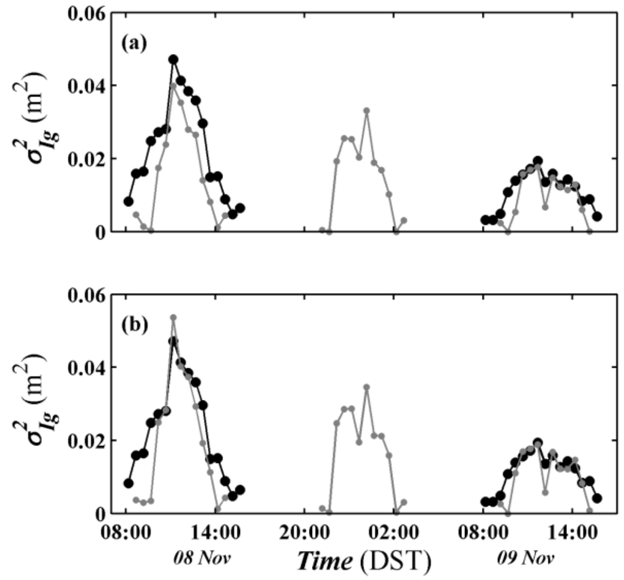

Figure 4.11. Time series of swash variance at infragravity frequencies (black lines with circles) and wave variance at infragravity frequencies extrapolated at the shoreline (gray lines with circles) using (a) the linear component of the net wave energy flux F_L, and (b) the total net wave energy flux F between *NiwaOut* and *NiwaInn* ADVs. Extrapolated energy fluxes were converted to energy density using linear wave theory and assuming water depth of 0.05 m (the same depth at which the F_L and F were extrapolated at).

correlated, r^2 = 0.79), for any h_{Swash} chosen. This is consistent with the observed changes in the relative contribution of the nonlinear energy flux $F_{NL}(f)$ from the first to the second day (Figure 4.7d) and support the conclusion of *Henderson et al.* (2006) that neglect of nonlinear infragravity energy fluxes might be a poor approximation.

Our observations suggest that sea-swell and most notably infragravity saturation may also occur under relatively mild offshore wave conditions if the beach slope near the shoreline is sufficiently gentle. The swash energy density $E_d(f)$ (on a log-log scale) decayed with frequency at the (negligible) sea-swell band at a linear rate of about f^{-4} (Figure 4.12a), and its temporal variability was very small compared to that observed at infragravity frequencies (Figure 4.12b), supporting the hypothesis of incident swash saturation. However, the f^{-4} 'roll-off' clearly extended into the highest infragravity band Ig_3 as well (Figure 4.12a), suggesting saturation also for this band. The saturation is consistent with the very low reflection coefficients R^2 (typically < 0.05) found for Ig_3, and also for Ig_2 when ξ_0 < ~0.3 (Figure 4.6a) and agrees with previous observation under highly energetic offshore wave conditions (e.g. *Ruessink et al.*, 1998; *Ruggiero et al.*, 2004; *Sénéchal et al.*, 2011). However, such conditions did not occur during our observations, suggesting that the saturation within the infragravity band was controlled by the very gentle slope near the shoreline. Note that R^2 did tend to increase for the three infragravity frequency bands with the Iribarren number ξ_0 (Figure 4.6a), which changed mostly due to changes in the beach slope at the mean swash location tanβ. Our findings support the hypothesis of *Ruessink et al.* (1998) in which infragravity saturation might be associated with ξ_0. The increase in R^2 for ξ_0 > ~0.3 observed for the two highest infragravity bands (especially Ig_2) is remarkably similar to the value of ξ_0 = 0.27 suggested by the authors as the threshold below which infragravity saturation occurs.

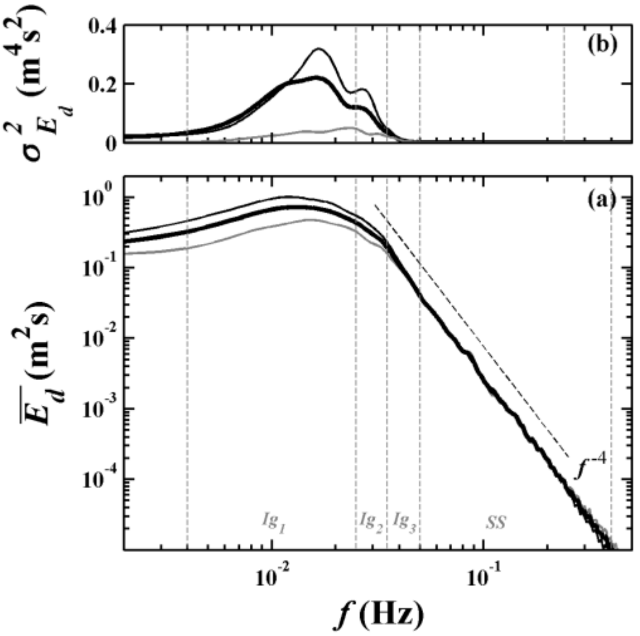

Figure 4.12. (a) Average of swash energy density for the first day (black thin solid line), second day (gray thin solid line) and over the entire period (black thick solid line) plotted on a log-log scale as a function of frequency f. Black dashed line shows the best fit of the saturated (linear on the log-log scale) band of the swash spectra (calculated between 0.03 Hz < f < 0.3 Hz). (b) Variance σ^2 of swash energy density as a function of f on a log scale (line styles are associated with the same periods defined for (a)). Vertical gray dashed lines delimit the frequency regions corresponding to the sea-swell and the 3 infragravity bands adopted in this study. Data have been averaged alongshore.

4.5.2 Nonlinear infragravity energy fluxes contributions

The nonlinear component of the net energy flux $F_{NL}(f)$ was observed to have a greater contribution to the net energy flux $F(f)$ outside of the breaking region (see Figure 4.7). Within the surfzone, the bulk infragravity net energy flux F_{Ig} (linear + nonlinear components) was very similar to its linear component $F_{L,Ig}$ suggesting that the nonlinear component could be neglected in very shallow water on low-sloping dissipative beaches. This is in contrast to observations of *Henderson et al.* (2006) near the shore on an intermediate beach (Duck), where $F_{NL,Ig}$ was found to be important. The contrasting patterns might be a result of contrasting morphologic and hydrodynamic conditions. Their observations took place on a steeper barred beach (their nearshore slope was about 0.07, see their Figure 1), with significant wave heights in 8-m depth between 0.3–1.2 m, so that non-breaking conditions potentially occurred within the region near the shore (in contrast to our observations).

4.5.3 Forced waves

The bispectral observations suggest that significant nonlinear energy transfer took place between incident swell waves and their harmonics between 2.6–0.6 m water depth (Figures 4.10a–d). The patterns are somewhat similar to field observations described by *Elgar and Guza* (1985) between h = 9–1 m, in which shoaling of sea swell waves caused the wave shape to change from skewed to asymmetric forms, as a result of continuous energy transfer to phase-coupled waves at harmonic frequencies, and changes in the phase structure among the nonlinearly coupled waves. Field observations have shown that the harmonics can eventually be released as they propagate over a sandbar, resulting in an increasing number of individual wave crests shoreward of the sandbar crest (e.g. *Elgar et al.*, 1997; *Masselink*, 1998; *Sénéchal et al.*, 2002; *Guedes et al.*, 2011). We observed a similar shoreward increase in the number of individual wave crests, even for a

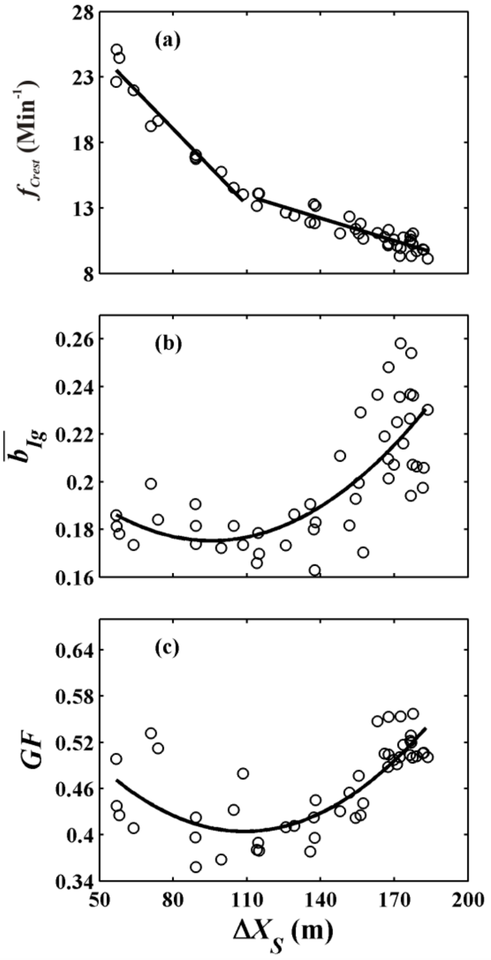

Figure 4.13. (a) Frequency of wave crests estimated as the number of wave maxima per minute, (b) Infragravity bicoherence $\overline{b}_{Ig}$ (see Figure 4.10) and (c) groupiness factor *GF*, as a function of the cross-shore distance from the mean shoreline location ΔX_S. Solid lines in panel (a) are best-fit lines calculated from data shoreward and seaward of ΔX_S = 110 m. Solid curves in panels (b) and (c) are second-degree polynomials fitted to the data. Data from *NiwaOut* ADV are shown.

more complex bathymetry lacking a well-defined sandbar. Figure 4.13a shows the number of individual wave crests per minute f_{Crest}, estimated from *NiwaOut* ADV using a modified version of the zero-crossing method (see *Guedes et al.*, 2011), as a function of the cross-shore distance from the shoreline ΔXs. The frequency of observed individual wave crests f_{Crest} increased by a factor of 2 from the farthest to the shallowest locations, with the rate of change in the shoreward direction getting higher at about ΔXs ~ 110 m (h ~ 1.2 m). The harmonic release can also be observed in the time stacks as the divergence of an individual wave into two wave crests, which propagate towards the shoreline with different wave speeds (not shown), and might be associated with the shoreward decrease in the nonlinear coupling involving sea-swell and harmonic waves observed in Figure 4.10c.

The cross-shore evolution of infragravity waves observed within the surfzone in very shallow water is a shoreward continuation of the progressive evolution that has been observed in deeper water by *Elgar and Guza* (1985). The infragravity biphases observed around 2.5 m water depth are close to the biphase of π for a bound wave produced by difference interactions, and their cross-shore evolution agrees with field (e.g., *Elgar and Guza*, 1985; *Masselink*, 1995) and laboratory observations (e.g., *Janssen et al.*, 2003; *Battjes et al.*, 2004) of increasing phase lag among interacting frequencies and forced bound waves in the shoreward direction. In fact, *Elgar and Guza* (1985) observed biphases for selected triads involving infragravity modes to decrease from about 170° to 140° for h between 6.0 and 2.0 m (see their Figure 12). Their shoreward-most observations were at similar depths and had similar biphases to our seaward-most observations (Figure 4.10f) suggesting that the phase shift progressively evolves towards very shallow water. This evolution is consistent with laboratory observations of *van Dongeren et al.* (2007), in which short waves propagating around the long wave crest in very shallow water converged on the crest as a result of long wave-induced changes in local depth and currents.

The breaking of waves at sea swell frequencies affected the evolution of waves at infragravity frequencies. Nonlinear wave coupling involving infragravity waves was clearly reduced as the short waves started to break (Figure 4.10e), and followed by a shoreward decrease in both the infragravity net energy flux and nonlinear wave energy transfer to infragravity waves (Figures 4.7–4.9). These observations are consistent with the abrupt decrease of nonlinear forcing within the surfzone, and agree with observations reported in previous studies (e.g., *Ruessink*, 1998a; 1998b; *Henderson and Bowen*, 2002; *Sheremet et al.*, 2002).

Figures 4.13b and 4.13c show respectively the averaged infragravity bicoherences $\overline{b_{Ig}}(\Delta X_S)$ and groupiness factor $GF(\Delta Xs)$, a relative measure of wave groupiness proposed by *List* (1991) and calculated from the ADV pressure time series. $GF(\Delta Xs)$ decreased in the shoreward direction for ΔXs > 110 m, as the waves started to break, which is possibly associated with the reduction in the infragravity coupling $\overline{b_{Ig}}(\Delta X_S)$ and nonlinear energy transfer W_{Ig} observed over the same region (see Figures 4.8 and 4.10). On the other hand, the (surfzone) region where ΔXs < 110 m, where the rate that harmonics were released increased (see the $f_{Crest}(\Delta X_S)$ slope change in Figure 4.13a), experienced a shoreward increasing trend for both $GF(\Delta Xs)$ and $\overline{b_{Ig}}(\Delta X_S)$. The surfzone wave groupiness observed here is also consistent with *List* (1991) who found significant wave height variability to persist within the saturated surfzone. Although the change in the slope of $f_{Crest}(\Delta X_S)$ at h ~ 1.2 m is not understood, we hypothesize that difference interactions among free waves at higher harmonic frequencies might have occurred within the surfzone. Figure 4.14a shows the nonlinear energy transfer $W(f_1+f_2, f_1)$ to (positive) and from (negative values) infragravity waves with frequency f_2 by triplets with frequencies f_1, f_2, and f_1+f_2, calculated (following *Henderson et al.*, 2006) as

$$W(f_1+f_2, f_1) = hC_{f_1+f_2,f_1}(u,u,\partial u/\partial x) + C_{f_1+f_2,f_1}(\eta,\eta,\partial u/\partial x) \qquad 4.20$$

where $C_{f1+f2,\, f1}$ denotes the co-bispectrum. Significant nonlinear energy transfers can be observed for triads involving an infragravity and two harmonic waves (region between dashed lines), in contrast to observations of *Henderson et al.* (2006) on a steeper barred beach, where most transfers occurred through triad interactions with swell frequencies (defined for 0.05 Hz < $[f_1+f_2, f_1]$ < 0.15 Hz). In addition, the proportion of the total energy transfer to (pluses) and from (circles) infragravity frequencies f_2 involving two harmonic waves increased in the shoreward direction (Figure 4.14b) indicating an increasing contribution of the harmonics relative to waves at swell frequencies within the inner surfzone. These observations suggest that harmonic waves released in very shallow water could play a key role in the infragravity energy balance under dissipative conditions.

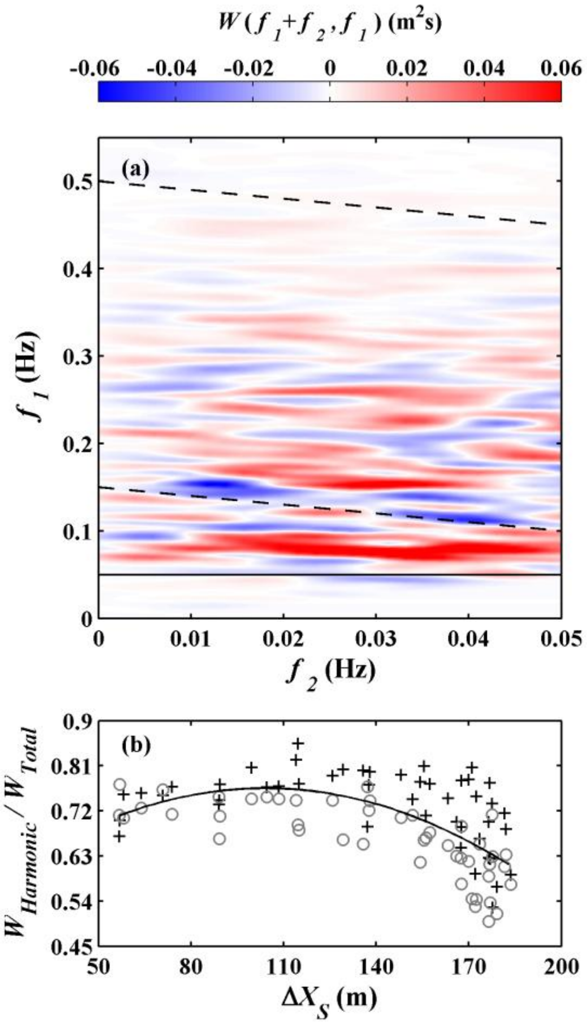

Figure 4.14. (a) Example nonlinear energy transfers $W(f_1+f_2, f_1)$ (Equation 4.20) to motions at infragravity frequency f_2 by triads with frequencies (f_1, f_2, f_1+f_2), calculated from a time series obtained by *NiwaOut* ADV at 10:10 (DST), during the first tidal cycle near high tide. Diagonal dashed lines mark region below which $f_1+f_2 < 0.5$ Hz (top line) and 0.15 Hz (bottom line). Horizontal solid line along $f_1 = 0.05$ Hz delimits region above which triads consist of only one infragravity wave. (b) Proportion of energy transfers involving two harmonic waves with frequencies (f_1+f_2, f_1) $W_{Harmonic}/W_{Total}$ to (positive $W(f_1+f_2, f_1)$, pluses) and from (negative $W(f_1+f_2, f_1)$, circles) infragravity waves f_2, as a function of cross-shore distance from the shoreline ΔX_S. $W_{Harmonic}$ is associated with the region in (a) where both f_1+f_2 and f_1 correspond to harmonic frequencies (defined here as $0.15 < f < 0.50$ Hz, region between two dashed lines), whereas W_{Total} also includes the region in (a) between lower dashed line and horizontal solid line, where f_1+f_2 and f_1 are within the swell range ($0.05 < f < 0.15$ Hz).

4.6 Conclusion

Swash oscillations on a low-sloping, dissipative beach were largely dominated by low-frequency ($f < 0.025$ Hz) infragravity waves. Incident waves at sea-swell frequencies were nearly fully dissipated through the surfzone by breaking, which yielded runup saturated at the incident band. In addition, swash energy at a higher-frequency infragravity band (0.035 Hz $< f <$ 0.05 Hz) also appeared to be saturated, similar to observations under high-energy offshore wave conditions, albeit offshore wave condition during our observations were mild. Our observations show that the frequency distribution (and total energy) of infragravity waves in infragravity-dominated swash motions were entirely consistent with the gradual dissipation of infragravity energy observed in the shallow surfzone.

Infragravity energy dissipation was strongly associated with breaking of sea-swell waves within the surfzone. Sea-swell wave breaking abruptly decreased nonlinear transfers to infragravity motions, making infragravity dissipation prevail over forcing and infragravity fluxes to decrease in the shoreward direction. Infragravity wave reflection increased with decreasing infragravity frequency, but was less than unity for all frequency bands. Tidal modulations in the dissipation pattern associated with changes to the beach face slope over the concave profile were largely responsible for shifting the zone of infragravity runup saturation to higher and lower frequencies. The strong control of beach slope on infragravity-dominated runup is consistent with field observations of *Ruggiero et al.* (2004).

Our observations suggest that the pathway of energy transfer between incident and infragravity frequencies as the waves progressed across the surf zone and into the swash zone involved higher order harmonics. We showed evidence of nonlinear difference interactions involving infragravity and high-frequency, secondary harmonic waves within the inner surfzone. Our findings suggest that these nonlinear harmonic waves could play a role in the wave energy balance near the shoreline on low-sloping, dissipative beaches. This may be in contrast to steeper barred beaches, where transfers of infragravity energy to and from swell waves have been shown to be more important.

Most infragravity forcing clearly occurred outside the surf-zone, and energy levels at sea-swell frequencies in the swash zone were very small, suggesting that bore-bore capture of sea-swell waves (e.g., *Mase*, 1995) may not be an important mechanism of infragravity generation on very gentle dissipative beaches.

Chapter 5

General Conclusions

5.1 Concluding remarks

Field observations of wave and swash hydrodynamics from two different sites were analysed. The sites were representative of medium-energy, steeper, intermediate beaches, characteristic of the east coast, and high-energy, low-sloping, dissipative beaches, typically observed on the west coast of New Zealand (Tairua Beach and Ngarunui Beach, Raglan respectively). As one would expect, the way in which swash motions were related to offshore wave climate was remarkably different on these two sites, particularly with respect to the magnitude of the vertical swash oscillations and the characteristics of the swash spectrum relative to offshore wave conditions.

The presence of a sandbar was found to change the characteristics of the swash motions on a steep, intermediate beach. The magnitude of the shoreline oscillations and the wave energy distribution among frequencies were highly controlled by the water depth over the sandbar crest, which defined the degree of wave breaking dissipation and the wave energy levels at the shoreline. Whereas here the water depth over the sandbar crest was modulated by changes in the tide, one would expect similar patterns to take place at distinct sites where the presence, quantity and characteristics of the sandbars are different. Accounting for the presence of sandbars and their distances from the shoreline, which might be viewed as a proxy of their depths, might improve the generalization of simple runup parameterizations, especially for steeper beaches where their effects in controlling wave breaking dissipation are typically maximized.

Alongshore runup variability at Tairua was strongly associated with changes in beach face slope. The sandbar morphology was notably alongshore-uniform during the period of the field experiment, despite previous observations having observed non-uniform sandbar features to be common at this site. However, the presence of a shoal near the southern end of the beach caused some variability in the degree of breaking-induced wave energy dissipation over this region, which also affected the magnitude of runup at both sea-swell and infragravity frequencies. These results suggest that prominent alongshore variability in sandbar morphology may lead to significant alongshore runup variability, which might be linked to coupling between shoreline and sandbar rhythmicity frequently observed in the field.

Swash motions on a low-sloping, dissipative beach were controlled by energy transfers between sea-swell and infragravity waves. Short waves at sea-swell frequencies were nearly fully-dissipated before reaching the swash zone and runup was essentially driven by wave energy at infragravity frequencies. However, infragravity waves were also observed to decrease in energy in the shoreward direction within the surfzone, and cross-shore changes in infragravity energy fluxes were highly associated with the energy density in the swash zone. Part of these infragravity losses appeared to be due to nonlinear energy transfer from infragravity back to incident waves, which were dissipated by breaking. Nevertheless, swash saturation and very small reflection coefficients observed for higher-frequency, infragravity waves, suggest that these waves might also have been limited by breaking in very shallow water (< 0.5 m). Understanding the conditions under which energy is gained or lost by infragravity waves in very shallow water is critical to predicting changes in swash motions on gently-sloping beaches.

A simple technique to quantify wave breaking dissipation was presented in this thesis. The method uses time stack images of the surfzone to detect breaking waves and calculates the probability of breaking across the surfzone. Quantifying the wave energy dissipated by breaking has been a challenge over the years, despite being critical to understanding wave transformation within the surfzone region. Though further testing and validation of the technique against field and laboratory experiments and numerical models would be desired, the technique has been successfully used in this thesis to investigate relative changes in wave dissipation and their contributions to swash motions, and could potentially be useful in future research.

Some of the limitations of this study are that some environmental parameters controlling swash oscillations were correlated in the field sites analysed in the thesis. Particularly, alongshore changes to beach face slope and the degree of wave breaking over the offshore sandbar were typically correlated which, despite being an interesting finding from this study, made it difficult to separate the relative contributions from these two variables. In addition, alongshore variability to the sandbar morphology was limited, and the effect of strong alongshore morphological variability on runup is unclear. Further research at different sites is needed to clarify these questions.

The sandbar control on runup was examined at one field site, subjected to a restricted range of offshore wave conditions, tidal range and nearshore morphology. Investigating the sandbar control under a wider range of environmental conditions would allow generalising the role of the sandbar in controlling swash oscillations. However, this was beyond the scope of this thesis.

Shallow water processes which are not accounted for in existing runup parameterizations, including bar-induced sea-swell wave breaking dissipation, infragravity dissipation and nonlinear wave energy transfers among wave frequencies were shown to have profound implications to the characteristics of the swash. Describing and quantifying such effects constitutes the main contribution of this thesis.

5.2 Suggestions for future research

This thesis answered some fundamental questions concerning swash oscillations on steep and low-sloping natural beaches and their relationship with environmental parameters, and gave rise to a number of further interesting research questions.

Wave breaking dissipation and changes in beach face morphology were both associated with changes to runup. However, the relative contributions of these two variables under a wide range of environmental conditions are still unclear. Investigating alongshore runup variability under highly non-homogeneous sandbar morphology, as well as tidally-modulated, cross-shore runup changes over convex beaches (where, conversely to the present observations, the beach slope decreases with increasing tide) could potentially help understanding their relative contributions.

This thesis showed evidence that secondary harmonic waves might be involved in the generation of infragravity motions at the shoreline through a mechanism of bore-bore capture. Examining this mechanism using numerical simulations could allow one to determine how important it could be under different wave and morphology conditions.

Nonlinear wave interaction patterns across the surfzone and their relationship with infragravity swash motions were investigated in this thesis. The shallowest observations took place at about 0.5 m water depth, shoreward of which the infragravity band started to dominate the spectrum and higher-frequency, infragravity waves might have broken. Examining shallower-water, field observations of wave hydrodynamics on low-sloping beaches may help clarifying the roles of energy transfer from infragravity waves and infragravity wave breaking in controlling infragravity swash motions.

References

Aagard, T., and J. Holm (1989), Digitization of wave run-up using video records, *J. Coastal Res.*, 5(3), 547–551.

Aarninkhof, S. G. J., B. G. Ruessink, and J. A. Roelvink (2005), Nearshore subtidal bathymetry from time-exposure video images, *J. Geophys. Res.*, 110, C06011, doi:10.1029/2004JC002791.

Baldock, T. E. (2006), Long wave generation by the shoaling and breaking of transient wave groups on a beach, *Proc. R. Soc. A*, 462, 1853–1876, doi:10.1098/rspa.2005.1642.

Baldock, T. E. and D. A. Huntley (2002), Long wave forcing by the breaking of random gravity waves on a beach, *Proc. R. Soc. A*, 458, 2177–2201, doi:10.1098/rspa.2002.0962.

Battjes, J. A. (1974), Surf similarity, in B. L. Edge (Ed.), Proceedings of the *Fourteenth Coastal Engineering Conference*, Copenhagen, pp. 466–480.

Battjes, J. A., H. J. Bakkenes, T. T. Janssen, and A. R. van Dongeren (2004), Shoaling of subharmonic gravity waves, *J. Geophys. Res.*, 109, C02009, doi:10.1029/2003JC001863.

Beji, S., and J. A. Battjes (1993), Experimental investigation of wave propagation over a bar, *Coastal Eng.*, 19, 151–162, doi:10.1016/0378-3839(93)90022-Z.

Bogle, J. A., K. R. Bryan, K. P. Black, T. M. Hume, and T. R. Healy (2000), Video observations of rip formation and evolution, *J. Coastal Res.*, 34(SI), 117–127.

Bryan, K. R., and A. J. Bowen (1998), Bar-trapped edge waves and longshore currents. *J. Geophys. Res.*, 103(C12), 27867–27884, doi:10.1029/98JC02098.

Bryan, K. R., and G. Coco (2010), Observations of nonlinear runup patterns on plane and rhythmic beach morphology, *J. Geophys. Res.*, 115, C09017, doi:10.1029/2009JC005721.

Bryan, K. R., P. A. Howd, and A. J. Bowen (1998), Field observations of bar-trapped edge waves. *J. Geophys. Res.*, 103(C1), 1285–1305, doi:10.1029/97JC02938.

Butt, T., and P. Russell (2000), Hydrodynamics and cross-shore sediment transport in the swash-zone of natural beaches: a review, *J. Coastal Res.*, 16(2), 255–268.

Castelle, B., B. G. Ruessink, P. Bonneton, V. Marieu, N. Bruneau, and T. D. Price (2010), Coupling mechanism in double sandbar systems. Part 1: patterns and physical explanation, *Earth Surf. Process. Landf.*, 35, 476–486, doi:10.1002/esp.1929.

Ciriano, Y., G. Coco, K. R. Bryan, and S. Elgar (2005), Field observations of swash zone infragravity motions and beach cusp evolution, *J. Geophys, Res.*, 110, C02018, doi:10.1029/2004JC002485.

Coco, G., K. R. Bryan, M. O. Green, B. G. Ruessink, I. L. Turner, and I. M. J. van Enckevort (2005), Video observations of shoreline and sandbar coupled dynamics, in M. Townsend, and D. J. Walker (Eds.), *Proceedings of Coasts and Ports* 2005, Adelaide, pp. 471–476.

Cowen, E. A., I. M. Sou, P. L.-F. Liu, and B. Raubenheimer (2003), Particle Image Velocimetry measurements within a laboratory generated swash zone, *J. Eng. Mech.*, 129(10), 1119–1129, doi:10.1061/(ASCE)0733-9399(2003)129:10(1119).

Elfrink, B., and T. Baldock (2002), Hydrodynamics and sediment transport in the swash zone: a review and perspectives, *Coastal Eng.*, 45, 149–167, doi:10.1016/S0378-3839(02)00032-7.

Elgar, S, B. Raubenheimer, and R. T. Guza (2005), Quality control of acoustic Doppler velocimeter data in the surfzone, *Meas. Sci. Technol.*, 16, 1889–1893, doi:10.1088/0957-0233/16/10/002.

Elgar, S., and R. T. Guza (1985), Observations of bispectra of shoaling surface gravity waves, *J. Fluid Mech.*, 161, 425–448, doi:10.1017/S0022112085003007.

Elgar, S., R. T. Guza, B. Raubenheimer, T. H. C. Herbers, and E. L. Gallagher (1997), Spectral evolution of shoaling and breaking waves on a barred beach, *J. Geophys. Res.*, 102(C7), 15797–15805, doi:10.1029/97JC01010.

Elgar, S., T. H. C. Herbers, and R. T. Guza (1994), Reflection of ocean surface gravity waves from a natural beach, *J. Phys. Oceanogr*, 24(7), 1503–1511, doi:10.1175/1520-0485(1994)024<1503:ROOSGW>2.0.CO;2.

Foote, M., and D. Horn (2002), Using video and GIS to measure two-dimensional water surface elevations in the swash zone, *Trans. in GIS*, 6(1), 43–68, doi:10.1111/1467-9671.00094.

Gallop, S. L., K. R. Bryan, and G. Coco (2009), Video observations of rip currents on an embayed beach, *J. Coastal Res.*, 56(SI), 49–56.

Gallop, S. L., K. R. Bryan, G. Coco, and S. A. Stephens (2011), Storm-driven changes in rip channel patterns on an embayed beach, *Geomorphology*, 127, 179–188, doi:10.1016/j.geomorph.2010.12.014.

Gorman, R., K. R. Bryan, and A. K. Laing (2003), Wave hindcast for the New Zealand region: nearshore validation and coastal wave climate, N. Z. J. Mar. Freshwater Res., 37, 567–588, doi:10.1080/00288330.2003.9517190.

Guedes, R. M. C., K. R. Bryan, G. Coco, and R. A. Holman (2011), The effects of tides on swash statistics on an intermediate beach, *J. Geophys. Res.*, 116, C04008, doi:10.1029/2010JC006660.

Guedes, R. M. C., K. R. Bryan, and G. Coco (2012), Observations of alongshore variability of swash motions on an intermediate beach, *Cont. Shelf Res.*, 48, 61–74 doi:10.1016/j.csr.2012.08.022.

Guza, R. T., and E. B. Thornton (1982), Swash oscillations on a natural beach, *J. Geophys. Res.*, 87(C1), 483–491, doi:10.1029/JC087iC01p00483.

Guza, R. T., and E. B. Thornton (1985), Observations of Surf Beat, J. Geophys. Res., 90(C2), 3161–3172, doi:10.1029/JC090iC02p03161.

Guza, R. T., E. B. Thornton, and R. A. Holman (1984), Swash on steep and shallow beaches, in B. L. Edge (Ed.), *Proceedings of the Nineteenth Coastal Engineering Conference*, Houston, pp. 708–723.

Haller, M. C., and P. A. Catalán (2009), Remote sensing of wave roller lengths in the laboratory, *J. Geophys. Res.*, 114, C07022, doi:10.1029/2008JC005185.

Hasselmann, K., W. Munk, and G. MacDonald (1963), Bispectra of ocean waves, in M. Rosenblatt (Ed.), *Time Series Analysis*, John Wiley, New York, pp. 125–139.

Haubrich, R. A. (1965), Earth Noise, 5 to 500 millicycles per Second 1. Spectral stationarity, normality, and nonlinearity, *J. Geophys. Res.*, 70(6), 1415–1427, doi:10.1029/JZ070i006p01415.

Heath, R. (1976), Broad classification of New Zealand inlets with emphasis on residence times, *N. Z. J. Mar. Freshwater Res.*, 10(3), 429–444, doi:10.1080/00288330.1976.9515628.

Henderson, S. M., and A. J. Bowen (2002), Observations of surf beat forcing and dissipation, *J. Geophys. Res.*, 107(C11), 3193, doi:10.1029/2000JC000498.

Henderson, S. M., R. T. Guza, S. Elgar, T. H. C. Herbers, and A. J. Bowen (2006), Nonlinear generation and loss of infragravity wave energy, *J. Geophys. Res.*, 111, C12007, doi:10.1029/2006JC003539.

Herbers, T. H. C., S. Elgar, and R. T. Guza (1994), Infragravity-frequency (0.005-0.05 Hz) motions on the shelf, I, Forced waves, *J. Phys. Oceanogr.*, 24(5), 917–927, doi:10.1175/1520-0485(1994)024<0917:IFHMOT>2.0.CO;2.

Herbers, T. H. C., S. Elgar, R. T. Guza, and W. C. O'Reiily (1995), Infragravity-frequency (0.005–0.05 Hz) motions on the shelf. Part II: free waves, *J. Phys. Oceanogr.*, 25(6), 1063–1079, doi:10.1175/1520-0485(1995)025<1063:IFHMOT>2.0.CO;2.

Holland, K. T., and J. A. Puleo (2001), Variable swash motions associated with foreshore profile change, *J. Geophys. Res.*, 106(C3), 4613–4623, doi:10.1029/1999JC000172.

Holland, K. T., and R. A. Holman (1993), The statistical distribution of swash maxima on natural beaches, *J. Geophys. Res.*, 98(C6), 10271–10278, doi:10.1029/93JC00035.

Holland, K. T., and R. A. Holman (1996), Field observations of beach cusps and swash motions, *Mar. Geol.*, 134, 77–93, doi:10.1016/0025-3227(96)00025-4.

Holland, K. T., and R. A. Holman (1999), Wavenumber-frequency structure of infragravity swash motions, *J. Geophys. Res.*, 106(C6), 13479–13488, doi:10.1029/1999JC900075.

Holland, K. T., B. Raubenheimer, R. T. Guza, and R. A. Holman (1995), Runup kinematics on a natural beach, *J. Geophys. Res.*, 100(C3), 4985–4993, doi:10.1029/94JC02664.

Holland, K. T., R. A. Holman, T. C. Lippmann, J. Stanley, and N. Plant (1997), Practical use of video imagery in nearshore oceanographic field studies, *IEEE J. Oceanic Eng.*, 22(1), 81–92, doi:10.1109/48.557542.

Holman, R. A. (1981), Infragravity energy in the surf zone, *J. Geophys. Res.*, 86(C7), 6442–6450, doi:10.1029/JC086iC07p06442.

Holman, R. A. (1986), Extreme value statistics for wave run-up on a natural beach, *Coastal Eng.*, 9, 527–544, doi:10.1016/0378-3839(86)90002-5.

Holman, R. A., and A. H. Sallenger (1985), Setup and swash on a natural beach, *J. Geophys. Res.*, 90(C1), 945–953, doi:10.1029/JC090iC01p00945.

Holman, R. A., and A. J. Bowen (1984), Longshore structure of infragravity wave motions, *J. Geophys. Res.*, 89(C4), 6446–6452, doi:10.1029/JC089iC04p06446.

Holman, R. A., and R. T. Guza (1984), Measuring run-up on a natural beach, *Coastal Eng.*, 8, 129–140, doi:10.1016/0378-3839(84)90008-5.

Howd, P. A., A. J. Bowen, and R. A. Holman (1992), Edge waves in the presence of strong longshore currents, *J. Geophys. Res.*, 97(C7), 11357–11371, doi:10.1029/92JC00858.

Howd, P. A., J. Oltman-Shay, and R. A. Holman (1991), Wave variance partitioning in the trough of a barred beach, *J. Geophys. Res.*, 96(C7), 12781–12795, doi:10.1029/91JC00434.

Huisman, C. E., K. R. Bryan, G. Coco, and B. G. Ruessink (2011), The use of video imagery to analyse groundwater and shoreline dynamics on a dissipative beach, *Cont. Shelf Res.*, 31, 1728–1738, doi:10.1016/j.csr.2011.07.013.

Huntley, D. A., R. T. Guza, and A. J. Bowen (1977), A universal form for shoreline run-up spectra?, *J. Geophys. Res.*, 82(18), 2577–2581, doi:10.1029/JC082i018p02577.

Iribarren, C. R., and C. Nogales (1949), Protection des Ports, paper presented at XVIIth International Navigation Congress, Lisbon.

Janssen, T. T., J. A. Battjes, and A. R. van Dongeren (2003), Long waves induced by short-wave groups over a sloping bottom, *J. Geophys. Res.*, 108(C8), 3252, doi:10.1029/2002JC001515.

Kim, Y., and E. Powers (1979), Digital bispectral analysis and its application to nonlinear wave interactions, *IEEE Trans. Plasma Sci.*, 7, 120–131, doi:10.1109/TPS.1979.4317207.

Kobayashi, N. (1999), Numerical modeling of wave run-up on coastal structures and beaches, *Mar. Technol. Soc. J.*, 33(3), 33–37, doi:10.4031/MTSJ.33.3.5.

Lippmann, T. C., and R. A. Holman (1989), Quantification of sand bar morphology: a video technique based on wave dissipation, *J. Geophys. Res.*, 94(C1), 995–1011, doi:10.1029/JC094iC01p00995.

Lippmann, T. C., R. A. Holman, and A. J. Bowen (1997), Generation of edge waves in shallow water, *J. Geophys. Res.*, 102(C4), 8663–8679, doi:10.1029/96JC03722.

List, J. H. (1991), Wave groupiness variations in the nearshore, *Coastal Eng.*, 15, 475–496, doi:10.1016/0378-3839(91)90024-B.

Longuet-Higgins, M. S., and R. W. Stewart (1962), Radiation stress and mass transport in gravity waves, with application to 'surf beats', *J. Fluid Mech.*, 13(4), 481–504, doi:10.1017/S0022112062000877.

Longuet-Higgins, M. S., and R. W. Stewart (1964), Radiation stresses in water waves; a physical discussion, with applications, *Deep-Sea Res.*, 11(4), 529–562, doi:10.1016/0011-7471(64)90001-4.

MacMahan, J. H., E. B. Thornton, and A. J. H. M. Reniers (2006), Rip current review, *Coastal Eng.*, 53, 191–208, doi:10.1016/j.coastaleng.2005.10.009.

Mase, H. (1988), Spectral characteristics of random wave run-up, *Coastal Eng.*, 12, 175–189, doi:10.1016/0378-3839(88)90004-X.

Mase, H. (1989), Random wave runup height on gentle slope, *J. Waterw., Port, Coast. Ocean Eng.*, 115(5), 649–661, doi:10.1061/(ASCE)0733-950X(1989)115:5(649).

Mase, H. (1995), Frequency down-shift of swash oscillations compared to incident waves, *J. Hydraul. Res.*, 33(3), 397–411.

Masselink, G. (1995), Group bound long waves as a source of infragravity energy in the surf zone, *Cont. Shelf Res.*, 15(13), 1525–1547, doi:10.1016/0278-4343(95)00037-2.

Masselink, G. (1998), Field investigation of wave propagation over a bar and the consequent generation of secondary waves. *Coastal Eng.*, 33, 1–9, doi:10.1016/S0378-3839(97)00032-X.

Masselink, G., and M. Hughes (1998), Field investigation of sediment transport in the swash zone, *Cont. Shelf Res.*, 18(10), 1179–1199, doi:10.1016/S0278-4343(98)00027-2.

Miche, M. (1951), Le pouvoir réfléchissant des ouvrages maritimes exposés a l'action de la houle, *Ann. Ponts Chaussees*, 121, 285–319.

Okihiro, M., and R. T. Guza (1995), Infragravity energy modulation by tides, *J. Geophys. Res.*, 100(C8), 16143–16148, doi:10.1029/95JC01545.

Oltman-Shay, J., and P. A. Howd (1993), Edge waves on nonplanar bathymetry and longshore currents: a model and data comparison, *J. Geophys. Res.*, 98(C2), 2495–2507, doi:10.1029/92JC02609.

Oltman-Shay, J., and R. T. Guza (1987), Infragravity edge wave observations on two California beaches, *J. Phys. Oceanogr.*, 17(5), 644–663, doi:10.1175/1520-0485(1987)017<0644:IEWOOT>2.0.CO;2.

Palmsten, M. L., and R. A. Holman (2011), Infiltration and instability in dune erosion, *J. Geophys. Res.*, 116, C10030, doi:10.1029/2011JC007083.

Pawka, S.S. (1983), Island shadows in wave directional spectra, *J. Geophys. Res.*, 88(C4), 2579–2591, doi:10.1029/JC088iC04p02579.

Peregrine, D. H. (1983), Breaking waves on beaches, *Annu. Rev. Fluid Mech.*, 15, 149–178, doi:10.1146/annurev.fl.15.010183.001053.

Plant, N. G., K. T. Holland, and M. C. Haller (2008), Ocean wavenumber estimation from wave-resolving time series imagery, *IEEE Trans. Geosci. Remote Sens.*, 46(9), 2644–2658, doi:10.1109/TGRS.2008.919821.

Puleo, J. A., R. A. Beach, R. A. Holman, and J. S. Allen (2000), Swash zone sediment suspension and transport and the importance of bore-generated turbulence, *J. Geophys. Res.*, 105(C7), 17021–17044, doi:10.1029/2000JC900024.

Raubenheimer, B., and R. T. Guza (1996), Observations and predictions of run-up, *J. Geophys. Res.*, 101(C10), 25575–25587, doi:10.1029/96JC02432.

Raubenheimer, B., R. T. Guza, and S. Elgar (1996), Wave transformation across the inner surf zone, *J. Geophys. Res.*, 101(C10), 25589–25597, doi:10.1029/96JC02433.

Raubenheimer, B., R. T. Guza, S. Elgar, and N. Kobayashi (1995), Swash on a gently sloping beach, *J. Geophys. Res.*, 100(C5), 8751–8760, doi:10.1029/95JC00232.

Ruessink, B. G. (1998a), Bound and free infragravity waves in the nearshore zone under breaking and nonbreaking conditions, *J. Geophys. Res.*, 103(C6), 12795–12805, doi:10.1029/98JC00893.

Ruessink, B. G. (1998b), The temporal and spatial variability of infragravity energy in a barred nearshore zone, *Cont. Shelf Res.*, 18, 585–605, doi:10.1016/S0278-4343(97)00055-1.

Ruessink, B. G., M. G. Kleinhans, and P. G. L. van den Beukel (1998), Observations of swash under highly dissipative conditions, *J. Geophys. Res.*, 103(C2), 3111–3118, doi:10.1029/97JC02791.

Ruggiero, P., P. D. Komar, J. J. Marra, W. G. McDougal, and R. A. Beach (2001), Wave runup, extreme water levels and the erosion of properties backing beaches, *J. Coastal Res.*, 17, 407–419.

Ruessink, B. G., G. Coco, R. Ranasinghe, and I. L. Turner (2007), Coupled and noncoupled behaviour of three-dimensional morphological patterns in a double sandbar system, *J. Geophys. Res.*, 112, C07002, doi:10.1029/2006JC003799.

Ruggiero, P., R. A. Holman, and R. A. Beach (2004), Wave run-up on a high-energy dissipative beach, *J. Geophys. Res.*, 109, C06025, doi:10.1029/2003JC002160.

Sénéchal, N., G. Coco, K. R. Bryan, and R. A. Holman (2011), Wave runup during extreme storm conditions, *J. Geophys. Res.*, 116, C07032, doi:10.1029/2010JC006819.

Sénéchal, N., P. Bonneton, and H. Dupuis (2002), Field experiment on secondary wave generation on a barred beach and the consequent evolution of energy dissipation on the beach face, *Coastal Eng.*, 46, 233–247, doi:10.1016/S0378-3839(02)00095-9.

Sheremet, A., R. T. Guza, S. Elgar, and T. H. C. Herbers (2002), Observations of nearshore infragravity waves: Seaward and shoreward propagating components, *J. Geophys. Res.*, 107(C8), doi:10.1029/2001JC000970.

Sherwood, A. M. and C. S. Nelson (1979), Surficial sediments of Raglan Harbour, *N. Z. J. Mar. Freshwater Res.*, 13(4), 475–496, doi:10.1080/00288330.1979.9515825.

Sonu, C. J. (1973), Three-dimensional beach changes, *J. Geol.*, 81, 42–64.

Stockdon, H. F., R. A. Holman, P. A. Howd, and A. H. Sallenger (2006), Empirical parameterization of setup, swash, and runup, *Coastal Eng.*, 53, 573–588, doi:10.1016/j.coastaleng.2005.12.005.

Symonds, G., D. A. Huntley, and A. J. Bowen (1982), Two-dimensional surf beat: long wave generation by a time-varying breakpoint, *J. Geophys. Res.*, 87(C1), 492–498, doi:10.1029/JC087iC01p00492.

Thomson, J., S. Elgar, B. Raubenheimer, T. H. C. Herbers, and R. T. Guza (2006), Tidal modulation of infragravity waves via nonlinear energy losses in the surf zone, *Geophys. Res. Lett.*, 33, L05601, doi:10.1029/2005GL025514.

Thornton, E. B., and C. S. Kim (1993), Longshore current and wave height modulation at tidal frequency inside the surf zone, *J. Geophys. Res.*, 98(C9), 16509–16519, doi:10.1029/93JC01440.

Thornton, E. B., and R. T. Guza (1983), Transformation of wave height distribution, *J. Geophys. Res.*, 88(C10), 5925–5938, doi:10.1029/JC088iC10p05925.

Turner, I. L., and G. Masselink (1998), Swash infiltration-exfiltration and sediment transport, *J. Geophys. Res.*, 103(C13), 30813–30824, doi:10.1029/98JC02606.

van Dongeren, A., J. Battjes, T. Janssen, J. van Noorloos, K. Steenhauer, G. Steenbergen, and A. Reniers (2007), Shoaling and shoreline dissipation of low-frequency waves, *J. Geophys. Res.*, 112, C02011, doi:10.1029/2006JC003701.

van Enckevort, I. M. J., and B. G. Ruessink (2001), Effect of hydrodynamics and bathymetry on video estimates of nearshore sandbar position, *J. Geophys. Res.*, 106(C8), 16969–16979, doi:10.1029/1999JC000167.

van Enckevort, I. M. J., and B. G. Ruessink (2003), Video observations of nearshore bar behavior. Part 1: alongshore uniform variability, *Cont. Shelf Res.*, 23, 501–512, doi:10.1016/S0278-4343(02)00234-0.

Wright, L.D., and A. D. Short (1984), Morphodynamic variability of surf zones and beaches: a synthesis, *Mar. Geol.*, 56, 93–118, doi:10.1016/0025-3227(84)90008-2.

Appendix

Non-stationary patterns in swash motions

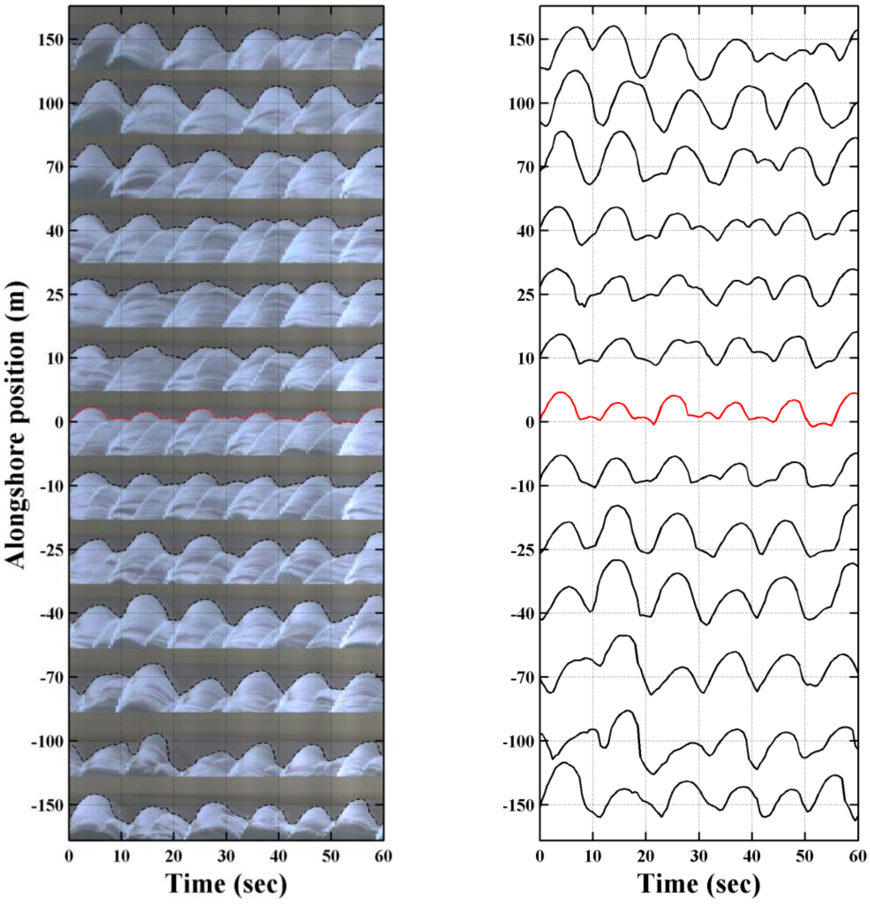

R. M. C. Guedes, K. R. Bryan, G. Coco, and S. Kruse (2011), Non-stationary patterns in swash motions, in *Proceedings of the Coasts and Ports 2011*, Pattiaratchi, C. (Ed.), Perth.

Abstract

Swash motions, shoreline oscillations driven by waves, are traditionally assumed to be a stationary process. The assumption of stationarity implies that techniques like Fourier analysis cannot be used to detect potential transient features such as those that could result from variations in offshore wave grouping. An alternative technique that has been often applied to investigating non-stationary processes is wavelet analysis, which yields localized information in both the time and frequency domains. Here, we use wavelet analysis to investigate infragravity swash motions at Tairua Beach in New Zealand. Time series of swash motions were obtained using video images at 31 alongshore locations spaced every 10 *m*. One-hour time series were obtained using video images recorded at 2 *Hz* at both low and high tide. The swash edge was identified using an edge detection algorithm and converted to vertical swash motions using known geometric transformations and a Lidar beach topography survey. An ADCP deployed in 12 *m* water depth measured the offshore wave climate. Fourier and wavelet transforms were performed on both the offshore and shoreline time series. We found that although the main features in the offshore spectra were similar using both techniques, the wavelet analysis also indicated that there were consistent localized time-variations in incident power that could be readily associated with variations in wave grouping. We observed a similar modulation in shoreline motions although, at certain alongshore positions and for large wave groups, energy at infragravity frequencies was also evident. Overall, our observations and analysis show that the wavelet technique can be a useful tool to investigate possible coupling between wave groupiness and infragravity swash motion.

Keywords: swash, ocean waves, infragravity motions, stationarity, wavelet analysis.

A.1. Introduction

Wave measurements in the inner surf and swash zones often show energetic motions at relatively long (infragravity) periods (i.e. >20 sec), even though these oscillations are normally a very small portion of the offshore wave field (e.g. *Guedes et al.*, 2011; *Guza and Thornton*, 1982). These infragravity motions are believed to be associated with the commonly-observed phenomenon of wave groupiness, in which the waves organize themselves in successive groups of high and small waves due to wave beating (*Longuet-Higgins and Stewart*, 1962).

Transfer of energy from incident to infragravity frequencies within the surfzone occurs through nonlinear interactions. According to *Longuet-Higgins and Stewart* (1962) the grouping pattern causes gradients in radiation stress between groups of large waves, where the sea surface is depressed and small waves, where it is raised. As a result, long (bound) waves with same period but 180° out of phase with respect to the wave groups are generated. It is widely assumed that these bound waves are released as a result of wave breaking and propagate towards the shoreline as free long waves, although *Baldock* (2009) has suggested that there is not a physical explanation or convincing evidence to support this release theory. Yet another mechanism proposed by *Symonds et al.* (1982) suggests that the long waves can be generated by time-varying breakpoint position. The group-modulation of wave heights induces variations in the width of the surf zone which are reflected by changes to the setup at the group periods and its harmonics, therefore generating long waves. Interactions between successive swash events may also contribute to the infragravity swash spectrum (e.g. *Mase*, 1988). The process is characterized either by an uprush being overtaken by the following one or a downwash colliding with the following uprush. Such interactions could cause longer period modulation at the shoreline, not necessarily associated with infragravity shallow-water waves. Recently, *Guedes et al.* (2011) suggested that higher-frequency (than incident) waves might contribute to this process.

Free surface elevation and swash data are normally assumed to be sufficiently stationary to use analysis techniques specifically developed for stationary time series. The use of stationary techniques such as Fourier analysis implies that information on the frequency distribution of power can only be obtained for the complete duration of the time series (*Farge*, 1992). The time information of potential transient features such as wave groups is inherently lost. An alternative technique that has been often applied to investigating non-stationary processes is wavelet analysis, which yields localized information in both the time and frequency domains. For instance, wavelet has been applied to the study of turbulence (e.g. *Farge*, 1992), rhythmic sandbar features (e.g. *Ruessink et al.*, 2007) and the El Niño-Southern Oscillation (e.g. *Gu and Philander*, 1995). Wavelets have also been found to be suitable for detecting group modulations in nearshore lake waves (*Liu*, 2000). However, we are unaware of studies applying wavelet analysis to swash data.

The objective of this paper is to investigate simultaneous time series of offshore and swash oscillation through a wavelet approach, and attempt to link potential coupling between offshore wave grouping and infragravity motions at the shoreline.

A.2. Wavelet analysis

The continuous wavelet transform of a time series $x(n)$, n=0...N-1 and time sampling dt is defined as the convolution of this time series with scaled and translated versions of base analyzing functions called “mother” wavelets $\psi(n)$ (*Farge*, 1992, *Torrence and Compo*, 1998):

$$W_n(s) = \sum_{n'}^{N-1} x_{n'} \cdot \psi * \left[\frac{(n'-n)dt}{s} \right], \tag{A.1}$$

where the * is the complex conjugate. The variation in the wavelet scale s and its translation along the time index n allows the energy in the *1*-dimensional time series $x(n)$ to be decomposed into both time and scale (*Farge*, 1992). Therefore, the wavelet transform is particularly appropriate to identify transient patterns that characterize non-stationary signals.

The base functions must satisfy some conditions among which they should be well localized in both time and frequency (with finite number of oscillations) and their average should be zero (*Farge*, 1992, *Torrence and Compo*, 1998). Moreover, the scaled versions of the wavelet $\psi_0(n)$ should be normalized as

$$\psi\left[\frac{(n'-n)dt}{s} \right] = \left(\frac{dt}{s} \right)^{1/2} \psi_0 \left[\frac{(n'-n)dt}{s} \right], \tag{A.2}$$

to have unit energy and to ensure that the wavelet coefficients are weighted only by $x(n)$ (*Torrence and Compo*, 1998). The choice of the wavelet function is important since the wavelet coefficients will have information of both the signal and the function itself. For the analysis of real-valued signals such as sea surface elevation and swash oscillations, progressive, complex-valued wavelets are appropriate because the quadrature phase shift between their real and imaginary parts allows one to eliminate their oscillations by visualizing the modulus of the coefficients (*Farge*, 1992). One of the most widely used complex-valued wavelets and the one adopted here is the Morlet (Figure A.1) which is a plane wave modulated by a Gaussian envelope, defined in the time domain as:

$$\psi(n) = \pi^{1/4} e^{i\omega_0 n} e^{-n^2/2}, \tag{A.3.}$$

where ω_0 is a non-dimensional frequency, commonly set to 6 to ensure admissibility (*Farge*, 1992, *Torrence and Compo*, 1998).

The relationship between the wavelet scale s and the equivalent Fourier period T can be calculated analytically for each type of wavelet and for the Morlet with ω_0=6, T=1.03s (hereinafter, results will be presented using the equivalent Fourier period).

The wavelet transforms (Equation A.1) is considerably faster if calculated in Fourier space since all the N convolutions can be done simultaneously for each scale (*Torrence and Compo*, 1998). However, the Fourier transform of non-cyclic time series leads to errors near the end of the time series. These errors can be minimized by padding the end of $x(n)$ with zeros prior to wavelet transforming. The compromise is the decrease in the wavelet coefficients near the edges which becomes more important at higher scales. The region within which the edge effects cannot be negligible is termed cone of influence and, for the Morlet wavelet, scales as $\sqrt{2}s$.

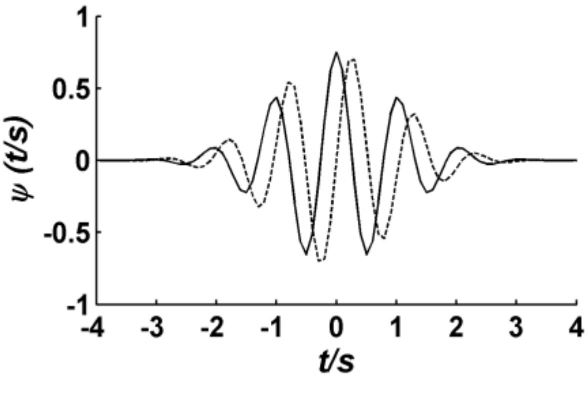

Figure A.1. Morlet wavelet ψ as a function of nondimensional time t/s. Solid and dashed lines are the real and imaginary parts of the function.

A.3. Methods

A.3.1. Field site

The dataset analysed here was obtained during a field experiment undertaken on 15–17 July 2008 at Tairua Beach, a 1.2-*km*-long pocket beach located on the Pacific coast of New Zealand (Figure A.2). This medium-coarse grained beach has a fairly steep beach face slope of about 5° and is exposed to medium wave energy with average offshore significant wave height and mean spectral period of 0.9 *m* and 5.8 *s*ec (*Gorman et al.*, 2003). The tides are semi-diurnal, with tidal ranges between 1.2 (neap) and 2 *m* (spring tides) and the system is normally classified as intermediate, with a rhythmic sandbar and strong rip currents often present (*Bogle et al.*, 2000). The sandbar remained remarkably alongshore uniform during the 3 days, at a cross-shore distance of about 80 *m* from the shoreline and with water depths over the crest changing from about 1.1 to 2.2 *m* due to tidal variations.

A.3.2. Field measurements

During the field experiment, measurements of offshore wave climate and beach topography, and video images of the beach were obtained (a comprehensive overview of some of these measurements is given by *Guedes et al.*, 2011). For this study, we selected two 60-*min* long periods from the second day of our dataset, at low tide starting at 11.00am and during high tide starting at 16.00pm.

The waves were measured using an ADCP deployed in a water depth of about 12 *m* (~800 *m* distant from the coast). Time series of subsurface pressure were recorded every hour for 20 *min*, at 2 *Hz* and converted to free surface elevation η_0 using linear wave theory.

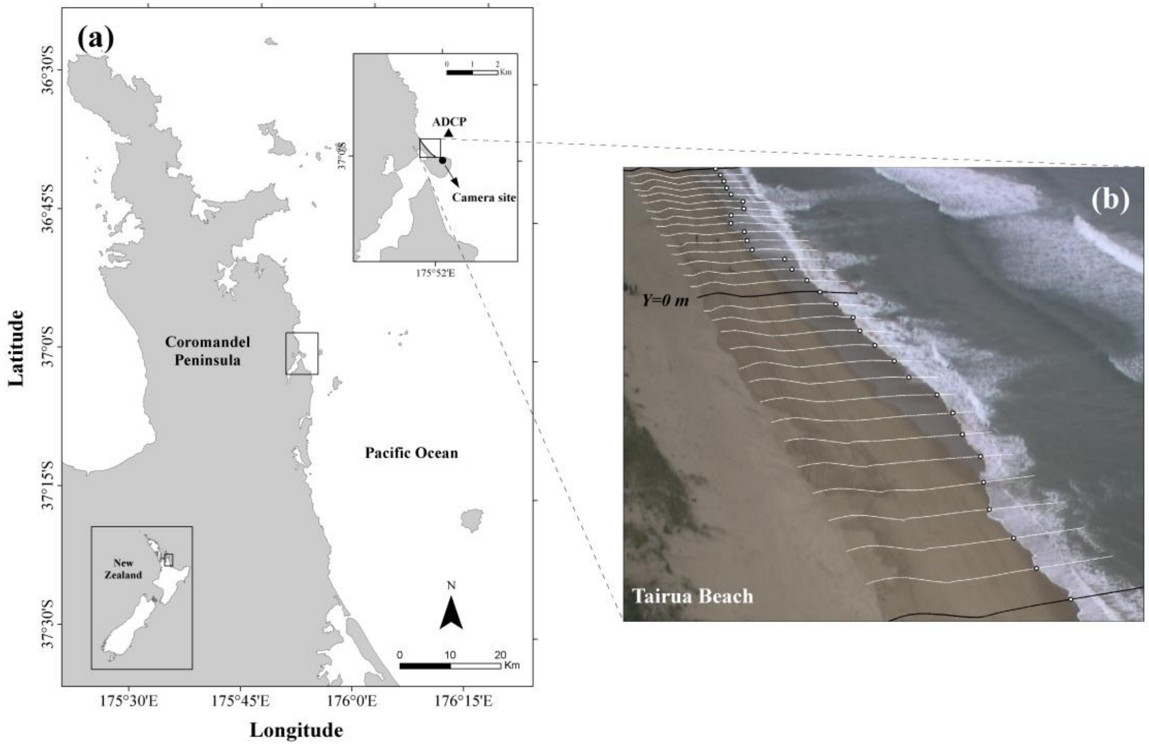

Figure A.2. Field site location with inset showing locations of camera and ADCP (a). Oblique image obtained at Tairua Beach on 16 July 2008 at 11:01am, during low tide (b). The lines show the alongshore positions where the swash was measured with the circles indicating where our algorithm detected the edge of the swash for this image.

The beach topography was surveyed with a land-based lidar laser scan once each day (the survey carried on July 16th is used here). An area extending for 300 *m* alongshore was selected within the surveyed area for the processing. The hugely-dense “point-cloud” obtained from the beach scan was filtered using algorithms created to remove outliers and non-desired points (e.g. foreign objects such as people standing on the beach). The algorithms repeatedly eliminated points below/above some standard deviation threshold within predefined windows. Finally, the remaining points were rotated and interpolated to a regular spacing of 0.5 *m* in the cross-shore and 1.0 *m* in the alongshore direction. The grid has the origin located at the alongshore position of the black line close to the centre of Figure A.2b and increases towards the NW direction.

High-resolution images (1528 x 2016 pixels) were acquired continuously at 2 *Hz* (e.g. Figure A.2b), using a digital camera mounted at the southern end of the beach (Figure A.2a) at approximately 42 *m* above the sea level. Runup oscillations were extracted at 31 positions spaced every 10 *m* alongshore, within the area covered by the lidar survey, using a technique known as ‘time stack’. The technique consists of time series of pixel intensity sampled along cross-shore transects defined on the images. Conversions between pixel and ground coordinates were made using the colinearity equations described in *Holland et al.* (1997) with corrections for lens distortions (see *Guedes et al.*, 2011 for more detail on the technique).

A.3.3. Data analysis

The swash location was defined as the most shoreward edge of water identifiable on each line of the time stacks. The edge was detected using an image processing algorithm, developed to distinguish the sharp contrast observed between the swash front, typically characterized by the presence of white foam, and the darker sandy beach. Manual detections of the swash were required in some images where the algorithm failed due to poor lighting contrast. Time series of vertical runup elevation R were derived from the digitized swash locations since the beach topography was accurately known from the lidar survey. In total, 62 time series of runup elevation were generated over the 2 periods of interest.

Variations in η_0 induced by offshore wave grouping were assessed by performing running standard deviations over the offshore series. A window width equivalent to ~3 wavelengths (76 datapoints) was used for the calculations. The time-delay of the waves between the location of the ADCP and the shoreline was estimated using linear wave theory to calculate the group speed, and used to provide a sort of “synchronization” between the offshore and swash time series.

The wavelet transform was performed on the offshore and swash time series obtained during the two periods selected for the analysis. Each time series was detrended and normalized by its variance prior to wavelet transformed. The resultant wavelet coefficients were converted to wavelet power spectra as $|W_n(s)|^2$ and scale-averaged (see *Torrence and Compo*, 1998) over incident (10 s < T < 15 s) and infragravity periods (20 s < T < 40 s). Hereinafter, the time series of scale-averaged wavelet power spectrum over incident and infragravity bands will be referred to as W_{inc} and W_{ig}, respectively.

Fourier power spectrum was calculated from each linearly detrended offshore and runup time series, segmented into sections of 256 *sec* (resulting in a bandwidth of 0.0039 *Hz*) and tapered with a Hanning window (50% overlap), giving typically 11 and 37 degrees of freedom for the offshore and the runup time series.

A.4. Results

During the two periods selected for analysis, the offshore wave parameters remained remarkably similar while large differences were observed at the shoreline. Offshore significant wave height, calculated as 4σ of the detrended time series (where σ is the standard deviation), changed from 0.86 *m* (low tide) to 0.82 *m* (high tide). The peak wave period, found from the inverse of the peak frequency from the Fourier spectrum, barely changed (from 11.4 to 11.5 *sec*) and virtually no infragravity energy was observed offshore. Yet, at the shoreline, the alongshore-averaged significant swash height increased by 68%, from 1.1 to 1.8 *m*, and peak swash period decreased from 12.7 to 11.6 *sec* (10%) from low to high tide. The alongshore-averaged ratio between the variance at infragravity (<0.05 *Hz*) and incident frequencies (>0.05 *Hz*) decreased by almost a factor of 4 between low tide (0.45) and high tide (0.12). These changes were found by *Guedes et al.* (2011) to be predominantly driven by tidally-controlled variations in the degree of wave breaking over the sandbar.

Figure A.3 shows time series of offshore sea surface elevation η_0 obtained at low tide and associated time series of running standard deviation $\sigma_{run-\eta_0}$, the wavelet power spectrum $W_n(s)$ and the scale-averaged wavelet power over the incident band $W_{Inc-\eta_0}$. It can be readily noticed that the groups of high waves are associated with peaks in $\sigma_{run-\eta_0}$ and the width of these peaks reflects the time length of the high-wave groups. These features can also be observed from the wavelet power at incident periods. It is apparent that the high-wave groups yield peaks in the wavelet spectrum at the offshore wave period, and that the time history of these peaks, expressed by $W_{Inc-\eta_0}$, shows essentially the same information as $\sigma_{run-\eta_0}$ with the correlation coefficient r^2 between these series amounting to 0.87 (significant at the 95% confidence level).

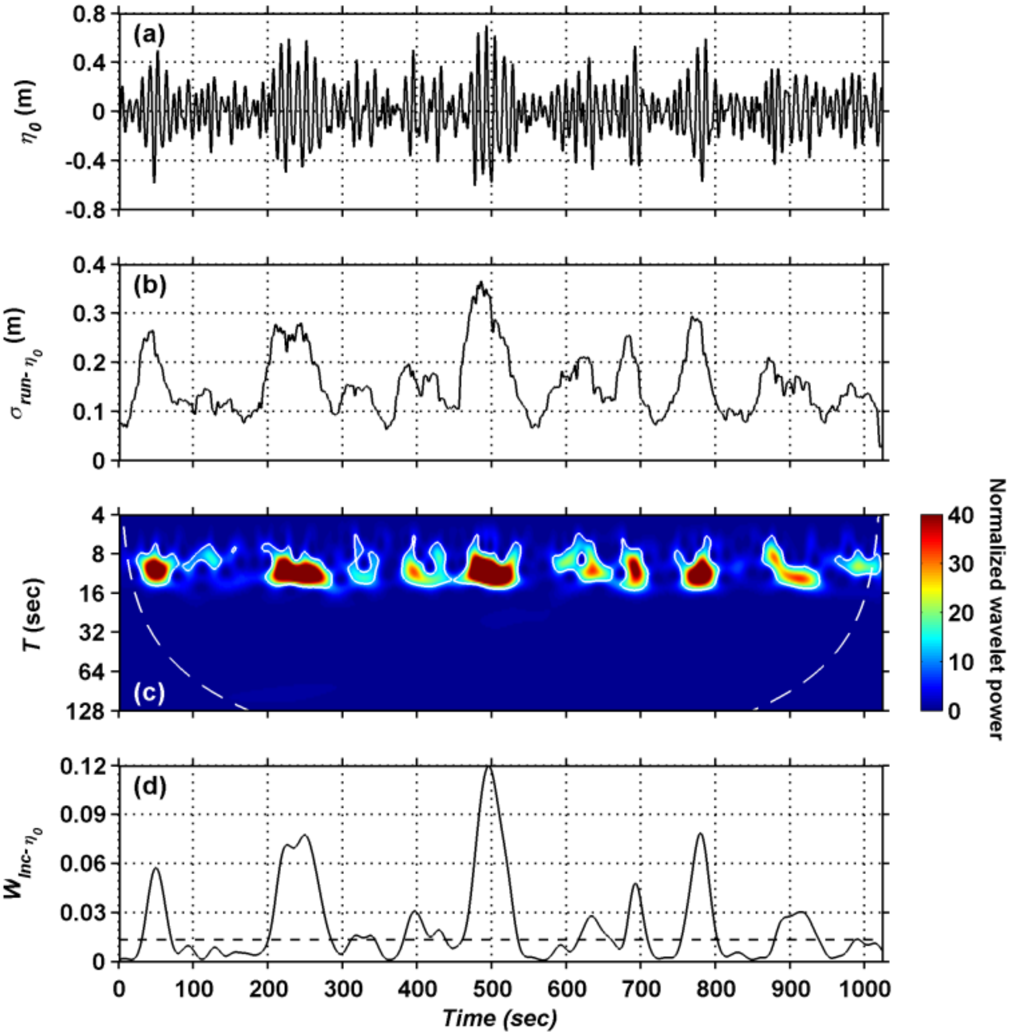

Figure A.3. (a) Time series of offshore sea surface elevation η_0 obtained on 16 July 2008. (b) Time series of running standard deviation σ_{run} calculated from (a). (c): Normalized wavelet power spectrum $W_n(s)$ obtained for the offshore time series shown in (a). White solid contours show the 5% significance level against red noise. The cone of influence is shown by the white dashed curves. The normalized power gives a measure of the power relative to white noise. (d): Scale-averaged wavelet power over the incident band W_{Inc} calculated from (c). Dashed line is 95% confidence level.

In order to investigate whether the infragravity swash power could be associated with the offshore wave groups, the offshore time series of scaled-averaged wavelet power over the incident band $W_{Inc-\eta_0}$ were regressed against the runup series of scaled-averaged wavelet power. Figure A.4 shows the Pearson product-moment correlation coefficient r obtained from the regressions of $W_{Inc-\eta_0}$ with W_{Inc-R} (Figure A.4a) and W_{Ig-R} (Figure A.4b), plotted as a function

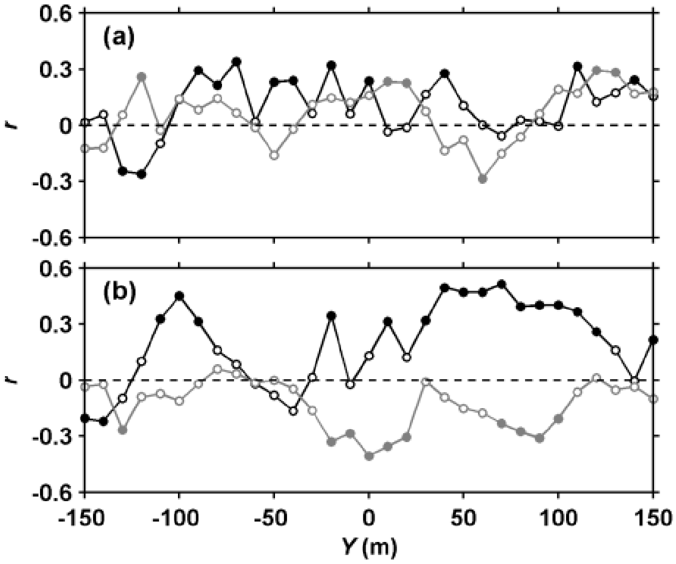

Figure A.4. Alongshore series of the Pearson product-moment correlation coefficient *r* between offshore series of incident scaled-averaged wavelet power $W_{Inc-\eta_0}$ and swash series of scaled-averaged wavelet power, over (a) the incident W_{Inc-R} and (b) infragravity band W_{Ig-R}. Black and gray lines show correlation for series collected at low and high tide, respectively. Significant values at the 95% confidence level are highlighted by filled circles.

of alongshore position *Y* at the shoreline. W_{Inc-R} does not show a clear correlation pattern with $W_{Inc-\eta_0}$. Although there are some alongshore locations where a significant linear relationship (at the 95% confidence level) can be observed between these variables, at most positions the correlation is not significant. It can also be observed that the significant values are mostly positive.

At infragravity frequencies, on the other hand, some interesting features can be observed. At low tide, when the infragravity power at the shoreline was maximized, a significant linear relationship at the 95% confidence was found at most alongshore locations between $W_{Inc-\eta_0}$ and W_{Ig-R} (Figure A.4b, black line). At high tide, conversely, no significant linear relationship at the 95% confidence level was found at most alongshore positions (Figure A.4b, gray line). Furthermore, significant values of *r* are mostly positive at low tide, although

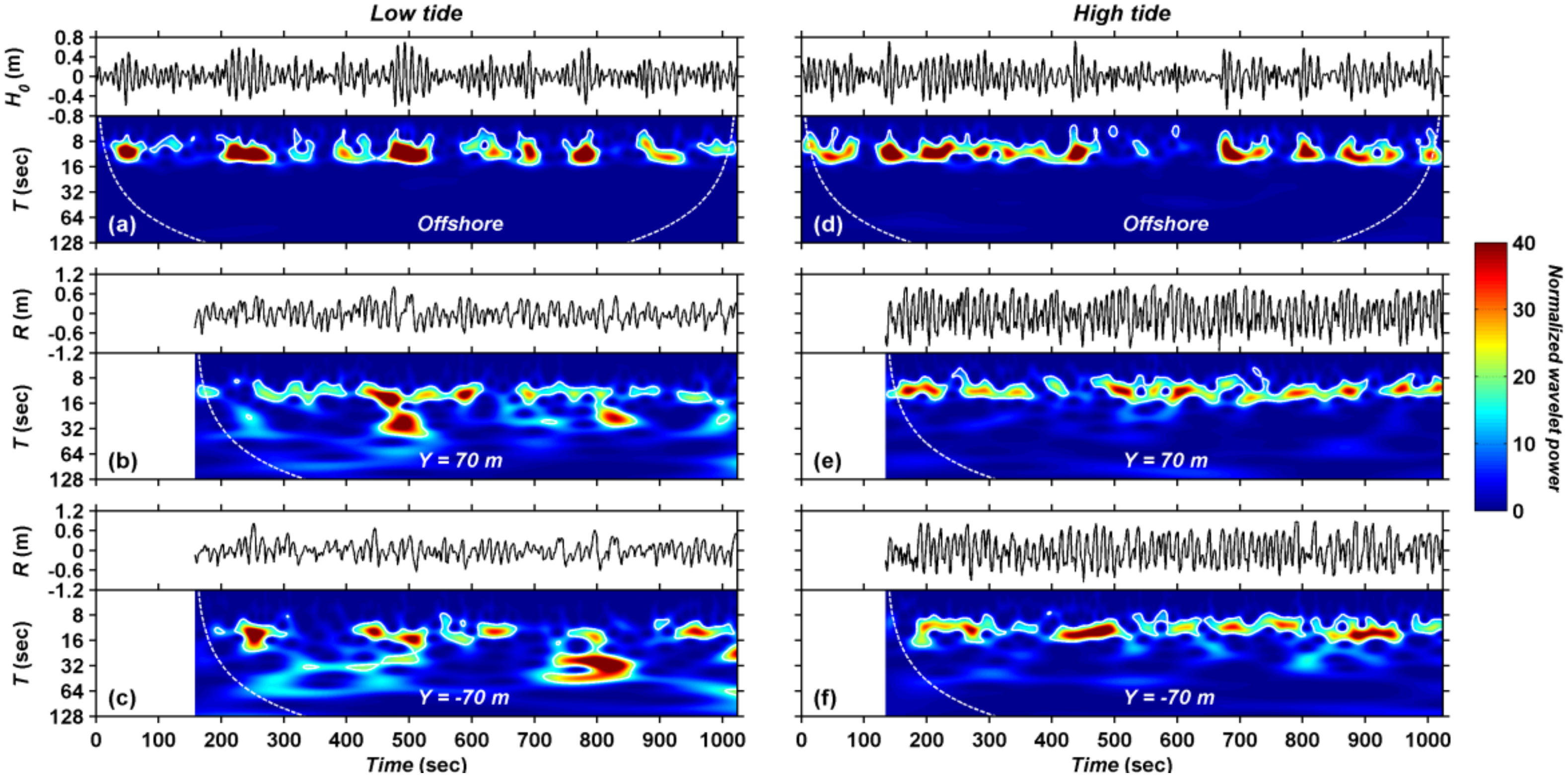

Figure A.5. Low (a–c) and high tide (d–f) time series (top), and respective normalized wavelet power spectrum $W_n(s)$ (bottom). Panels (a,d) are offshore data; panels (b,e) and (c,f) are swash data for the alongshore positions y=70 *m* and y=-70 *m*, respectively. The 5% significance level is shown as the white solid contours. The cone of influence is shown by the white dashed curves. The normalized power gives a measure of the power relative to white noise. Blank region on the left-hand side of the swash plots correspond to time delay calculated during low (158 *sec*) and high tide (134 *sec*).

during high tide they are always negative. Finally, we notice that there is a consistent alongshore pattern with absolute values of *r* normally higher on the northern side of the beach (positive values of *Y*) with a nodal location around *Y*=-60 *m* where the correlations are small and not significant for the two periods analysed.

Figure A.5 shows some examples of wavelet power spectra and respective time series obtained offshore and at alongshore positions where there was (*Y*=70 *m*) and there was not (*Y*=-70 *m*) a statistically significant linear relation between $W_{Inc-\eta_0}$ and W_{Ig-R}. It is apparent that there is considerably more infragravity power at low tide, and that this power varies along the length of the time series. The time locations where the infragravity power is located can be somewhat associated with the grouping-modulated offshore incident peaks, for the low tide data at *Y*=70 *m* (Figures A.5a and A.5b), as suggested by the significant value of *r* at this location. At *Y*=-70 *m*, conversely, the swash infragravity power cannot be readily connected to the offshore group modulation (Figures A.5a and A.5c). At high tide (Figures A.5d–f) the association between the offshore incident power and the swash infragravity power is not evident as the infragravity swash energy is low and not significant, yet there seems to be some regions with higher infragravity power at *Y*=70 *m* connected to groups of low waves offshore.

A.5. Discussion and conclusion

The significant linear correlation observed between $W_{Inc-\eta_0}$ and some of the time series of W_{Ig-R} supports the hypothesis of infragravity swash motions being associated with offshore wave grouping. The correlations were generally higher at low tide, when the infragravity swash energy was greater and when there was considerably more active wave breaking over the sandbar. The fact that *r* was positive at low tide and negative at high tide is also intriguing and suggests that there might be different mechanisms generating long waves. Intense wave breaking conditions appear to be associated with long waves in phase with the wave group structure, consistent with the mechanism proposed by *Symonds et al.* (1982), although the low-energy, infragravity swash motions observed at high tide appear to be more consistent with *Longuet-Higgins and Stewart* (1962). We also noticed that, even though the correlations might be significant, they are not strong (the highest correlation coefficient r^2 observed at low tide at Y=70 m amounts to 0.27). Therefore, part of the infragravity swash signal might be indeed not associated with long waves, and result from other mechanisms such as swash interactions.

A well-defined pattern between the grouping information offshore and the incident power at the shoreline was not observed either during low or high tide. This is consistent with the group structure being destroyed as the waves approach very shallow water near the shoreline and become strongly depth-dependent. Additionally, interaction between individual swash cycles should potentially complicate the scenario at incident periods.

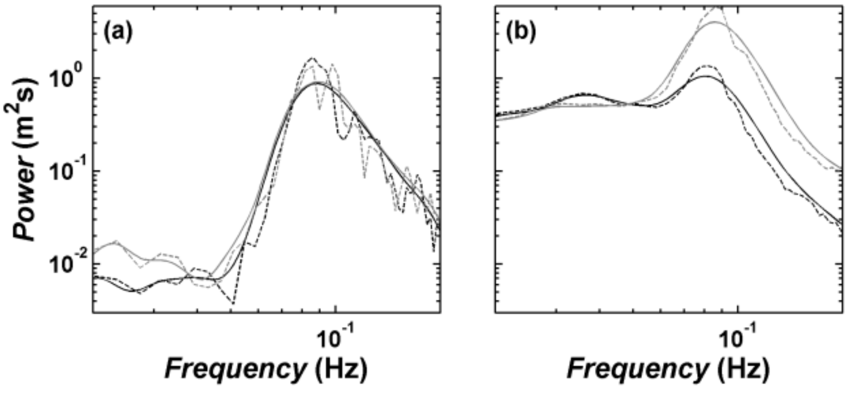

Figure A.6. Fourier spectra (dashed lines) and wavelet spectra integrated over all times (solid lines) calculated for the offshore (a) and shoreline data (b). Black and gray lines are spectra calculated for the low and high tide time series, respectively (the time series were not normalized by their variance here). The swash spectra were averaged over all alongshore positions.

The wavelet and the Fourier analysis showed some similar features. Figure A.6 shows the wavelet integrated over all times (the global wavelet) and the Fourier power spectra, for the offshore (Figure A.6a) and swash data (Figure A.6b). Both the shape, the location of the peaks and the total variance were consistent. The main distinction was the smoother and wider incident peaks observed in the global wavelet spectra, which results from neighbouring wavelet scales being correlated (*Percival*, 1995).

We found the wavelet analysis to be a useful tool for detecting not only the frequencies where the offshore wave power was distributed at, but also modulation of this power due to wave groupiness. This agrees with the analysis conducted by *Liu* (2000) on data from nearshore lake waves. Nevertheless, the wavelet was also found to be an appropriate means of analysing runup data as the infragravity swash power was consistently observed to be transient in time, which opposes to the commonly-accepted idea of stationarity.

References

Baldock, T. (2009), Bound wave release induced by short wave breaking – true or false?, in M. Mizuguchi, and S. Sato (Eds.), *Proceedings of the Coastal Dynamics 2009*, Tokyo, Paper 8.

Bogle, J. A., K. R. Bryan, K. P. Black, T. M. Hume, and T. R. Healy (2000), Video observations of rip formation and evolution, *J. Coastal Res.*, 34(SI), 117–127.

Farge, M. (1992), Wavelet transforms and their applications to turbulence, *Annu. Rev. Fluid Mech.*, 24, 395–457, doi:10.1146/annurev.fl.24.010192.002143.

Gorman, R., K. R. Bryan, and A. K. Laing (2003), Wave hindcast for the New Zealand region: nearshore validation and coastal wave climate, N. Z. J. Mar. Freshwater Res., 37, 567–588, doi:10.1080/00288330.2003.9517190.

Gu, D. and S. G. H. Philander (1995), Secular changes of annual and interannual variability in the Tropics during the past century, *J. Climate*, 8, 864–876, doi:10.1175/1520-0442(1995)008<0864:SCOAAI>2.0.CO;2.

Guedes, R. M. C., K. R. Bryan, G. Coco, and R. A. Holman (2011), The effects of tides on swash statistics on an intermediate beach, *J. Geophys. Res.*, 116, C04008, doi:10.1029/2010JC006660.

Guza, R. T. and E. B. Thornton (1982), Swash oscillations on a natural beach, *J. Geophys. Res.*, 87(C1), 483–491, doi: 10.1029/JC087iC01p00483.

Holland, K. T., R. A. Holman, T. C. Lippmann, J. Stanley, and N. Plant (1997), Practical use of video imagery in nearshore oceanographic field studies, *IEEE J. Oceanic Eng.*, 22(1), 81–92, doi:10.1109/48.557542.

Liu, P. C. (2000), Wave grouping characteristics in nearshore Great Lakes, *Ocean Eng*., 27(11), 1221–1230, doi:10.1016/S0029-8018(99)00042-6.

Longuet-Higgins, M. S., and R. W. Stewart (1962), Radiation stress and mass transport in gravity waves, with application to ‘surf beats’, *J. Fluid Mech*., 13(4), 481–504, doi:10.1017/S0022112062000877.

Mase, H. (1988), Spectral characteristics of random wave run-up, *Coastal Eng.*, 12, 175–189, doi:10.1016/0378-3839(88)90004-X.

Percival, D. P. (1995), On estimation of the wavelet variance, *Biometrika*, 82(3), 619–631, doi:10.1093/biomet/82.3.619.

Ruessink, B. G., G. Coco, R. Ranasinghe, and I. L. Turner (2007), Coupled and noncoupled behaviour of three-dimensional morphological patterns in a double sandbar system, *J. Geophys. Res.*, 112, C07002, doi:10.1029/2006JC003799.

Symonds, G., D. A. Huntley, and A. J. Bowen (1982), Two-dimensional surf beat: Long wave generation by a time-varying breakpoint, *J. Geophys Res.*, 87(C1), 492–498, doi:10.1029/JC087iC01p00492.

Torrence, C. and G. P. Compo (1998), A practical guide to wavelet analysis, *Bull. Am. Meteorol. Soc.*, 79, 61–78, doi:10.1175/1520-0477(1998)079<0061:APGTWA>2.0.CO;2.